Orogenic high-*T* granitoids of the central Grenville Province: characteristics and geodynamic implications

by

© Cheuk Yin Yip

A Thesis submitted to the School of Graduate Studies

in partial fulfilment of the requirements

for the degree of

Master of Science

Department of Earth Sciences

Memorial University of Newfoundland

May 2025

St. John's, Newfoundland and Labrador

Abstract

Conventional models of collisional orogens predict S-type granitoid emplacement during the orogenic climax, whereas high-*T* (also known as A-type) granitoids, commonly associated with mantle-derived magmas, are expected to form by late-orogenic extensional collapse. However, the Grenville Province lacks significant syn-orogenic S-type granites, while high-*T* granitoid bodies were intermittently emplaced in its hinterland throughout the duration of the Grenvillian Orogeny. These rocks are particularly abundant in central Grenville, where they intrude Mesoproterozoic Quebecia crust, in the granulite-facies mid and low-*P* segments of the orogenic hinterland and are spatially associated with ~1.16–1.13 Ga anorthosites.

A review of a literature database shows that the high-*T* granitoids of the central Grenville Province were emplaced intermittently in the orogenic hinterland between ca. 1086 and 1007 Ma (with an apparent gap ~1042–1032 Ma) and are dominantly ferroan, metaluminous to weakly peraluminous, alkali-calcic, with strong negative HFSE anomalies. In addition, a petrological and geochemical investigation of samples from four granitoid bodies suggests crystallisation conditions at ~5–6 kbar and ~800–1000ºC and variable oxidising conditions. Within-plate transitional to arc-like geochemistry, oxidising fO_2 values, relatively evolved whole-rock ε_{Nd} and zircon ε_{Hf} with Paleo- to Mesoproterozoic T_{DM} suggest significant inheritance from the Quebecia arc crust. The granitoids may have originated from the anhydrous, partial melting of the intermediate, granulitic mid- to lower crust.

Irrespective of the magma sources, orogenic high-*T* magmatism over a span of ~80 Myr reflects substantial mantle heat flux. The high concentration of these granitoids and the ~1.16–1.13 Ga anorthosites in Quebecia suggests that orogenic magmatism is heavily influenced by lithospheric structures inherited from the evolution of Quebecia in the pre-Grenvillian Mesoproterozoic Laurentian margin.

Acknowledgements

I would like to express my deepest gratitude to my supervisor, Dr. Aphrodite Indares, for her invaluable guidance, support, patience, and the time she dedicated to this project. It has been an honour to be supervised by her over the past two and a half years. I am also sincerely grateful to my co-supervisor, Dr. Gregory Dunning, for his insightful advice on igneous petrology and geochronology, which greatly enriched this research. Québec Ministry of Natural Resources and Forests and Abdelali Moukhsil are thanked for data provision. I am grateful and appreciate the positive reviews and valuable feedback provided by Dr. Steven Denyszyn and Dr. Hamish Sandeman during the examination of my thesis.

I extend my appreciation to the CREAIT team: Dylan Goudie (SEM–MLA), Sherri Strong (TIMS), Dr. Wanda Aylward (EPMA), and the LA–ICP–MS team, Dr. Sebastian Kommescher and Dr. Rebecca Lam, as well as Matt Crocker for sample preparation. Their technical expertise and support were essential to this work.

I am fortunate to have been part of a supportive research group, including Susan Strowbridge, Arlin Fonseca, Dr. Caroline Lotout, and Daniela Mendoza Marin. The discussions, laughter, and encouragement from this group helped me grow both academically and personally.

I would also like to give a special thank you to Dr. John Malpas for his encouragement in pursuing further studies in Newfoundland. I am also deeply grateful to my family for their unwavering support as I pursued my dream on the other side of the world. Thank you, my best friend and partner, Louis; your unconditional support and company have been tremendously important during our studies. I also appreciate my friends—Gabriel, Nagi, Hans, Pascal, Ming, Caroline, Debby and Denise—for our fruitful discussions and your incredible companionship.

This research was supported by an NSERC Discovery Grant to Dr. Aphrodite Indares. I am also grateful to the School of Graduate Studies for its financial support throughout my master's program.

Table of contents

List of Figures

List of Tables

Appendix

Appendix A. Whole-rock geochemistry database (SIGEOM and this study)

Appendix B. EPMA results

Appendix C. Zircon CL collages of studied samples

Appendix D. LA–ICP–MS zircon U–Pb results

Appendix E. LA–ICP–MS zircon trace element results

Appendix F. MC–LA–ICP–MS zircon Lu–Hf results

Chapter 1. Introduction

1.1. Introduction, aim of the study and organisation of the thesis

Continental collision is expressed in crustal thickening and shortening, followed by extension and thinning (Bickford 1990; Spencer et al. 2017; Wilson et al. 2019). In conventional orogenic models, during the shortening phase, the thickened crust generates radiogenic heat that promotes partial melting of supracrustal rocks to form aluminous S-type granites (Chappell & White 1974; Patiño Douce & McCarthy 1998; Kemp & Hawkesworth 2003; Hopkinson et al. 2017). In contrast, during post-collision or late to post-orogenic extension, asthenospheric uprising may contribute juvenile, mantle-derived underplating basaltic magma, adding anhydrous, high-temperature (high-*T*, >800ºC), A-type granites in the orogenic crust (e.g. Barbarin 1990; Pitcher 1997; Miller et al. 2003; Jacob et al. 2021). However, in the Mesoproterozoic Grenville Orogen, S-type granitic bodies are inconspicuous, whereas syn- to late-orogenic high-*T*, intermediate to felsic granitoids are locally abundant in the orogenic hinterland (Indares 2024).

The late Mesoproterozoic (~1090–980 Ma) Grenville Orogen is interpreted as a long-duration, large, hot orogen in which granulite-facies rocks, representing formerly intermediate to deep levels of orogenic crust, are widely exposed in the hinterland (Hynes & Rivers 2010; Rivers 2012; Rivers et al. 2012). In addition, the local concentration of syn- to late, orogenic high-*T* granitoids in the hinterland indicates an elevated thermal influence of the mantle during orogenesis (Indares 2020). Such magmatism acts as an advective mantle-crust heat transfer, but the links to regional high-grade metamorphism remain uncertain.

This study aims to improve understanding of the orogenic high-*T* granitoid magmatism in the hinterland of central Grenville Province, where such magmatism is particularly abundant. This study has two main components: (1) review and interpretation of U–Pb ages and geochemical patterns using published data on high-*T* granitoids from this area, and (2) assessment of whole-rock geochemistry, isotopic signatures, and of the zircon isotopic and geochemical record using samples collected from a subset of these granites. The tectonic implications of the high-*T* granitoid magmatism in the central Grenville Province are discussed,

and in a broader sense, this study provides insights into granite petrogenesis in a Mesoproterozoic collisional tectonic setting.

This thesis aims to answer key questions regarding the formation of orogenic high-*T* granitoids in the central Grenville Province. First-order questions include: (1) Are there any spatiotemporal trends, or any change in geochemical patterns with time? (2) What are the *T* conditions of crystallisation and the depths of emplacement? Second-order questions include: (1) What is the source of magma that could account for the observations? (2) Are the tectonic settings of magmatism consistent with current tectonic models for the Grenvillian Orogeny?

This Chapter introduces the rationale behind the study and provides background information on the Grenville Province, on high-*T* granitoid magmatism in general and on ways to assess it. Approach, methodology and analytical techniques are described in Chapter 2. Chapter 3 presents a synthesis of literature data on the geochemistry and geochronology of the central Grenville granitoids. Chapter 4 is a focused investigation in terms of petrology, geochemistry and zircon isotopic and geochemical signatures, of samples from four plutons that intruded different crustal levels in the region. Chapter 5 integrates the results, discusses key points and concludes this study.

1.2. Background geology

1.2.1. The Grenville Province

The Grenville Orogen is considered the result of the continent-continent collision between Laurentia and Amazonia in the late Mesoproterozoic (~1090–980 Ma) and is placed in the core of the Rodinia supercontinent configuration (Fig. 1.1; Li et al. 2008; Hynes & Rivers 2010). The Grenville Orogen was built upon the southeastern Laurentian margin. This margin was comprised of the southern parts of the Archean-Paleoproterozoic continental nucleus (internal Laurentia) and peripheral, accretionary systems active during the Paleo- to Mesoproterozoic (external Laurentia, also referred to as the Great Proterozoic Accretionary Orogen; Whitmeyer & Karlstrom 2007; Condie 2013). Among the latter, Labradorian (~1.68–1.62 Ga), Pinwarian (originally defined ~1.50–1.45 Ga, but continuing down to ~1.35 Ga; Indares et al. 2023), and Elzevirian (~1.30–1.20 Ga) are recognised as the most active periods of peri-cratonic crustal growth for over 500 Myr in external Laurentia (Gower & Krogh 2002; Rivers et al. 2012; Daniel et al. 2023).

Most of the Grenville Orogen was built upon external Laurentia crust, reworked during the Grenvillian Orogeny, and delineated by Nd model ages (e.g. Dickin 2000) or as crustal-age domains by zircon U–Pb ages (Rivers et al. 2012). In addition, the 1.19–1.14 Ga accretionary Shawinigan orogen, overprinted Elzevirian crust in the SW Grenville (Carr et al. 2000).

The Grenville Province (Fig. 1.2a & b) represents the geographical extent of the Orogen and is separated from the rest of Laurentia by the Grenville Front and is divided into the hinterland (Allochthonous Belt) at the orogenic core and the Parautochthonous Belt at the orogenic periphery (Rivers 1997; Rivers et al. 2012). The Parautochthonous Belt mostly consists of Archean and Paleoproterozoic crust of internal Laurentia, which was reworked during the last phase (Rigolet phase) of the Grenvillian orogeny (~1005–980 Ma; Rivers, 2008). The metamorphic grade increases from greenschist to amphibolite/granulite facies from northwest to southeast towards the hinterland.

In contrast, the hinterland consists of a Paleo-Mesoproterozoic crust of external Laurentia that varies from southwest to northeast. In eastern Grenville, Labradorian (~1.7–1.6 Ga) and Pinwarian (~1.65–1.45 Ga) crustal domains are recognised, where the Pinwarian crust is interpreted as a continental arc segment (Dickin 2000; Gower & Krogh 2002). To the southwest, in central Grenville, Quebecia is a Pinwarian (~1.50–1.35 Ga) juvenile domain with some older Nd model ages of ~1.65–1.5 Ga (Dickin & Higgins 1992; Vautour & Dickin 2019; Dickin et al. 2023). Further southwest, accreted Elzevirian terranes with mixed Nd model ages and U–Pb ages younger than 1.3 Ga are identified in the western Grenville (Fig. 1.2a; Dickin 2000; McLelland et al. 2010a).

The hinterland was widely metamorphosed under granulite-facies conditions at the climax of the Grenvillian orogeny (~1090–1020 Ma Ottawa phase; Rivers 1997, 2008). Based on peak metamorphic pressure (*P*) conditions, the Ottawan hinterland is subdivided into the high-*P* (higher than 14 kbars), mid-*P* (~11–8 kbars), and low-*P* (~7–6 kbars) segments (or belts) that represent orogenic crust exhumed from different depths (Rivers 2008). In the high- and mid-*P* segments, regional metamorphism at granulite facies reached ~800–900ºC. The low-*P* segments mainly consist of upper amphibolite facies assemblages (Groulier et al. 2018b), and furthermore, a low-*P* granulite facies segment was recently recognised in the central Grenville Province

(Groulier et al. 2016; Groulier et al. 2018b; Indares 2020). An additional tectonic division, the Ottawan orogenic lid, represents the exposed highest crustal levels that were less affected by the Grenvillian Orogeny (Fig. 1.2b).

Based on key orogenic features, the evolution of the Grenville Orogen is interpreted to have involved: (a) crustal thickening contributing to ductile flow and development of an orogenic plateau in the hinterland during the culmination of the Ottawan phase; (b) subsequent extension by gravitational spreading from ca. 1050 to 1020 Ma in the hinterland: and (c) final propagation of the orogen towards the foreland, leading to metamorphism and deformation in the Parautochthonous Belt, during the Rigolet phase (Rivers 2008; Rivers et al. 2012). A major contribution to these interpretations comes from numerical modelling in the western Grenville Province, involving hot, flow nappes and syn-convergent exhumation that simulated orogenic features along the transect of the orogenic belt and predicted a thermally weakened, ductile mid-crust of 750–900ºC over a prolonged period (~100 Myr; Beaumont et al. 2010; Jamieson & Beaumont 2011).

1.2.2. High-T magmatism in the hinterland of the Grenville Province

Following the accretionary stages of the pre-Grenvillian Laurentian margin, high-*T* magmatism started before the onset of the Grenvillian orogeny. This was manifested by a major phase of anorthosite-mangerite-charnockite-granite (AMCG) magmatism at ~1.16–1.13 Ga that generated voluminous anorthositic complexes in two regions of the Grenville Province (Fig. 1.2b). The Adirondacks Anorthosite and AMCG complex intruded the ~1.19–1.14 Ga Shawinigan orogen in western Grenville (Corrigan & Hanmer 1997; McLelland et al. 2010b). The other AMCG complexes were emplaced approximately in a north-south trend broadly at the eastern and western margins of Quebecia. In addition, the intrusion of Lac-Saint-Jean and Vallant Anorthosite followed major crustal structures (Saint-Fulgence and Pipmuacan deformation zones, Fig. 1.2b; Turcotte 2001; Hébert et al. 2009).

Grenvillian-age orogenic magmatism is mostly expressed by high-*T* granitoids, but also anorthosites that are less voluminous than the earlier ones, and its distribution led to the definition of the Interior Magmatic Belt in the hinterland (Corrigan & van Breemen, 1997; Corriveau, 1990; Gower et al., 1991; Rivers et al., 2012). Orogenic magmatism occurred in

distinct settings across the orogen (Fig. 1.2b; Indares 2024). In the Adirondacks, Lyon Mountain Granite is spatially associated with pre-Grenvillian anorthosite. It is thought to have been emplaced at ~1.05 Ga (mid-Ottawan) following ~1.07–1.06 Ga extension as a product of partial melting of mafic crust under the presence of an unaddressed heat source (Indares 2024 and references therein). In western Grenville, small, undeformed, older (~1.09–1.06 Ga) alkaline granites intruded the Frontenac and Composite Arc Belt in the Ottawan Orogenic Lid (e.g. Corriveau et al. 1990; Cutts 2014). In central Grenville, Grenvillian-age intermediate to felsic granitoid bodies are commonly exposed in Quebecia, with the largest plutons (~1.08–1.05 Ga Parc-des Lauretides Complex; ~1.06–1.01 Ga Varin Monzonite; Indares 2020) spatially associated with the pre-Grenvillian anorthosites. In the same area, anorthosite plutons, such as Vanel, Mattawa, Labrieville and St. Urbain Anorthosite, were generated between ca. 1.08 and 1.01 Ga (e.g. Owens et al. 1994; Hébert et al. 2009; Morisset et al. 2009). A range of smaller monzonitic to granitic bodies, with or without orthopyroxene, are emplaced intermittently in both mid-*P* and low-*P* segments during the same period (Rivers et al. 2012; Indares 2020, 2024). In contrast, numerous ~975–950 Ma post-tectonic alkaline plutonic intrusions are exposed in eastern Grenville (Gower et al. 1991), and these are inferred to be linked to the late stages of the opening of the Asgard Sea, between Laurentia and Baltica in the Neoproterozoic, which are unrelated to the Grenvillian Orogeny (Strowbridge et al. 2022).

1.2.3. Regional geology of the hinterland of the central Grenville Province

A major crustal component in this part of the hinterland is Quebecia, which predominantly consists of Pinwarian, ~1.50–1.35 Ga lithologic associations (Fig. 1.2). These rocks have juvenile Nd model ages at ~1.60–1.50 Ga, as well as locally older Nd model ages at ~1.8–1.6 Ga (Dickin & Higgins 1992; Dickin 2000; Vautour & Dickin 2019; Dickin et al. 2023). In addition, older Labradorian-age rocks are exposed farther north (Dunning & Indares 2010). The lithologic associations of Quebecia include Pinwarian-age plutonic and sedimentary rocks, such as ~1.5 Ga Hulot orthogneiss and Plus-Value and Bourdon paragneiss (Moukhsil et al. 2013a; Moukhsil et al. 2014). In addition, ~1.50 to 1.45 Ga volcano-sedimentary sequences and associated plutonic units are preserved in the Escoumins Supracrustal Belt (ESB, Groulier et al. 2018b) and the Montauban Group in the Portneuf–Mauricie domain (Corrigan & van Breemen

1997). The pre-Grenvillian geology in the central Province is interpreted as follows: rifting of a part of the Laurentian margin at or before ~1.5 Ga leading to passive-margin sedimentation, followed by the development of pericratonic island arcs on previously rifted crustal fragments, which were subsequently re-integrated into Laurentia during ~1.4–1.37 Ga (Groulier et al. 2020; Dickin et al. 2023).

In central Grenville, spanning from Manicouagan in the north to Escoumins/Baie-Comeau in the south (referred to as the Manicouagan–Escoumins transect; Indares 2020, Fig. 1.1b), a complete section across Grenvillian-age tectono-metamorphic divisions is exposed (Figs. 1.2 & 1.3). To the north, the high-*P* segment is represented by the Manicouagan Imbricate Zone, where rocks predominantly of Labradorian to Pinwarian age underwent high-*P* granulite to eclogite-metamorphism ~1040–1015 Ma during the waning stage of the Ottawan phase (Lotout et al. 2023). To the south, the mid- and low-*P* segments are interpreted as reworked Quebecia crust (e.g. Dickin 2000). The mid-*P* segment consists of Pinwarian-age orthogneisses and metasedimentary rocks, which were metamorphosed at mid-*P* granulite-facies conditions ~1080–1040 Ma at the culmination of the Ottawan phase (Dunning & Indares 2010). This segment terminates at the presumed extension of two major deformation zones, the Saint-Fulgence and Pipmuacan Deformation Zones (Figs 1.2 & 1.3). South and east of these zones, ~1160–1050 Ma plutonic rocks are dominant (Indares 2020), and preliminary data suggest low-*P* granulite-facies metamorphism in this area (Fonseca-Martinez & Indares 2024). At the southern-most end of the transect, the Escoumins Supracrustal Belt (ESB) comprises Pinwarian volcano-sedimentary sequences that underwent low-*P* amphibolite-facies metamorphism during the Grenvillian Orogeny (Groulier et al. 2018a; 2018b). Therefore, the entire region south and east of the Saint-Fulgence and Pipmuacan Deformation Zones is inferred to represent a low-*P* segment (Indares 2020).

Saint-Fulgence and Pipmuacan Deformation Zones are significant, long-lived structural elements in the Lac-St-Jean region. The Saint-Fulgence Deformation Zone is a polyphase, NE–SW trending dextral transpressional shear zone (~2 km wide, ~400 km long). It marks the western boundary of Lac-St-Jean anorthosite and was active from at least before 1090 Ma to ~1008 Ma (Owens et al. 1994; Hébert et al. 2009). To the north, the Pipmuacan Deformation

Zone crosscuts the ~1148 Ma Lac-Saint-Jean (LSJ) Anorthosite and remained active until ~1008 Ma (Higgins et al. 2002). These crustal-scale deformation zones are important boundaries in central Grenville, indicating active deformation during the orogeny.

1.3. High-*T* granitoid magmatism

1.3.1. General characteristics

Granitoid rocks with solidus temperature exceeding 800°C are labelled as "hot" or high-*T* (Miller et al. 2003). These rocks possess characteristic mineralogical features; for instance, ternary feldspar can be variably transformed into perthite or antiperthite. Ternary feldspar generally crystallises from high-*T* magma, while plagioclase exsolves from alkali feldspar host to form perthite, or vice versa for anti-perthite, under sub-solidus conditions (Nekvasil 2011). In addition, rapakivi texture is common in coarse-grained or megacrystic high-*T* granites (Vernon 2016). Finally, the presence of magmatic pyroxene in granite or monzonite (charnockite or mangerite) in granulite terranes also implies relatively high-*T* regimes during emplacement (Frost & Frost 2008; Touret & Huizenga 2012).

These high-*T* granitoids exhibit geochemical features commonly associated with "A-type" but the definition of A-type granite remains complex and inconsistently applied in the literature. The term A-type granite, introduced by Loiselle and Wones (1979), refers to a distinct group of granites that are alkaline, anhydrous, reducing, and inferred to be anorogenic. These granites are marked by high total alkali content ($K_2O + Na_2O$), Fe-number ($Fe^* = [FeO_t/(FeO_t + MgO)]$), and enrichment in high field strength elements (HFSE) and rare earth elements (REE), while elements compatible with mafic silicates and plagioclase (e.g. Cr, Co, Ni, Sr, Ba, Eu) are depleted (Collins et al. 1982; Clemens et al. 1986; Whalen et al. 1987). Their composition and petrogenesis are associated with high-*T* conditions, often linked to partial melting of the mantle in extensional tectonic settings (Miller et al. 2003; Moyen et al. 2021). However, wheras high-*T* granites are also formed under elevated thermal conditions (Chappell et al. 2007) and may exhibit features overlapping with A-type granites, they are not restricted to anorogenic settings and can be formed in a variety of tectonic environments (Bonin 1990; King et al. 2001; Bonin 2007; Jacob et al. 2021). The magma's oxidation state may range from oxidising to reducing (Ishihara 1977; Anderson & Morrison 2005; see section 1.3.3). Despite their shared characteristics, high-*T*

granites and A-type granites are not interchangeable terms and should not be treated as synonyms when the tectonic setting is unknown.

The generation of granitoids is controlled by magma crystallising conditions and sources of magma, resulting in the petrological and geochemical characteristics of the granitoids (Jacob et al. 2021; Moyen et al. 2021). The formation of granitoids is the result of various petrogenetic processes, including but not limited to the differentiation of (1) mantle-derived basaltic magma, (2) partial melting of crust (crustal anatexis), and (3) assimilation of crustal material during fractionation (Frost et al. 2001a; Frost & Frost 2011). Granitoids sourced from the partial melting of the mantle would have a relatively short residence time (≤200 Myr) in the crust (Condie 2013). On the other extreme, crustal anatexis recycles existing crustal material and forms granitoids as a part of the reworked crust. In the case of assimilating crustal material during the fractionation of mantle-derived magma, a hybridised melt, which has both mantle and crustal components, is formed (e.g. Hildreth & Moorbath 1988; Frost et al. 2001b). The source of magma can be traced by isotope chemistry, such as whole-rock Sm–Nd and zircon Lu–Hf isotopes.

1.3.2. Geochemical and petrological toolbox

Several indicators can be used to understand the petrogenetic conditions of magmatic rocks. This study utilises whole-rock lithogeochemistry, isotope chemistry, geothermobarometry and zircon characteristics as the means to constrain the sources of magma and the *P–T* conditions of magma crystallisation.

1.3.2.1. Geochemical classification of granitoids

Classification of granitic rocks enables the identification of possible petrogenetic processes and tectonic settings. Bonin et al. (2020) proposed that an ideal classification for high-*T* granitoids should adhere to key principles: (1) objectively illustrating the key geochemical characteristics, (2) linking major element geochemistry to petrological observations, and (3) identifying trends and associations rather than individual compositions. The five crucial geochemical properties controlling granitoid petrology are (1) silica content, (2) Fe/Mg ratio; (3) alkalinity, the ratio between Na + K and Ca; (4) the ratio between Al and alkali content (Ca+Na+K); and (5) Na/K ratio. Currently, the granitoid classification approach can be broadly

divided into tectonic discrimination (e.g. Chappell & White 1974; Whalen et al. 1987; Chappell & White 2001) and descriptive classification (Frost et al. 2001a; Frost & Frost 2011).

Tectonic discrimination (e.g. Pearce et al. 1984; Whalen et al. 1987), or genetic classification, uses major- and trace-element patterns to infer tectonic environments of the formation of granitoids. This scheme directly links the geochemistry to tectonic settings in a well-understood tectonic context, highlighting signatures associated with specific environments (e.g. low Nb in volcanic arcs, Pearce et al. 1984). However, in felsic magma, trace element concentrations are strongly influenced by accessory minerals and intensive parameters (Bea 1996). Furthermore, applying this approach to granitoids with hybridised mantle and crustal sources is challenging because of the ambiguity that arises from mixed geochemical signatures (e.g. post-collision granites, Pearce et al. 1984).

On the other hand, descriptive classification (e.g. Frost et al. 2001a) utilises major element geochemical characteristics, making it particularly useful in ambiguous tectonic settings. Some possible petrogenetic models can be considered for the generation of granites with an "A-type" signature. Frost and Frost (2011) suggest ferroan metaluminous alkalic plutons form in three tectonic contexts: (1) anorthosites-associated granitoids formed by hybridisation of ferro-basaltic and granitic magmas, (2) alkaline plutons derived from extreme fractionation of basaltic magma (e.g. in continental rifts), and (3) calc-alkalic plutons resulted from the partial melting of quartzofeldspathic crust.

This thesis uses both classification approaches, supplemented by geochemical and isotopic data, to elucidate the crystallisation conditions and the sources of high-*T* granitoids in the central Grenville Province.

1.3.2.2. Whole-rock Sm–Nd isotopes

Isotopic analysis of samarium (Sm) and neodymium (Nd) in granitic rocks provides insights into understanding the sources of granitoid magma (DePaolo & Wasserburg 1976b, a; DePaolo 1988; DePaolo et al. 1991). The long-lived, radiogenic ^{147}Sm undergoes alpha decay to non-radiogenic ^{143}Nd, while the stable ^{144}Nd does not undergo decay; thus, the relative fractionation between Sm and Nd isotopes is very small during crystallisation and melting and

the decay processes. The evolution of the $^{143}Nd/^{144}Nd$ ratio of granitoids follows the chondritic uniform reservoir (CHUR) and the depleted mantle (DM) models, which can be referenced to crustal-forming events and crustal-mantle interaction models (DePaolo & Wasserburg 1976a; DePaolo 1981). Due to the slight variation in Nd isotopic ratios, the epsilon-notation of Nd (ε_{Nd}) was developed by DePaolo and Wasserburg (1976b) to represent data normalised to the CHUR value

$$\varepsilon_{Nd}(t) = \left[\frac{\left(\frac{^{143}Nd}{^{144}Nd}\right)_{t,sample}}{\left(\frac{^{143}Nd}{^{144}Nd}\right)_{t,CHUR}} - 1 \right] \times 10^4$$

where t denotes the time from which the $^{143}Nd/^{144}Nd$ ratio is calculated. The ε_{Nd} can be plotted against time to visualise the evolution of isotopic signatures in granitoids.

The addition of juvenile crust (≤200 Myr) versus crustal recycling can be determined by the extraction ages with reference to country rock isotopic compositions. The addition of a new crust would produce a higher, DM-like $^{143}Nd/^{144}Nd$ ratio (high ε_{Nd}). In contrast, if a rock formed by the melting of an existing crustal source, and the melting process left the Sm/Nd ratio unchanged, the model age would approximate the time when the melt was originally derived from the depleted mantle (DePaolo 1988).

1.3.3. Estimating crystallisation conditions

Intensive parameters, including temperature (*T*), pressure (*P*), oxygen fugacity (fO_2) and volatile element contents, control the magma evolution. In the case of high-*T* granitoids, intensive parameters of crystallisation can be estimated by applying relevant thermometers, barometers, and oxybarometers. Thermometry is relatively insensitive to *P*, but most barometry is *T*-dependent (Anderson 1996). Oxygen fugacity, which reflects the availability of oxygen in the magma and its redox state, is dependent on the *P* and *T* (Frost 1991). On such grounds, the constraints placed by mineral chemistry on crystallisation *T* are crucial to characterising high-*T* granitoids. This section lists the methods of estimating intensive parameters and reviews their theoretical background.

1.3.3.1. Zircon Saturation Temperature

The zircon saturation temperature (T_{Zr}) is a proxy tool to indicate the temperature at which Zr reaches saturation and zircon starts to crystallise from the melt (Watson & Harrison 1983; Hanchar & Watson 2003; Boehnke et al. 2013). This thermometer uses bulk-rock compositions to estimate the minimum liquidus temperature of the magma provided that inherited zircon is absent. Watson and Harrison (1983) derived the T_{Zr} (in K) as

$$T_{Zr} = \frac{12900}{ln\, D_{Zr} + 3.8 + 0.85 \cdot (M - 1)}$$

where $\mathrm{M} = \frac{\mathrm{Na+K+2Ca}}{\mathrm{Al \cdot Si}}$ is the ratio representing magma liquidus composition. $D_{Zr} = \frac{497{,}644}{[Zr]_{sat}}$ is the distribution coefficient of Zr in zircon to melt, which can be estimated by stoichiometric Zr concentration (497,644 ppm) divided by bulk-rock Zr concentration, assumed to be the Zr concentration at saturation.

It is important to note that the calculation assumes that: (1) zircon is homogeneously distributed in the rock and has not been concentrated or removed; (ii) the rock composition represents the magmatic composition; (iii) no inherited zircon is present; and (iv) zircon crystallises near the magma liquidus (Evans & Hanson 1993; Bea 1996; Miller et al. 2003). Inherited zircons (or xenocrysts) may be present in peraluminous rocks (e.g. Vavra 1994), therefore, to avoid overestimation of T_{Zr}, the presence of such zircons should be assessed by investigating their internal textures and their textural relationship to other rock-forming minerals by using cathodoluminescence (CL) or back-scattered electron microscopy (BSE) images (Corfu et al. 2003; Hanchar & Watson 2003).

1.3.3.2. Amphibole-based thermometry and barometry

The hornblende-plagioclase thermometer, used to estimate the solidus temperature was developed by Blundy and Holland (1990) and improved by Holland and Blundy (1994). The thermometer is based on the *T*-dependent partitioning of Al and Ca between hornblende and plagioclase. The thermometer assumes equilibrium between hornblende and plagioclase during crystallisation, governed by the reaction $edenite + albite = richterite + anorthite$. The thermometer follows a careful procedure of recalculating ferric-ferrous ratios and site allocations on the basis of 23 oxygens to ensure that stoichiometric amphibole is used. The calculated

temperature is a function of hornblende-plagioclase mineral chemistry and pressure. However, in natural systems, partitioning of Al and Ca by other Al- or Ca-rich minerals (e.g. pyroxene), may lead to imprecise estimations (Anderson et al. 2008).

The Holland and Blundy (1994) thermometer is often used in conjunction with the Al-in-hornblende barometer (Blundy & Holland 1990), yielding *P–T* conditions by simultaneous solution (Anderson et al. 2008). For metaluminous, plagioclase–hornblende bearing granite, an empirical barometer based on the Al content in hornblende was proposed by Blundy and Holland (1990):

$$P\ (kbar) = 5.03Al - 3.53$$

where Al is the sum of Al^{IV} and Al^{VI} per 13 cations (per formula unit) in hornblende. This geobarometer is not calibrated for ferroan rapakivi granites, which are Fe-rich, and the *P* may be overestimated due to improper estimation of fO_2 (Anderson & Smith 1995). Nevertheless, this could be taken as an upper limit for the *P* of crystallisation.

In addition, Ridolfi and Renzulli (2012) and Ridolfi (2021) proposed an amphibole-only thermobarometer for Mg-rich calcic amphiboles in calc-alkaline or alkaline magmas. However, Fe-rich calcic amphibole, which is common in high-*T* granitoids, remains uncalibrated.

1.3.3.3. Zircon as a petrogenetic indicator

Geochronology, trace element geochemistry and isotopic affinity of zircon extracted from high-*T* granitoids provide a wide range of petrogenetic insights. Zircon ($ZrSiO_4$) is a refractory mineral that survives metamorphism, magmatism and erosion (Roberts & Spencer 2014). In granitoids, zircon is a common accessory mineral and a powerful indicator of crystallisation age, temperature, and melt composition. Therefore, it can provide insights into the magmatic evolution as well as the inherited history, if any, before magmatism. The following is a discussion of how zircon morphology, isotopic systematics (U–Pb and Lu–Hf), geothermometry (Ti-in zircon) and Ce–U–Ti oxybarometry can contribute to the understanding of high-*T* granitoids.

External crystal habits and internal textures reflect the magmatic history of zircons. Corfu et al. (2003) reviewed zircon morphology comprehensively to delineate the history of the formation or resorption of the mineral. Identifying textural relations of zircon to surrounding

minerals is also essential to understanding the crystallisation rate because of variable Zr solubility and concentration in the systems (Hanchar & Watson 2003). Zircon's external shape is a function of composition and the kinetics of the crystallisation system (Vavra 1990; Hoskin 2003). Magmatic resorption or metamorphic reaction could lead to the destruction of external structures (Corfu et al. 2003). The internal textures are revealed under back-scattered electron microscopy (BSE) or cathodoluminescence to understand the growth history and distinguish igneous and metamorphic zircon (e.g. Vavra 1990; Corfu et al. 2003; Hoskin 2003). For example, oscillatory zoning is a typical magmatic texture in zircon (Vavra 1994; Hoskin 2003). On the contrary, low-luminescence core, sector-zoned or oscillatory-zoned overgrowth rim, or irregular, diffuse "aurora-light" texture are typical metamict domains in metamorphic zircons (Corfu et al. 2003; Hoskin 2003). Older, inherited cores may also be present in zircons (Vavra et al. 1999; Hoskin 2003; Miller et al. 2007).

U–Pb dating of zircon has been widely used to obtain the absolute age of magmatic events. Geochronology of orogenic granitoids is essential to pinpoint the stages of orogenic evolution. BSE and CL imaging are important for recognising zircon internal textures and for planning spots to be analysed. Modern dating methods include laser ablation–inductively-coupled plasma–mass spectrometry (LA–ICP–MS) and Isotope Dilution–Thermal Ionization Mass Spectrometry (ID–TIMS) (Davis et al. 2003). For LA–ICP–MS, in-situ detection could be achieved to date specific zones in zircon, but the precision is less than that for ID–TIMS. On the contrary, a higher age precision could be achieved using ID–TIMS by sacrificing spatial resolution. Therefore, zircon morphology is crucial to deciding which instrument to use.

The zircon Lu–Hf isotopic system can be used to assess magma sources, in addition to whole-rock Sm–Nd isotopes (Kinny & Maas 2003; Spencer et al. 2020). Lu–Hf isotopes in zircon are less susceptible to redistribution by metamorphism than the U–Pb system, unless in the case of fluid reaction (Kinny & Maas 2003). The comparison between Hf ratios assumes an equivalent Lu/Hf ratio between the bulk Earth and a chondritic source (CHUR) from which it has evolved (Blichert-Toft & Albarède 1997). The epsilon-notation of Hf (ε_{Hf}) represents the $^{176}Hf/^{177}Hf$ ratio normalised to the CHUR value (DePaolo & Wasserburg 1976a; Patchett & Tatsumoto 1981; Bouvier et al. 2008). A domain indicative of a mantle-derived magma source would hold a

positive $\varepsilon_{Hf}(t)$ at the time of crystallisation (t), whereas negative $\varepsilon_{Hf}(t)$ represents crustal affinity. Assuming the evolution of the average continental crust (Lu/Hf = 0.015) as a realistic estimate, the Hf–T_{DM} age represents the minimum age of the magma extracted from the depleted mantle (Vervoort et al. 2018). Coupling high-precision U–Pb geochronology and Lu–Hf isotopic geochemistry is a powerful tool for deciphering magmatic sources through time.

In addition, Watson and Harrison (2005) experimentally calibrated the Ti concentration in zircon as a reliable indicator of its formation temperature, accounting for the activity of TiO_2. The Ti-in-zircon thermometer is supported by theoretical calculations (Harrison et al. 2005) and further experiments in rutile-bearing, Ti-saturated rocks (Ferry and Watson 2007), which suggest the following reaction involving rutile, zircon and quartz:

$$TiO_2 + ZrSiO_4 \leftrightarrow ZrTiO_4 + SiO_2$$

Ti-in-zircon is strongly dependent on the activities of TiO_2 and SiO_2 in the melt (αTiO_2, αSiO_2) pressure and temperature (Ferry & Watson 2007; Ferriss et al. 2008). Hayden and Watson (2007) suggested an αTiO_2 of 0.6 for rutile-undersaturated and an αSiO_2 of 1 for quartz-present melt. A revised geothermometric equation to calculate Ti-in zircon temperature (TIZT, in K) is proposed by Loucks et al. (2020):

$$TIZT = \frac{-4800 + 0.4748(P - 1000)}{log[Ti]_{zrn} - 5.711 - \log \alpha TiO_2 + \log \alpha SiO_2}$$

where P (MPa) is the equilibrium pressure estimated by Al-in-hornblende barometry and $[Ti]_{zrn}$ (ppm) is the concentration of Ti in zircon.

In the same paper, Loucks et al. (2020) developed a magmatic oxybarometer using the concentrations of redox-sensitive elements (Ce, U, and Ti) in zircon to estimate the oxygen fugacity (fO_2) in granitoids. Granitoids that have high fO_2 are formed under a more oxidising condition, favouring ferric and sulphate species and are typical of arc granitoids derived from calc-alkaline magma (Ishihara 1977). In contrast, low-fO_2 granitoids are generated under more reducing conditions, stabilising ferrous and sulphide species and could be derived from alkali basalt parental magma or anhydrous source (Frost & Frost 2011; Dall'Agnol et al. 2012). The fO_2 of the fayalite–magnetite–quartz (FMQ) buffer at given P (kbar) and T (K) is empirically established by Frost (1991):

$$\log fO_{2_{FMQ}} = \frac{-25096.3}{T} + 8.735 + (P-1)\frac{0.11}{T}$$

In granitoids, zircon is more resistant to chemical changes than other minerals such as hornblende, which has been used for oxybarometric calibrations (e.g. Ridolfi & Renzulli 2012). Therefore, the fO_2 recorded in zircon is considered a reliable indicator of the magma's redox conditions. The fO_2 of zircon is calculated with respect to the FMQ buffer (ΔFMQ):

$$\Delta\text{FMQ} = \log fO_{2_{sample}} - \log fO_{2_{FMQ}}$$

$$= (3.998 \pm 0.124) \times \log\left(\frac{Ce}{\sqrt{U_i \times Ti}}\right)_{zrn} + (2.284 \pm 0.101)$$

where Ce and Ti are their measured concentrations, and U_i is the initial concentration of U at the time of crystallisation of zircon.

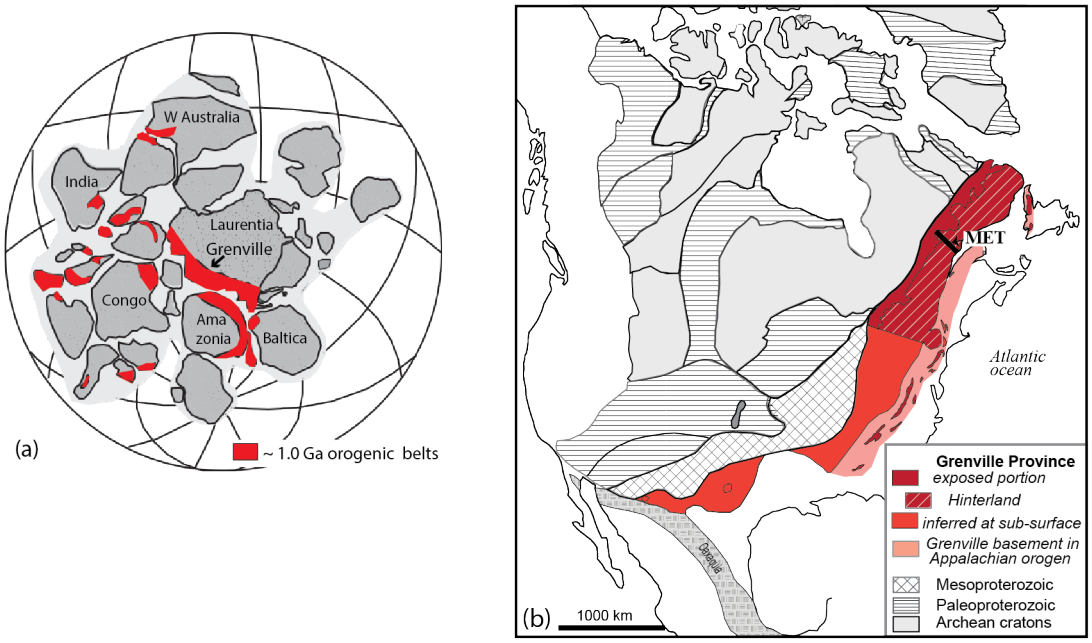

Figure 1.1 Location of the Grenville Province in the **(a)** Rodinia configuration adopted from Indares (2020), after Chappell & White (2001) and Li et al. (2008); and **(b)** North America (Hoffman et al. 1989). The Manicouagan-Escoumins Transect (MET) is located at the central Grenville Province. Modified from Indares (2020) and Whitmeyer and Kalstrom (2007).

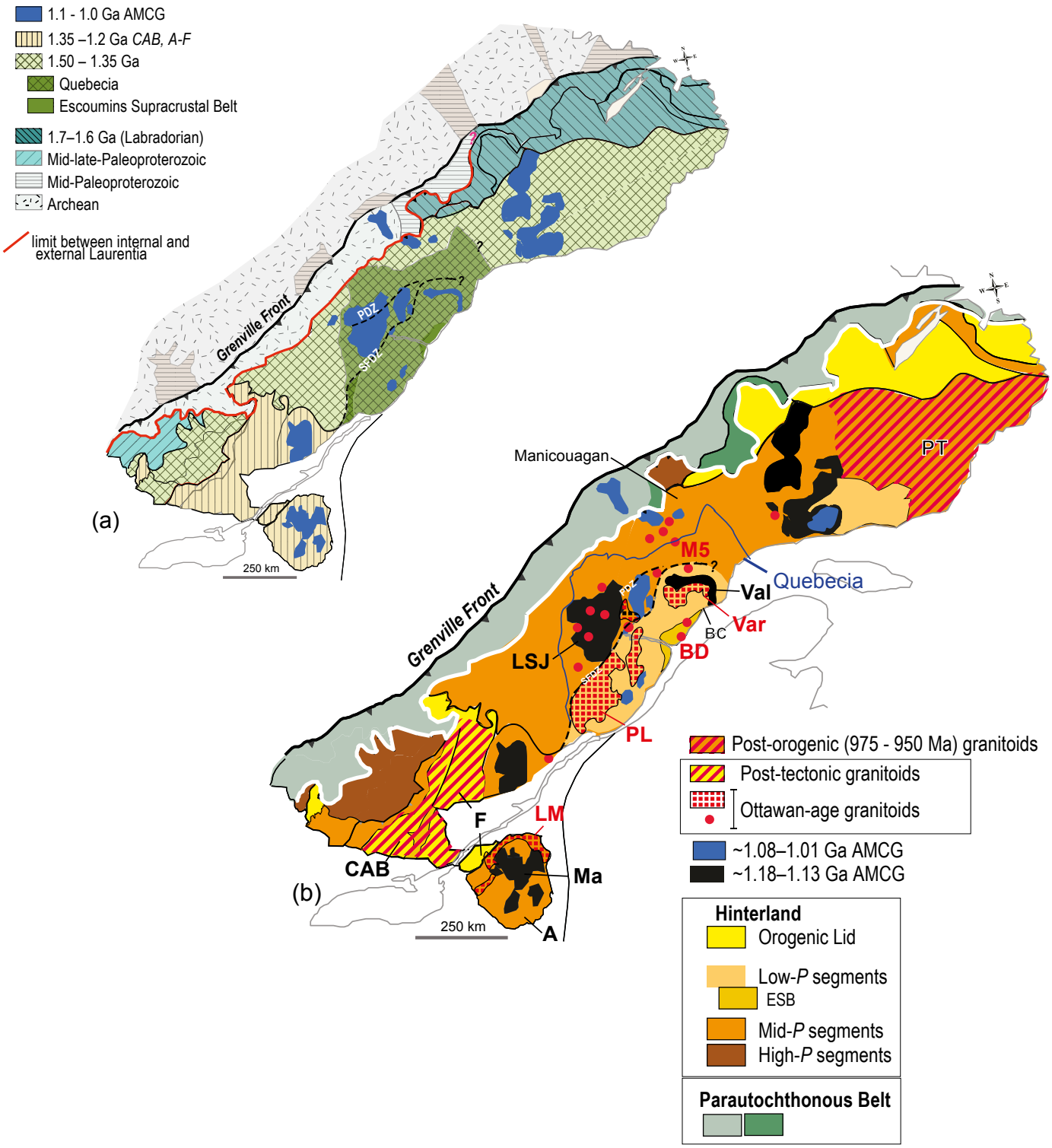

Figure 1.2 Overview of the Grenville Province, modified from Indares (2024). **(a)** Crustal domains of the Grenville Province, highlighting the formation ages of crustal domains. The outline of Quebecia is illustrated (Dickin et al. 2010). **(b)** Distribution of Grenvillian magmatism and the crustal structure of the orogenic hinterland. Abbreviations, SW Grenville: A – Adirondacks; F – Frontenac; CAB – Composite Arc Belt; LM – Lyon Mountains Granite. 1.1 Ga: HSP – Havre-Saint-Pierre anorthosite; LSJ – Lac-Saint-Jean Anorthosite; Ma – Marcy Anorthosite; Val – Vallant Anorthosite. Grenvillian high-*T* granitoids: PL – Parc des Laurentides Complex; PT – Pinware Terrane; Var – Varin Monzonite; BD – Bon-Desir Granite. Major structure (Dashed lines, italic): PDZ – Pipmuacan Deformation Zone; SFDZ – Saint-Fulgence Deformation Zone. ESB – Escoumins Supracrustal Belt; BC – Baie-Comeau.

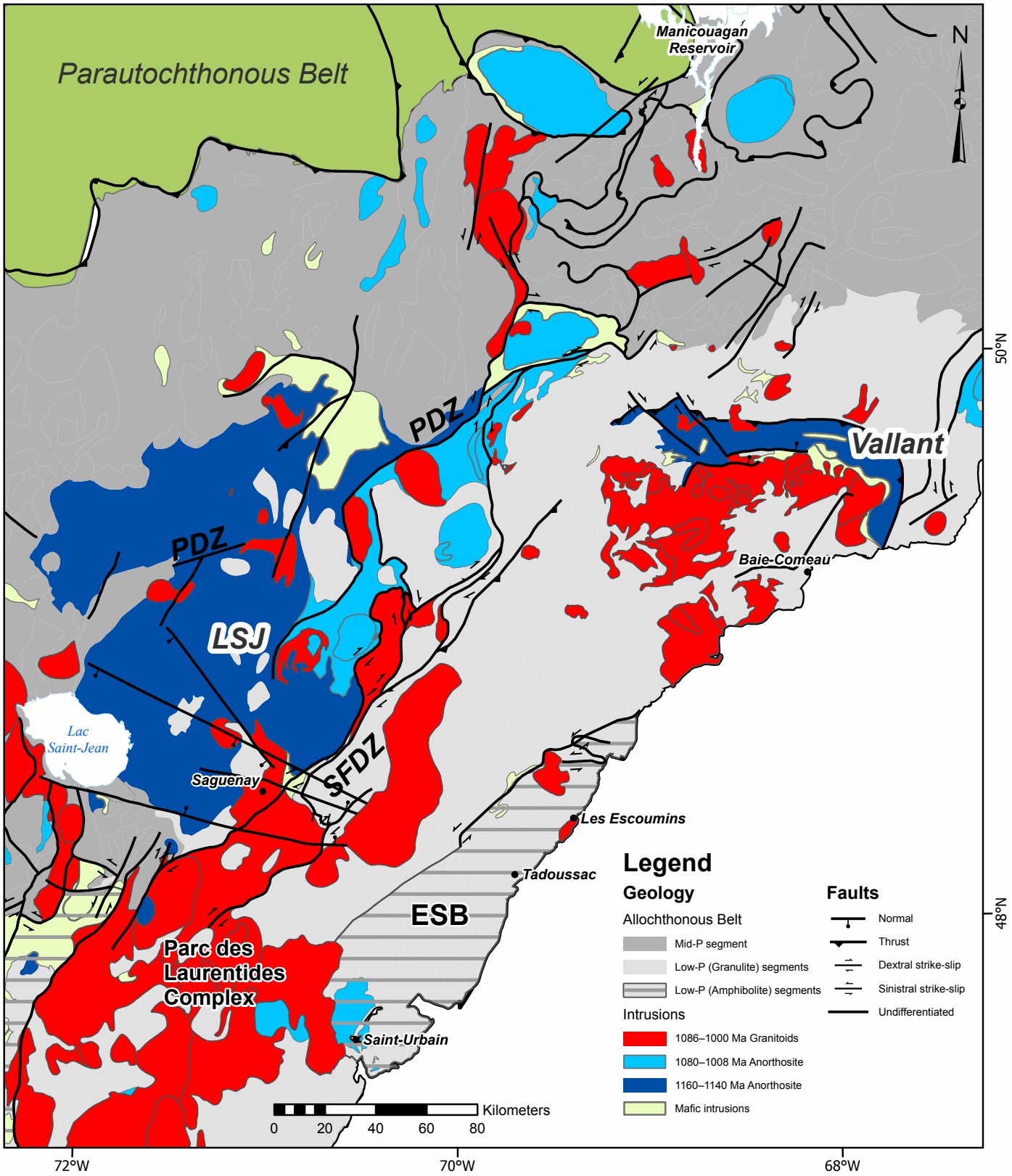

Figure 1.3 Overview of the Central Grenville Province, modified from SIGEÓM (MRNF 2021). Abbreviations, Crustal domains: ESB – Escoumins Supracrustal Belt. Anorthosite: LSJ – Lac-Saint-Jean Anorthosite. Syn-orogenic high-*T* granitoids: PLC – Parc des Laurentides Complex. Deformation zones: PDZ – Pipmuacan Deformation Zone; SFDZ – Saint Fulgence Deformation Zone.

Chapter 2. Approach, methodology and analytical techniques

2.1. Introduction

This project is comprised of two components: (1) synthesis of the age and geochemistry of orogenic high-*T* granitoids in the central Grenville Province from the literature, to assess potential spatiotemporal trends, geochemical signatures and zircon saturation temperatures at the scale of the study area; and (2) detail characterisation of samples collected from four granitoids exposed in different pressure segments. For the first component, a geochemical and a geochronology database were compiled from the Québec geoscientific database (SIGEÓM, https://sigeom.mines.gouv.qc.ca/signet/classes/I1102_indexAccueil?l=a), a geospatial database by the Québec Ministry of Natural Resources and Forests. For the second component, five samples of selected granitoids were documented in terms of petrography, whole-rock and isotopic (Sm–Nd) geochemistry, and zircon trace element and isotopic (U–Pb and Lu–Hf) composition. These data were used to delineate geochemical signatures using standard classification diagrams; crystallisation conditions (*P, T* and fO_2) using amphibole-based thermobarometry, ternary feldspar, Ti-in-zircon thermometry and zircon Ce–U–Ti oxybarometry; zircon inherited and crystallisation ages via U–Pb geochronology; and sources of magma by whole-rock Sm–Nd and zircon Lu–Hf isotopes.

2.2. Literature database (component 1)

Ages and geochemistry of the high-*T* granitoids in the Central Grenville Province were compiled from SIGEÓM (Table 3.1 & Appendix A; MRNF 2021). The locations of the samples are shown in Figure 3.1. The age data come from the dominant units of each plutonic suite, and most plutonic suites/units only have one or two ages available. Considering this limitation, only the geochemical data from the units with available geochronology were considered. Data information, including sample number, unit name, and UTM coordinates, is recorded in Appendix A. For geochemistry, eleven major element oxides, including SiO_2, TiO_2, Al_2O_3, Fe_2O_3 (total), MnO, MgO, CaO, Na_2O, K_2O, P_2O_5 and Cr_2O_3, and forty-seven trace elements, including Be, Sc, V, Co, Ni, Cu, Zn, Ga, Ge, As, Se, Rb, Sr, Y, Zr, Nb, Mo, Ag, Cd, Sn, Sb, Cs, Ba, La, Ce, Pr, Nd, Sm, Eu, Gd, Tb, Dy, Ho, Er, Tm, Yb, Lu, Hf, Ta, W, Au, Hg, Tl, Pb, Bi, Th, U are documented.

CIPW norms αre calculated by IgPet (Carr & Gazel 2016). All Fe-oxides are assumed to be FeO (total) to determine the first-order QAP trend.

Management, visualisation, and analysis of the literature data were completed using Python Jupyter Notebook. The data are managed by the data management module (Pandas) and plotted by visualisation modules (Matplotlib and Seaborn) with the aid of the geochemical module (pyrolite, Williams et al. 2020). In terms of geochemistry, data that are below the detection limit are discarded. A SiO_2 cut-off of 55% was used to distinguish intermediate to felsic rocks (≥55%; the ones considered here) and mafic rocks (<55%). Data with SiO_2 > 80% are also discarded because they represent alteration or other siliceous rocks. A review of suspicious outliers is conducted manually by cross-checking the Geofiche outcrop data in SIGÉOM. Geochemical signatures of the granitoids were assessed with the aid of standard granitoid classification diagrams from the literature.

2.3. Petrography and mineral chemistry (component 2)

Minerals and textures were examined with an optical microscope equipped with a camera, while the distribution of minerals at the section scale and their modal proportions were estimated by false-colour mineral maps generated using a scanning electron microscope–mineral liberation analyser (SEM–MLA). Mineral chemistry was obtained using an electron-probe micro-analyser (EPMA).

2.3.1. SEM–MLA imaging

Combining BSE imaging analysis and X-ray mineral identification provides automated mineral identification, visualising the mineral distribution and modal proportion. Imaging of thin sections was performed by FEI Quanta 400 scanning electron microscope (SEM) equipped with a mineral liberation analyser (MLA) at the CREAIT network facility at Memorial University of Newfoundland (MUN). Backscatter electron (BSE) images were acquired using an acceleration voltage of 25 kV and beam current of 13 nA under fast scanning mode with a resolution of 400×400 pixels per frame, an X-ray step size of 16 pixels and a scanning time of 8 μs. The MLA software processed a thin-section-wide BSE image and respective X-ray spectral data (JKTech Pty. Ltd., The University of Queensland, Australia). A false colour map was generated for each thin section that delineates the boundary of mineral grains and rasterises mineral compositions.

2.3.2. Chemistry of rock-forming minerals

Electron-probe micro-analysis (EPMA) for quantitative mineral major elements was conducted using JEOL JXA-8230, available through the CREAIT network facility at MUN. Analyses were carried out in a wavelength dispersive mode with an accelerating voltage of 15 keV, while beam current and beam sizes were 15 nA and 1 μm for amphibole, 20 nA and 3 μm for clinopyroxene, and 20 nA and 5 μm for biotite, K-feldspar and plagioclase.

Elements analysed for each mineral, the standards and the analysis setup are reported in Table 2.1. During the analytical sequence of each mineral, three analyses of equivalent standard minerals were performed and treated as unknowns to evaluate the accuracy of the measurement every twenty to thirty analyses. Raw data were converted into concentrations using the ZAF matrix correction procedure.

For each thin section, three to five grains of each mineral were measured. At least three analysis points are assigned to each mineral grain. If zoning is present, a step scan line analysis was taken across the grain with five to seven points. The EPMA results are given in Appendix B.

Table 2.1 Standards used for mineral chemistry analysis with the EPMA

Standards for EPMA																
Minerals																
Amphibole					Biotite				Clinopyroxene				Feldspar			
Number of Oxygens: 23					Number of Oxygens: 22				Number of Oxygens: 6				Number of Oxygens: 8			
Primary Standards																
Element	Standard	Crystal	t (s)		Element	Standard	Crystal	t (s)	Element	Standard	Crystal	t (s)	Element	Standard	Crystal	t (s)
F	Fluorapatite	LDE1	10		F	Fluorapatite	LDE1	10	Fe	Almandine	LIFL	20	Fe	Almandine	LIFL	20
Fe	Almandine	LIFL	20		Fe	Almandine	LIFL	20	Ca	Diopside	PETL	10	Ba	Barite	LIFL	30
Cl	Tugtupite	PETL	20		Ba	Barite	LIFL	30	Na	Albite	TAP	20	K	Orthoclase	PETL	20
K	Orthoclase	PETL	20		Cl	Tugtupite	PETL	20	Al	Almandine	TAP	20	Ca	Diopside	PETL	20
Ca	Diopside	PETL	20		K	Orthoclase	PETL	20	Si	Diopside	TAP	20	Na	Albite	TAP	10
Na	Albite	TAP	10		Ca	Diopside	PETL	20	Mg	Pyrope	TAP	20	Al	Pyrope	TAP	20
Al	Pyrope	TAP	20		Na	Albite	TAP	10	Mn	Rhodenite	LIFH	30	Si	Orthoclase	TAP	20
Si	Diopside	TAP	20		Al	Almandine	TAP	20	Ti	Rutile	LIFH	30	Sr	Celestite	PETH	30
Mg	Pyrope	TAP	20		Si	Diopside	TAP	20								
Mn	Rhodenite	LIFH	30		Mg	Pyrope	TAP	20								
Ti	Rutile	LIFH	30		Mn	Rhodenite	LIFH	30								
					Ti	Rutile	LIFH	30								
Secondary standards																
Astimex kaersutite					Astimex biotite				Astimex Cr diopside				K-feldspar: Indian K-feldspar Plagioclase: Astimex albite			

2.4. Whole-rock geochemistry (component 2)

2.4.1. Major and trace element compositions

Samples were crushed and powdered in a tungsten carbide swing mill at MUN. Whole-rock geochemistry analysis was completed at Actlabs Inc. (Ancaster, Ontario, Canada). Flux material Li-metaborate and Li-tetraborate were added to each sample for fusion. Major and trace element compositions were analysed by inductively coupled plasma atomic emission spectrometry (ICP–AES) and inductively coupled plasma mass spectrometry (ICP–MS), respectively. Ten major oxides, SiO_2, Al_2O_3, FeO_T, MnO, MgO, CaO, Na_2O, K_2O, TiO_2, P_2O_5, and loss on ignition (LOI), are reported with a detection limit of 0.01 wt %. Forty-five trace elements were also measured, including Sc, Be, V, Ba, Sr, Y, Zr, Cr, Co, Ni, Cu, Zn, Ga, Ge, As, Rb, Nb, Mo, Ag, In, Sn, Sb, Cs, La, Ce, Pr, Nd, Sm, Eu, Gd, Tb, Dy, Ho, Er, Tm, Yb, Lu, Hf, Ta, W, Tl, Pb, Bi, Th, U. The results are presented in Appendix A.

2.4.2. Sm–Nd isotopic composition

Isotopic Sm–Nd data were obtained at the CREAIT Facility at MUN using the thermal ionisation mass spectrometry (TIMS) method. An aliquot is made by adding a mixed $^{150}Nd/^{149}Sm$ spike to a homogeneous, powdered sample. The spiked aliquot is then weighed on a high-precision balance. The mixtures were dissolved using HF–HNO_3 solution in Teflon beakers for five days to ensure the complete dissolution of refractory materials. After digestion, the solutions were dried on a hot plate and received concentrated 6 N HCl until they were evaporated to dryness. Then, 1 mL of 2.5 N HCl was added to each sample, and they were loaded on cationic exchange HDEHP LN resin columns to extract the REE fraction of the samples. Then, the collected REE fractions were purified and loaded on secondary columns filled with LN resin to isolate Sm and Nd analytes. The analytes are collected in separate polyethylene pots and evaporated to dryness.

A multi-collector Finnigan MAT 262 mass spectrometer was used in static mode to determine Sm and Nd concentrations and in dynamic mode to measure Nd isotopic compositions. Nd isotopic ratios were normalised to $^{146}Nd/^{144}Nd = 0.7219$ (O'Nions et al. 1977) to correct instrumental mass fractionation. Deviation from JNdi-1 standard $^{143}Nd/^{144}Nd = 0.512115$ (Tanaka et al. 2000) is corrected for the reported Nd isotope ratios. Replicates of the standard yielded a

mean value and 2σ uncertainty, reported in the last decimal place, of $^{143}Nd/^{144}Nd = 0.512097 \pm 7$ ($n = 15$) for JNdi-1. Errors on the Nd isotopic ratios have uncertainties <0.002%.

The ε_{Nd} values (DePaolo & Wasserburg 1976b) for each rock are calculated using the age of crystallisation, the decay constant of ^{147}Sm of 0.00654 Gyr^{-1}, a present-day chondritic uniform reservoir (CHUR) composition of $^{143}Nd/^{144}Nd = 0.512638$ (Goldstein et al. 1984) and $^{147}Sm/^{144}Nd = 0.1967$ (Jacobsen & Wasserburg 1980). The Nd-depleted mantle model ages (T_{DM}) were calculated based on DePaolo (1988).

2.5. Zircon data (component 2)

Zircons were investigated in order to determine their age, trace element and isotopic record. Individual zircon populations were extracted from the samples and were imaged prior to analysis. In-situ trace element, U–Pb and Lu–Hf analyses were performed using LA–ICP–MS during separate sessions. The analytical spots were planned within the same internal textural domain in a zircon grain, assuming no differences in the elemental or isotopic composition of the different volumes. U–Pb was prioritised if only one spot could be fitted in the domain.

2.5.1. Preparation (mineral separation, picking, chemical abrasion)

Fresh samples were cleaned and then crushed in a BICO Chipmunk jaw crusher and powdered in a disc mill to obtain a powder of <500 μm diameter at MUN. Heavy mineral concentrates were obtained using the Wilfley table, and heavy-mineral separation was done with methylene iodide. Further filtered by a 425 μm mesh, zircon grains were obtained by an isodynamic Frantz separator. About 100 to 150 zircon grains were handpicked under a binocular microscope, covering as many kinds of external morphology in the population as possible.

The handpicked zircon grains were then chemically abraded (c.f. Mattinson 2005). Chemical abrasion reduces radiation-damaged or altered zones that are unrestorable by annealing so that secondary Pb loss is minimised. The zircons were then annealed in the oven at 1000 °C for 36 hours in silicon crucibles and were subsequently etched in concentrated hydrofluoric acid in a Teflon pressure-dissolution bomb in an oven at 200 °C for 4 hours. Zircon grains that survived were mounted in epoxy resin. The grain mounts were polished to the core of the grains, and the surface was finished to a high polish with 1 μm diamond paste.

Zircon internal texture was imaged by a Deben cathodoluminescence (CL) detector on the JEOL JSM-7100F field emission SEM at the TERRA facility (CREAIT, MUN). The current used varied from 10 to 15 kV. CL images reveal the internal structures, such as chemical zoning and inherited cores, and are useful for interpreting the growth history of zircon. Montages of zircon CL images are shown in Appendix C.

2.5.2. LA–ICP–MS zircon U–Pb geochronology

In-situ zircon U–Pb ages were measured by laser-ablation (LA)–ICP–MS at the Micro Analysis Facility (MAF) within CREAIT, MUN using a Thermo-Scientific Element XR ICP–MS coupled to a GEOLAS 193 nm ArF excimer laser system (Coherent, Göttingen, Germany). Depending on the size of the domain, the U–Pb isotopic data were collected using a spot size and laser fluence of 20 and 5 J cm^{-2}, or 30 μm and 4 J cm^{-2}, respectively, at a repetition rate of 5 Hz and 200 pulses. Typical sample acquisition includes 40s of background, 40s of ablation interval followed by washout, masses ^{202}Hg, ^{204}Pb, ^{206}Pb, ^{207}Pb, ^{208}Pb, ^{232}Th, ^{235}U, ^{238}U, were measured for 2 – 15 ms. The 91500 zircon (Wiedenbeck et al. 1995) with a $^{206}Pb/^{238}U$ age of 1062.4 ± 0.4 Ma was used as the primary standard for correcting laser-induced elemental fractionation and instrument drift. Secondary zircon reference materials Plešovice (Sláma et al. 2008), 02123 (Ketchum et al. 2001) and Temora (Black et al. 2003) were interspersed every 12 unknowns. The weighted mean $^{206}Pb/^{238}U$ ages yielded the following: 91500 (1062.4 ± 8.7 Ma; MSWD = 0.5, n = 42) and Plešovice (339.7 ± 2.8 Ma; MSWD = 1.9, n = 42), consistent with published ages.

Data evaluation was done offline with the iolite3 plug-in for Igor Pro (Paton et al. 2010), which contains a down-hole fractionation correction function. Results were calculated following Ludwig (1998) using IsoplotR (Vermeesch 2018). Error ellipses represent two times the standard error (2SE). on a Wetherill Concordia diagram. Age uncertainties are reported at the 95% confidence interval level. The zircon U–Pb geochronology results of the samples and reference materials are presented in Appendix D.

2.5.3. Zircon trace element geochemistry

2.5.3.1. EPMA for zircon internal standard calibration

Quantitative analyses for major elements in zircon grains serve as internal standards for calibration in trace element measurements. EPMA was conducted using the JEOL JXA-8230 at MUN. Analyses were carried out in a wavelength dispersive mode with an accelerating voltage of 17 keV, while the beam current was 50 nA on a focused beam. Five elements were measured, including: P, Zr, Hf, Si, Y. The standards and analysis setup are reported in Table 2.2. Raw data were converted into concentrations using the ZAF matrix correction procedure. In each analytical sequence, three analyses of synthetic zircon (Hanchar et al. 2001) as the equivalent standard mineral were performed and treated as unknowns to evaluate the accuracy of the measurement every twenty to thirty analyses.

Table 2.2 Standards used for zircon chemistry analysis with the EPMA

Standards for EPMA			
Zircon			
Number of Oxygens: 4			
Element	Standard	Crystal	t (s)
P	Apatite	PETJ	60
Zr	Synthetic Zircon	PETL	10
Hf	Synthetic Hafnon	LIFL	60
Si	Synthetic Zircon	TAP	10
Y	YP_5O_{14}	PETH	60
*Background counts were measured for half of the peak times on both sides of the peak.			
Secondary standards			
Synthetic Zircon			

For a preliminary screening, ten to fifteen grains were randomly selected, and one spot in every selected grain was analysed. If the ZrO_2 and SiO_2 are close to stoichiometric composition (~67 wt% ZrO_2, ~33 wt% SiO_2), the average chemical composition was assumed to be the same for the same domain across the zircon grains. The average ZrO_2 concentration was used as the internal standard. In the case of non-stoichiometric data, all domains in every grain were analysed to account for chemical variation across the zircon population.

2.5.3.2. LA–ICP–MS zircon trace elements

The trace element data were collected on the same LA–ICP–MS at MUN after the collection of U–Pb data. Ablation parameters were adjusted, and spot size and laser fluence were

set to 20 μm and 5 J cm^{-2} at a repetition rate of 5 Hz and 150 pulses. Analytical locations were selected adjacent to a U–Pb spot in the same CL domain. The primary standards used were standard reference materials NIST610 and NIST612 (Pearce et al. 2007) to correct laser-induced elemental fractionation, instrument drift and internal normalisation. The secondary standards used were Zircon 91500 (Wiedenbeck et al. 2007; Szymanowski et al. 2018) and BCR2G (Jochum et al. 2005). Zr measured by EPMA was used as the internal standard. A total of 22 species were measured, including ^{90}Zr, ^{178}Hf, ^{49}Ti, ^{89}Y, ^{93}Nb, ^{181}Ta, ^{139}La, ^{140}Ce, ^{141}Pr, ^{146}Nd, ^{147}Sm, ^{153}Eu, ^{157}Gd, ^{159}Tb, ^{163}Dy, ^{165}Ho, ^{166}Er, ^{169}Tm, ^{172}Yb, ^{175}Lu, ^{232}Th, ^{238}U. Primary and secondary reference materials were interspersed every 12 unknowns. Data evaluation was performed offline with iolite. The zircon trace elements results of the samples and reference materials are displayed in Appendix E.

2.5.4. MC–LA–ICP–MS zircon Lu–Hf isotopes

The Lu–Hf data were collected by the Thermo-Finnigan Neptune multi-collector (MC)–LA–ICP–MS at MUN. The Lu–Hf isotopic data were obtained by a 30 μm diameter laser-ablation spot, operating at a frequency of 15 Hz and fluence of *ca.* 4 Jcm^{-2}. A typical Lu–Hf analysis consisted of a 25-second background measurement phase followed by a 20-second data acquisition phase. Eight Faraday cups in static mode collect the ^{171}Yb, ^{173}Yb, ^{174}Yb, ^{175}Lu, ^{176}(Yb + Lu + Hf), ^{177}Hf, ^{178}Hf and ^{179}Hf beams. ^{176}Hf was corrected for mass bias, and ^{176}Yb and ^{176}Lu isobaric interference (Woodhead et al. 2004; Fisher et al. 2014). Taking $^{173}Yb/^{171}Yb = 1.132685$ as a reference (Chu et al., 2002), the Yb mass bias (β_{Yb}) was calculated. Then, the contribution of ^{176}Yb on ^{176}Hf was subtracted using the intensity of the interference-free ^{173}Yb and a ratio of $^{176}Yb/^{173}Yb = 0.79618$ (Chu et al. 2002). Similarly, assuming that $\beta_{Lu} = \beta_{Yb}$, the contribution of the ^{176}Lu on the ^{176}Hf signal was estimated using the intensity of the interference-free ^{175}Lu with a $^{176}Lu/^{175}Lu = 0.02656$ (Blichert-Toft & Albarède 1997). The mass bias correction on the $^{176}Hf/^{177}Hf$ ratios was determined using a ratio of $^{179}Hf/^{177}Hf = 0.7325$ (Patchett & Tatsumoto 1981). Exponential law of mass bias corrections for Yb, Hf and Lu was applied. In cases where the Yb/Hf ratios were low, β_{Hf} were used instead of β_{Yb} for Yb mass bias corrections. Quality control for the mass bias corrections was conducted by assessing the $^{178}Hf/^{177}Hf$ ratio on the reference materials, yielding a value of 1.46717 ± 9 (MSWD = 1.6, n = 59), consistent with the

published value (1.46735 ± 16; Thirlwall & Anczkiewicz 2004). Plešovice (Sláma et al. 2008) served as the primary zircon standard to correct instrument drift throughout the analytical session. Secondary reference materials (b142, R33, Temora) were interspersed in the analysis sequence. Analytical errors were computed by quadratic additions of the internal error (2SE) and the reproducibility (2σ) of the primary standard. The initial $^{176}Hf/^{177}Hf$ isotope ratios and εHf values were determined using the ^{176}Lu decay constant of 1.867×10^{-11} yr^{-1} (Albarède et al. 2006) and the Lu–Hf Chondritic Uniform Reservoir (CHUR) parameters (Bouvier et al. 2008). The following weighted mean $^{176}Hf/^{177}Hf$ values with 2σ uncertainty, reported in last decimal place, were obtained as follows: Plešovice (0.282483 ± 8; MSWD = 1.9, *n* = 25), b142 (0.282149 ± 17; MSWD = 2.1, n = 13), R33 (0.282754 ± 19; MSWD = 0.8, n = 10), Temora (0.282694 ± 17; MSWD = 1.8, n = 11). For each sample, the $^{176}Hf/^{177}Hf$ isotope ratios and $\varepsilon_{Hf}(t)$ values were calculated using published TIMS zircon U–Pb ages. In the absence of TIMS ages, weighted average $^{206}Pb/^{238}U$ ages (<1500 Ma) or $^{207}Pb/^{206}Pb$ ages (≥ 1500Ma) were used, particularly for inherited zircons. The zircon Lu–Hf results of the samples and reference materials are displayed in Appendix F.

Chapter 3. Synthesis of orogenic high-*T* granitoids in the central Grenville Province

3.1. Introduction

This chapter provides an overview of literature data on orogenic high-*T* granitoids from the central Grenville Province. The granitoids of interest are exposed in three distinct geological settings: (1) the mid-*P* segment, south of the Manicouagan reservoir; (2) the low-*P* segments in the Baie-Comeau and Escoumins regions; and (3) the Lac-St-Jean region, where they are spatially associated with ca. 1.16 to 1.00 Ga anorthosites. The purpose is to identify spatiotemporal trends, if any, in the crystallisation ages, assess the broad geochemical framework of these granitoids, and explore their tectonic significance in the context of the orogeny. The granitoids are exposed as 1 – 100 km^2 plutons in the low- and mid-*P* segments and as 3,000 – 5,000 km^2 of composite bodies in the vicinity of ca. 1.16 to 1.13 Ga anorthosites, in the low-*P* segment.

3.2. Rock types and ages of the subject plutonic suites

This section summarises literature data on rock types, field relationships, and intrusion ages of the granitoids considered here. Intrusion ages are TIMS zircon U–Pb ages unless otherwise specified. The granitoid bodies are described by region, from north (mid-*P* segment) to south (low-*P* segments), and west (Lac-St-Jean region) and their locations are shown in Figure 3.1. The rock types and ages are summarised in Table 3.1 in spatial order.

3.2.1. Granitoids of the mid-P segment, south of Manicouagan

These granitoids are located between the Manicouagan Reservoir and the eastern extension of the Pipmuacan Deformation Zone (Fig. 3.1), covering a total surface area of ~1,600 km^2, with individual plutons not larger than ~500 km^2. They include the older ~1065 Ma Manic 5 Plutonic Suite and three younger, ~1018 to 1015 Ma intrusions, the Trémaudan and Okaopéo Plutonic Suites, and the Sabot Mangerite.

3.2.1.1. Manic 5 Plutonic Suite

The *Manic 5 Plutonic Suite* is located north of the Manic 5 dam and mainly consists of medium-grained granite to quartz-monzonite. Two units were identified, with Unit 1, a grey, biotite-hornblende porphyroclastic granite to quartz-monzonite, dated at 1065 ± 8 Ma (Dunning & Indares 2010). This unit locally contains irregular mafic enclaves with magma mixing or commingling texture and shows diffusive contacts between felsic components. Unit 2 is a pink, medium-grained granite, which crosscuts Unit 1 with gradational contacts in the field (Dunning & Indares 2010).

3.2.1.2. Younger intrusions (Trémaudan, Sabot and Okaopéo)

These intrusions are generally associated with strike-slip faults (Moukhsil et al. 2013b). The *Trémaudan Plutonic Suite* is a 20-km-wide rounded batholith dominated by porphyritic quartz syenite, dated at 1018.4 ± 0.6 Ma (TIMS) and 1028 ± 8 Ma (LA–ICP–MS; Davis et al. 2014), with lesser gabbronorite and pyroxenite at the border. The *Sabot Mangerite* outcrops as several kilometric-scale plutons with a total surface area of ~987 km^2, locally intruding the Trémaudan Plutonic Suite (Moukhsil et al. 2009; Moukhsil et al. 2013b). The Sabot plutons are dominated by megacrystic orthopyroxene-bearing monzonite with minor granite and rare gabbronorite (Moukhsil et al. 2009; Moukhsil et al. 2013b). Two orthopyroxene-bearing monzonites of the Sabot plutons were dated at 1017 ± 2 Ma and 1016 ± 4 Ma (Gobeil et al. 2002). Finally, the *Okaopéo Plutonic Suite* comprises a few subcircular to elongated plutons with a surface area of over 100 km^2 and locally crosscuts Sabot Mangerite (Moukhsil et al. 2014). It consists of medium-grained orthopyroxene-bearing granite to quartz monzonite that was dated at 1015 ± 2 Ma (Augland et al. 2015).

3.2.2. Granitoids of the low-P segments, Baie-Comeau and Escoumins regions

The high-*T* granitoids in the low-*P* segments are located in two distinct settings: (a) the Varin Plutonic Suite, a large plutonic complex covering an area of hundreds of kilometres directly south of the ~1150–1135 Ma Vallant Anorthosite, and the Miquelon Plutonic Suite consisting of smaller, kilometric-scale intrusions scattered on both sides of the Varin Plutonic Suite, are exposed in the Baie-Comeau region; and (b) mostly, deca-kilometric scale plutons, as for instance

the Bon-Désir Granite and the Michaud Monzonite, are exposed in the Escoumins Supracrustal Belt (ESB).

3.2.2.1. Granitoids in the Baie-Comeau region (Varin, Miquelon)

The *Varin Plutonic Suite* is bounded to the north by a ~1060 Ma gabbroic unit (Louis Plutonic Suite), and both are separated from the Vallant Anorthosite by an E-W striking normal fault (Moukhsil et al. 2009; Moukhsil et al. 2011). Exposed over a surface area of 3,600 km^2, Varin consists of a wide range of rock types and is broadly divided into three units: orthopyroxene-free (Unit 1), orthopyroxene-bearing (Unit 2) and their gneissose equivalents (Unit 3). Generally, the suite is made up of biotite-hornblende quartz monzonite to granite with porphyritic feldspars and contains enclaves of gneissic host rocks and other minor mafic rocks. Two samples were dated at 1057.6 ± 1.7 Ma (Unit 1) and 1007.7 ± 1.7 Ma (Unit 2, David et al. 2009) from the western and eastern part of the plutonic suite, respectively. This difference in age represents ~50 Myr of active magmatism or two phases of magmatism.

The *Miquelon Plutonic Suite* consists of multiple plutonic bodies not greater than 100 km^2, crosscutting Pinwarian-age gneisses (Moukhsil et al. 2009; Moukhsil et al. 2014). Miquelon consists of medium- to coarse-grained quartz monzonite and biotite-hornblende-bearing granite. A monzonite intrusive into the Vallant Anorthosite was dated at 1047.9 ± 4 Ma with inherited zircon at 1155 ± 7 Ma (David et al. 2010b).

3.2.2.2. Granitoids of the Escoumins Supracrustal Belt (ESB)

Documented high-*T* granitoids in the ESB include the deca-kilometric scale Bon-Désir and Michaud intrusions, and a decametric biotite-rich felsic sill. *Bon-Désir* is a megacrystic granite dated 1086 ± 2 Ma, with quartzite, gabbro and amphibolite enclaves. *Michaud* is a coarse-grained clinopyroxene-bearing quartz monzonite dated at 1063 ± 3 Ma, with enclaves of metasedimentary rocks. The biotite-*rich felsic* sill is of intermediate to felsic composition with an anomalously high amount of zircon and apatite, dated at 1045 ± 3 Ma (Groulier et al. 2018a).

Table 3.1 Summary of TIMS zircon U–Pb ages, total area and rock types of the orogenic high-*T* granitoid plutonic suites/units in the central Grenville Province by region

	Name of suites/units	Area (km^2)	Rock type	Age ± 2σ (Ma)
Mid-*P* segments	**Manic 5 Plutonic Suite** [1,2]	88	*Unit 1* – porphyritic granite to quartz-monzonite. *Unit 2* – granite.	1065 ± 8 –
	Trémaudan Plutonic Suite [2,3]	446	quartz-syenite to syenogranite with leuconorite	1018.4 ± 0.6
	Sabot Mangerite [2,4,5,6]	987	*Unit 1* – mangerite. *Unit 2* – charnockite and biotite granite.	1017 ± 2 & 1016 ± 4 –
	Okaopéo Plutonic Suite [2,7]	132	*Unit 1* – Opx-bearing monzonite and monzonite. *Unit 2* – gabbronorite, leuconorite, locally gabbro. *Unit 3* – syenogranite with minor syenite.	1015 ± 2 – –
Low-*P* (granulite) segments	**Varin Plutonic Suite** [2,4,8,9]	3,619	*Unit 1* – granite, quartz-monzonite. *Unit 2* – Opx-bearing granite/quartz-monzonite. *Unit 3* – granitic and quartz-monzonitic gneiss.	1057.6 ±1.7 1007.7 ±1.7 –
	Miquelon Plutonic Suite [2,4,10]	199	quartz-rich monzonite & granite	1047.9 ± 4
Low-*P* (amphibolite) segments	**Bon-Désir Granite** [11]	32	megacrystic granite with enclaves of gabbro, quartzite and amphibolite	1086 ± 2
	Michaud Monzonite [11]	142	Cpx-bearing monzonite, with xenoliths of metasedimentary rocks	1063 ± 3
	Biotite-rich felsic sill [11]	-	intermediate to felsic sill with enclaves of metasedimentary rocks	1045 ± 3
Lac-St-Jean Region	**Chicoutimi Mangerite** [12,13]	385	mangerite and monzonite to monzodiorite	1082 ± 3
	Pipmuacan Anorthosite Suite [14,15,16]			**1073 – 1059**
	Strike Mangerite	84	mangerite and charnockite; granite, quartz monzonite and monzonite, subordinate with diorite	1073 ± 1.5
	Pamouscachiou Granite	688		1069.1 ± 1.5
	Poulin-de-Courval Mangerite	116		1068 ± 3
	Étienniche Monzonite	2		1059 ± 2
	La Baie Granite [12]	1,341	Granite	1067 ± 3
	Rivière-à-Pierre Plutonic Suite [17]	>5,000	Opx-bearing granite and monzonite	1058 ± 2
	Péribonka Plutonic Suite [14,15,18,19]			**1028 – 1018**
	Astra Granite	116	intermediate to felsic plutons intruding the LSJ Anorthosite; granite, quartz-monzonite, locally porphyritic, rapakivi with/without Opx; enclaves of anorthosite and supracrustal rocks	1028 ± 2
	La Carpe Granite	95		1028 ± 2
	Psukè Granite	21		1024.2 ± 2.4
	Menton Granite	205		1019.6 ± 1.5
	Margane Monzonite	119		1018.4 ± 2.4
	Farmer Monzonite	30		$1018\ ^{+7}_{-3}$
	Alcantara-Dion Mangerite [4,10]	45	monzonite/mangerite (with/without opx) and some granite/charnockite	1022 ± 10
	Valin Anorthosite Suite [12,14,15]		alkaline anorthositic massifs with mangerite, charnockite or monzonite and minor monzodiorite and diorite	**1020 – 1010**
	Saint-Ambroise Monzonite	93		$1020\ ^{+4}_{-3}$
	Gouin Mangerite	300		1010 ± 2
	La Hache Monzonite	185		1010 ± 3

Note: inferred area of plutonic units/suites in km^2. Underlined ages correspond to the dated units in the suite for this investigation. Abbreviation: Opx – orthopyroxene; Cpx – clinopyroxene

Table 3.1 (cont'd)

Reference: **1** – Dunning and Indares (2010); **2** – Moukhsil et al. (2014); **3** – Davis et al. (2014), who also reported a zircon LA–ICP–MS $^{207}Pb/^{206}Pb$ age at 1028 ± 8 Ma for Trémaudan; **4** – Moukhsil et al. (2009); **5** – Moukhsil et al. (2013b); **6** – Gobeil et al. (2002); **7** – Augland et al. (2015); **8** – Gobeil et al. (2006); **9** – David et al. (2009); **10** – David et al. (2010b); **11** – Groulier et al. (2018a); **12** – Higgins and van Breemen (1996); **13** – Hervet et al. (1994); **14** – Hébert et al. (2009); **15** – van Breemen (2009); **16** – Hébert et al. (1998); **17** – Moukhsil and Côté (2018), estimated area also included the Parc des Laurentides Complex; **18** – Higgins et al. (2002); **19** – Emslie and Hunt (1990)

3.2.3. Granitoids associated with anorthosites in the Lac-St-Jean region and vicinity

Four groups of Grenvillian-age granitoid plutons are recognised in the Lac-St-Jean (LSJ) region. (Fig. 3.1) The most voluminous is the 1080–1060 Ma Parc des Laurentides Complex, exposed on the SW extension of the low-*P* segment and separated from the ~1160–1135 Ma LSJ Anorthosite by the SFDZ. The remaining granitoid bodies are exposed west of the SFDZ and are spatially associated with the LSJ Anorthosite. They are of a deca-kilometric scale and are components of smaller, Grenvillian-age anorthositic suites. These are the early to mid-Ottawan-age Pipmuacan Anorthosite Suite (1082 – 1045 Ma), the late Ottawan-age Péribonka Plutonic Suite (1028 – 1018 Ma) and the younger, Valin Anorthosite Suite (1016 – 1008 Ma).

The *Parc des Laurentides Complex* (PLC) covers an area of at least 5,000 km^2. The *Rivière-à-Pierre Plutonic Suite* is the main granitoid unit and comprises hecto-kilometric-scale plutons located in the Parc des Laurentides region and the Portneuf–Mauricie domain (Corrigan & Hanmer 1997; Hébert et al. 2009). Rock types range from porphyritic biotite-hornblende granite to quartz monzonite with or without orthopyroxene and contain enclaves of granulite, amphibolite and tonalite (Corrigan & van Breemen 1997; Moukhsil & Côté 2018). Components of these plutons are dated at 1066 ± 24 and 1043 ± 20 Ma (TIMS whole-rock Rb–Sr, Frith & Doig 1973) and at 1058 ± 2 Ma (Moukhsil & Côté 2018). In addition, an aplite dyke at 1056 ± 2 Ma constrained the maximum age of magmatism in the Portneuf–Mauricie domain (Corrigan & van Breemen 1997).

In the Saguenay region, the PLC straddles the SFDZ. The 1082 ± 3 Ma *Chicoutimi Mangerite* to the west is an orthopyroxene-bearing porphyritic monzonite that intruded the LSJ Anorthosite, and the 1067 ± 3 Ma *La Baie Granite* to the east is a porphyritic orthopyroxene-

bearing monzonite and granite with a rapakivi texture (Higgins & van Breemen 1992; Hervet et al. 1994; Higgins & van Breemen 1996; Hébert & Lacoste 1998a, b).

The *Pipmuacan Anorthosite Suite* is a group of anorthositic and granitic intrusions, located to the north and east of LSJ Anorthosite (Hébert et al. 1998; Hébert et al. 2009; van Breemen 2009). The main anorthositic body, Vanel Anorthosite (1080 – 1061 Ma), is sandwiched between the PDZ and the SFDZ (Fig. 3.1). Coeval granitoids are of deca-kilometric scale, dominated by porphyroclastic monzonite, quartz monzonite, granite, monzodiorite, with or without orthopyroxene and with enclaves of anorthosite. The granitoids include the *Strike Mangerite* (1073 ± 2 Ma), the *Pamouscachiou Monzonite* (1069 ±2 Ma), the *Poulin-de-Courval Mangerite* (1068 ±3 Ma), and the *Étienniche Monzonite* (1059 ± 2 Ma). In addition, a younger pluton, *Alcantara-Dion Mangerite,* consisting of monzonite with or without orthopyroxene (Moukhsil et al. 2009), intruded the Vanel Anorthosite to the north at 1022 ± 10 Ma (David et al. 2010a).

The *Péribonka Plutonic Suite* comprises smaller (20–200 km^2) intermediate to felsic plutons that intruded the LSJ Anorthosite between 1028 and 1018 Ma (Emslie & Hunt 1990; Higgins & van Breemen 1996; Ider 1997; Hébert et al. 2009; van Breemen 2009). It consists of monzonite to granite, including *La Carpe Granite* (1028 ± 2 Ma), *Astra Granite* (1028 ± 2 Ma), *Menton Porphyritic Granite* (1020 ± 2 Ma), *St. Ambroise Monzonite* (1020 $^{+4}_{-3}$ Ma), *Margane Monzonite* (1018 ± 3 Ma) and *Farmer Monzonite* (1018 $^{+7}_{-8}$ Ma). Each pluton is structurally and petrographically different, although the intrusive ages are similar. For instance, the La Carpe Granite contains magmatic orthopyroxene variably replaced by hornblende and biotite (Hébert et al. 2009), whereas the Astra Granite intruded metasedimentary sequences and calc-silicate rocks and contains amazonite (Ider 1997; Higgins et al. 2002). Menton Porphyritic Granite formed along the SFDZ with thrust faults crosscutting the pluton. To the west of Saguenay, St. Ambroise Pluton is a circular pluton consisting of rapakivi monzonite.

The *Valin Anorthosite Suite* is the youngest anorthositic association in the central Grenville Province (Hébert et al. 2005). It is exposed to the SSW of the Vanel Anorthosite, between the PDZ and the SFDZ. The Suite includes the Mattawa (1016 ± 2 Ma) and Labrieville (1010–1008 Ma) anorthosites, with the former intrusive into the LSJ Anorthosite. Besides,

granitoid intrusions include the *La Hache Mangerite* (1010 ± 3 Ma) and the *Gouin Charnockite* (1010 ± 2 Ma). The granitoids form kilometric-scale plutons consisting of orthopyroxene-bearing monzonite–granite and diorite, some intrusive into the Vanel Anorthosite.

3.2.4. Age trends

The geochronological record shows that high-*T* granitoids were emplaced intermittently in the central Grenville Province between ca. 1086 and 1007 Ma (Fig. 3.2), with a conspicuous gap between ca. 1042 and 1032 Ma, where no intrusion ages are recorded in the literature. Therefore, in terms of intrusion age, the granitoid magmatism can be divided into two phases: an older one between ca. 1090 and 1040 Ma, e.g., in the early to mid-Ottawan period, and a younger one between ca.1030 and 1000 Ma, e.g., in the late Ottawan to Rigolet phase.

3.3. Geochemistry

Geochemical data from the orogenic high-*T* granitoids in central Grenville were compiled to assess the geochemical trends of this magmatism. A total number of 216 sets of data fulfilled the study criteria (See Chapter 2.2; Appendix A). In all of the diagrams presented in this section, the data from the older (1090 – 1040 Ma) and the younger (1030 – 1000 Ma) granitoid rocks are shown separately in order to assess potential geochemical differences between them.

The majority of granitoids are fresh or weakly altered. The Chemical Index of Alteration (CIA) of the samples ranges from 45 to 53, reflecting that the granitoids are akin to typical unaltered granitoids and subject to no or little alteration (Fig 3.3; Nesbitt & Young 1982). One outlier is identified with a CIA of 58, which is a slightly altered sample. Therefore, most of the dataset represents the original bulk major element composition of the samples.

3.3.1. Major element geochemistry

In general, the granitoids are dominantly intermediate to felsic with variable alkali content regardless of the presence of orthopyroxene. The granitoids show a wide span of SiO_2 (55–77 wt%) and low MgO (<3 wt%), TiO_2 (<2.5 wt%) and volatile (loss of ignition; LOI <2 wt%) content (Figs 3.4 & 3.5). Although the rocks are dominantly high in K_2O (<8 wt%), K_2O/Na_2O (0.2–3.0) ratios increase as SiO_2 increases. Unit 1 of the Varin Suite as well as the Miquelon Suite have some of the highest K_2O/Na_2O ratios (>2).

On the QAP diagram, the rocks range from monzodiorite and monzonite to granite (Fig. 3.6a). Plagioclase is the dominant modal feldspar, and the maximum modal quartz is 40%. In the TAS diagram (Irvine & Baragar 1971; Middlemost 1994), an alkaline and a subalkaline trend are observed (Fig. 3.6b). The alkaline trend (monzodiorite–monzonite–syenite series) is defined by Trémaudan in the mid-*P* segment, Pipmuacan, Chicoutimi and Valin in the LSJ region. In contrast, a subalkaline trend (monzonite–quartz-monzonite–granite series) is defined by most suites in the mid- and low-*P* segments, including La Baie in the Saguenay region. Some plutonic suites follow both trends, such as Miquelon in the low-*P* segment and Péribonka, which have syenite and quartz-monzonite constituents.

The Frost et al. (2001a) diagrams provide a descriptive classification of the granitoids. First, most granitoids are ferroan, with Fe* > 0.7 in the Fe*–silica diagram (Fig. 3.7a). Exceptions include some samples from the Okaopéo and Sabot of the mid-*P* segment and Bon-Desir in the ESB of the low-*P* segments, which is a magnesian granite (Groulier et al. 2018a). Second, the granitoids are dominantly metaluminous to weakly peraluminous, forming a broad array of increasing ASI with silica (Fig. 3.7b). On the other hand, in the low-*P* segments, some felsic samples from Varin, Miquelon and Bon-Désir are weakly peraluminous. Almost no sample has an ASI of more than 1.1. Third, in the MALI–silica diagram, the data define two trends, an alkalic trend and an alkali-calcic to calc-alkalic (AC–CA) trend (Fig. 3.7c). The alkalic trend includes Pipmuacan, Valin, and Chicoutimi in the LSJ region, as well as Trémaudan and Miquelon (Unit 2, syenite), which have strongly alkalic signatures. The AC–CA trend includes Manic 5, Sabot, Okaopéo in the mid-*P* segment, La Baie and Varin and the plutonic rocks of the ESB in the low-*P* segments. The MALI trends are similar to those in the TAS diagram (Fig. 3.6b).

To summarise, the granitoids in the region are broadly ferroan, metaluminous to weakly peraluminous, and alkalic with variable calcic content in the descriptive classification. No apparent relationship is observed between the age or region of emplacement. During the Grenvillian Orogeny, ferroan magmatism is widespread in the central Grenville Province.

3.3.2. Trace element geochemistry

3.3.2.1. Genetic classification diagrams

The data are plotted on the genetic classification diagrams, including Zr–Ga/Al (Whalen et al. 1987) and Nb–Y (Pearce et al. 1984; Whalen & Hildebrand 2019). The majority of data have ~300 to 2000 ppm Zr and fall into the "A-type" field in the Zr–Ga/Al plot (Fig. 3.8a), whereas only a minority of data have lower Zr and fall into the I-/S-type field. In the Nb–Y diagram (Pearce et al. 1984), the data fall into the fields of within-plate granites (WPG), volcanic arc granites and syn-collisional granites (VAG+syn-COLG; Fig. 3.8b). In the same plot, the data are scattered between the fields of A2-type, slab-failure and arc settings (Whalen & Hildebrand 2019). Notably, most of the population has Y/Nb greater than 1.2 or even up to 4. Within the same suite, the data extend from WPG into VAG (e.g. Varin).

3.3.2.2. Primitive mantle-normalised diagrams

Normalising granite trace elements to the primitive mantle (PM) highlights enrichment or depletion patterns relative to the original composition of the bulk silicate Earth, which would facilitate identifying magmatic processes such as partial melting, fractionation and crustal contamination (Sun & McDonough 1989). The PM-normalised rare earth element (REE) and extended trace-element diagrams show the composite trace element patterns in granitoids by regions (Figs. 3.9 & 3.10; Sun & McDonough 1989). In the REE diagrams (*left column* of Figs. 3.9 & 3.10), the granitoids are generally enriched in light-REE (LREE) compared to heavy-REE (HREE). Eu anomalies (Eu/Eu*) are variable. The wide range of REE values indicates varying degrees of fractionation within each plutonic suite. Moreover, the PM-normalised trace-element diagrams (*right column* of Figs. 3.9 & 3.10) illustrate that the granitoids have variable enrichment or depletion in large-ion lithophile elements (LILE, e.g. Rb, Sr, Ba, Pb). The high field strength elements (HFSE) display pronounced negative Nb, Ta, Sr, P, and Ti anomalies. These trace-element variations are described below.

*Eu/Eu**** in the granitoids is variable across the study area, and two major trends are notable (Fig. 3.11). The first trend is defined by granitoids with a variably positive Eu anomaly independent of silica evolution, including Chicoutimi, Pipmuacan, Miquelon (syenite), and some

data from Péribonka, Sabot and Okaopéo granitoids. The second trend represents granitoids with Eu fractionation, which have decreasing Eu/Eu* with increasing silica content, for instance, Varin and La Baie.

LILE substitute into major minerals. Rb and Ba replace K in feldspars, biotite and amphibole, while Sr exchanges with Ca in pyroxene and plagioclase. It is noted that LILE are fluid-mobile and may be subjected to subsolidus alteration (Keppler 2017). The steeper trend with a high K/Rb ratio shows the presence of feldspar and biotite taking up Rb (Fig. 3.11b). A gentler trend reflects Rb incompatibility. Granitoids in the low-*P* segments have a large range in Rb (~50–300 ppm) concentration and low K/Rb (~200–400), suggesting that Rb is a more incompatible element in these magmas. In contrast, rocks in the mid-*P* segment, LSJ and Saguenay regions have low Rb (<150 ppm) and a large range of K/Rb (~200–1000).

Ba and Sr contents vary in the granitoids, but they correlate overall (Fig. 3.11c). The mean Ba is high at 1716 ppm, with some high-Ba granitoids containing up to 6185 ppm Ba. Sr is less abundant at a range of 5–1443 ppm. The two elements are correlated in most of the suites, except for Pipmuacan and Péribonka, where dispersion is observed.

Pb displays a spatial trend, distinguishing granitoids into low-Pb (<8 ppm) and high-Pb (8–61 ppm) groups (Figs. 3.11 & 3.12). The low-Pb group mainly includes the granitoids in the low-*P* segment in the Baie-Comeau region and those associated with the Vanel anorthosite, west of Lac-St-Jean, and is distributed in an E-W direction. The high-Pb group is geographically distributed north and south of the low-Pb group and includes the granitoids in the mid-*P* segment, those in the low-*P* ESB, and those in Saguenay and Valin. There are, however, a few exceptions; for instance, some data from Manic 5 are low-Pb, while some from Varin are high-Pb, and the Astra granite (Fig. 3.12), which intruded a supracrustal sequence, is a high-Pb pluton.

HFSE displays negative anomalies and primitive to enrich HFSE ratios. Preliminary screening of PM-normalised trace element diagrams revealed pronounced Nb, Ta and Ti anomalies, and Zr is enriched (Figs. 3.13). On the Nb/Ta *vs.* Zr/Hf diagram, the granitoid compositions cluster near or above these chondritic ratios ($[Nb/Ta]_n$ ~17.6, $[Zr/Hf]_n$ ~37.1; Fig. 3.13a). Some granitoids are more enriched in Zr or Nb, such as the Nb-enriched Chicoutimi Mangerite (Nb/Ta ~54–62). The Zr/Hf ranges from ~30 up to 67, with a superchondritic cluster.

Zr enrichment is evident by the abundant zircon in the rocks. Overall, the Nb/Ta–Zr/Hf relationships show that the granitoids are either unfractionated or relatively enriched in Zr or Nb in terms of HFSE.

3.3.2.3. Zircon Saturation Temperature

The granitoids have high zircon saturation temperatures (T_{Zr}, Fig. 3.13b) in the model of Watson and Harrison (1983). Overall, Zr contents range from ~40 to 2070 ppm, and the compositional parameter (M) ranges from 0.62 to 1.51. Following Watson and Harrison (1983), only the samples with an M-value between 0.9 and 1.7, i.e. within the calibrated compositional interval, are described. After filtering, most granitoids cluster between M = ~0.9–1.2 with Zr ~200 – 2000 ppm Zr, reaching zircon saturation at T_{Zr} from ~850 up to 1100ºC for both time periods. A small portion of samples have scattered M values and T_{Zr} lower than 850ºC.

3.4. Discussion

3.4.1. Insights from geochronology

Intermediate to felsic plutonic rocks were emplaced intermittently between ca. 1086–1007 Ma in the central Grenville Province. The culmination of the Ottawan phase is marked by the emplacement of the most voluminous plutons at ca. 1082–1057 Ma (Fig. 3.14), for instance, Varin Plutonic Suite, which is locally rimmed by a mafic unit of similar age (Louis Plutonic Suite), and Rivière-à-Pierre Plutonic Suite. These units are exposed in the low-*P* segment, from Baie-Comeau to the SFDZ and are spatially associated with large and older, ca. 1160 to 1140 Ma anorthosites. In early Ottawan, granitoid plutons (e.g. Strike, Pamouscachiou) intruded the LSJ and Vanel Anorthosites (~1080 Ma; van Breemen 2009) between SFDZ and PDZ, as well as St. Urbain Anorthosite (~1060–1045 Ma; Morisset et al. 2009) to the south of SFDZ. Elsewhere, early Ottawan plutons are sporadically exposed in both the mid-*P* segment (Manic 5) and the low-*P* ESB (Bon-Desir Granite and Michaud Monzonite).

In the low-*P* segment, smaller intrusions (Miquelon in the Baie-Comeau region, felsic sill in ESB) followed at ca. 1048–1045 Ma. No magmatic record between ca. 1042 and 1032 Ma indicates a potential hiatus in magmatism during that interval. The majority of younger granitoid plutons (~1032–1010 Ma) are exposed in the mid-*P* segment and the Lac-St-Jean region. These

are smaller (~1–100 km^2) intrusions, commonly located along major crustal-scale shear zones (e.g. SFDZ; Fig. 3.14). Finally, the only young granitoid unit reported in the low-*P* segments is Varin Unit 2, dated at ca. 1007 Ma. This is ~50 Myr younger than the age of Varin Unit 1; whether the Varin Plutonic Suite was generated over a prolonged period or by multiple pulses remained elusive.

The regional distribution of plutons and U–Pb ages (Fig. 3.14) suggests an overall trend defined by:

(a) older, early to mid-Ottawan granitoids in the low-*P* segments (Baie-Comeau / Parc des Laurentides and ESB),
(b) younger late Ottawan / transitional to Rigolet in the mid-*P* segment, and;
(c) both older and younger granitoids in the LSJ region (and younger ages along the SFDZ).

However, there are some exceptions, as the mid-Ottawan Manic 5 Suite is in the mid-*P* segment, and the youngest, Varin Unit 2, is in the low-*P* segment. Despite the age gap between ~1042 and 1032 Ma suggested by the data, older and younger granitoids share similar geochemical patterns, implying potentially similar modes of magmatism before and after the 10-Myr hiatus.

3.4.2. Petrogenetic implications from geochemistry

In the granitoids of central Grenville, two main trends are identified based on major elements: an alkaline monzonite–syenite trend mainly in those of the LSJ region, and a subalkaline monzogranite–granite trend mainly in those of the mid- and low-*P* segments. A large majority of data from the older granitoids shows zircon saturation temperatures between 850 and 950ºC, while the data from the younger granitoids show a wider spread, between 850ºC and 1050ºC. In both cases, the zircon saturation temperatures are consistent with the starting inference that these are high-*T* granitoids.

Under the descriptive classification (Frost et al. 2001a), the granitoids are dominantly ferroan, metaluminous and alkalic to alkali-calcic. The ferroan characteristics are consistent with an origin from the fractionation of a reduced basaltic source. However, they generally exhibit high MALI and are predominantly alkaline to alkali-calcic, with an alkaline cluster observed in the intermediate granitoids, and the alkali-calcic to calc-alkalic trend indicates crustal

assimilation. Additionally, the granitoids are metaluminous to weakly peraluminous, characterised by the presence of biotite and/or hornblende (and in some cases orthopyroxene) in the igneous mineral assemblage and a lack of garnet and muscovite. This aligns with the lack of S-type character and suggests that they were not formed from the melting of thickened and heated orogenic crust containing recycled metasedimentary rocks.

In the tectonic discrimination diagrams, the granitoids fall into the WPG field, with some units extending into the VAG field. This trend, together with the pronounced negative Nb–Ta–Ti anomalies, suggests a situation in which within-plate magmas assimilated earlier arc crust, leading to the inheritance of an arc signature. This will be tested by isotopes (Chapter 4) and assuming the parental magma derives from the mantle, considering that the granitoid magmas are intrusive into the Quebecia crust, which was part of a Pinwarian-age arc system at the margin of Laurentia.

The orogenic high-*T* granitoids have some A-type granite characteristics, such as elevated Zr concentrations and a tendency to fall into the WPG field; however, they do not entirely resemble granitoids formed in post-collisional or anorogenic tectonic settings. The pattern of the high-T granitoids in the Nb–Y diagram is akin to post-collisional granites, which have a mixed signature of both mantle and crust. However, the post-collisional tectonic setting conflicts with the protracted synchronous metamorphism during the ~80 Myr emplacement period of granitoids. Furthermore, post-orogenic granite data used in the model of Whalen and Hildebrand (2019) are modern magnesian, calc-alkalic to calcic granitoids. The trace element geochemistry of magnesian granitoids could differ from that of Proterozoic ferroan granitoids (Frost et al. 2001a; Frost & Frost 2011).

Collectively, no major change in the geochemistry before and after the magmatic hiatus indicates a broadly common petrogenesis in the central Grenville Province throughout the Grenvillian Orogeny. Moreover, the Quebecia arc crust is an important component in the petrogenesis of the orogenic high-*T* granitoids. This Chapter sets the basis for studying the petrology, age and geochemistry of the granitoids in Chapter 4.

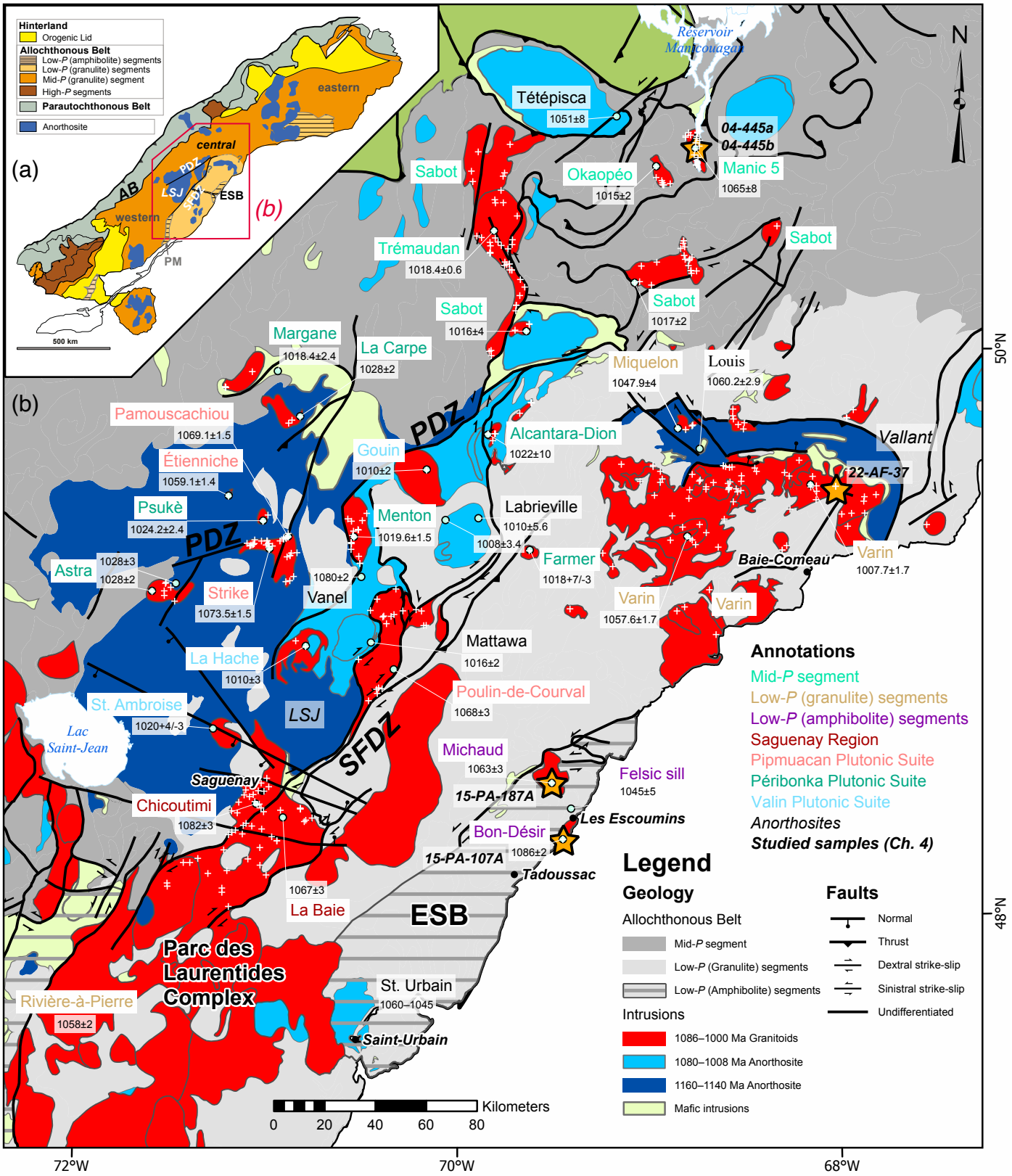

Figure 3.1 (a) Geology overview of the Grenville Province, modified after Rivers et al. (2012) and Indares (2020). Abbreviations: AB – Allochthonous Boundary; ESB – Escoumins Supracrustal Belt; PM – Portneuf-St-Maurice Domain; LSJ – Lac-St-Jean Anorthosite; PDZ – Pipmuacan Deformation Zone; SFDZ – Saint Fulgence Deformation Zone. **(b)** Spatial distribution of syn-orogenic magmatism in the central Grenville Province, modified from the MRNF SIGÉOM database (MRNF 2021). Zircon U–Pb ages are reported with uncertainties at 2σ (reference in Table 3.1). White cross – Geochemistry sample location; and orange star – location of samples discussed in Chapter 4.

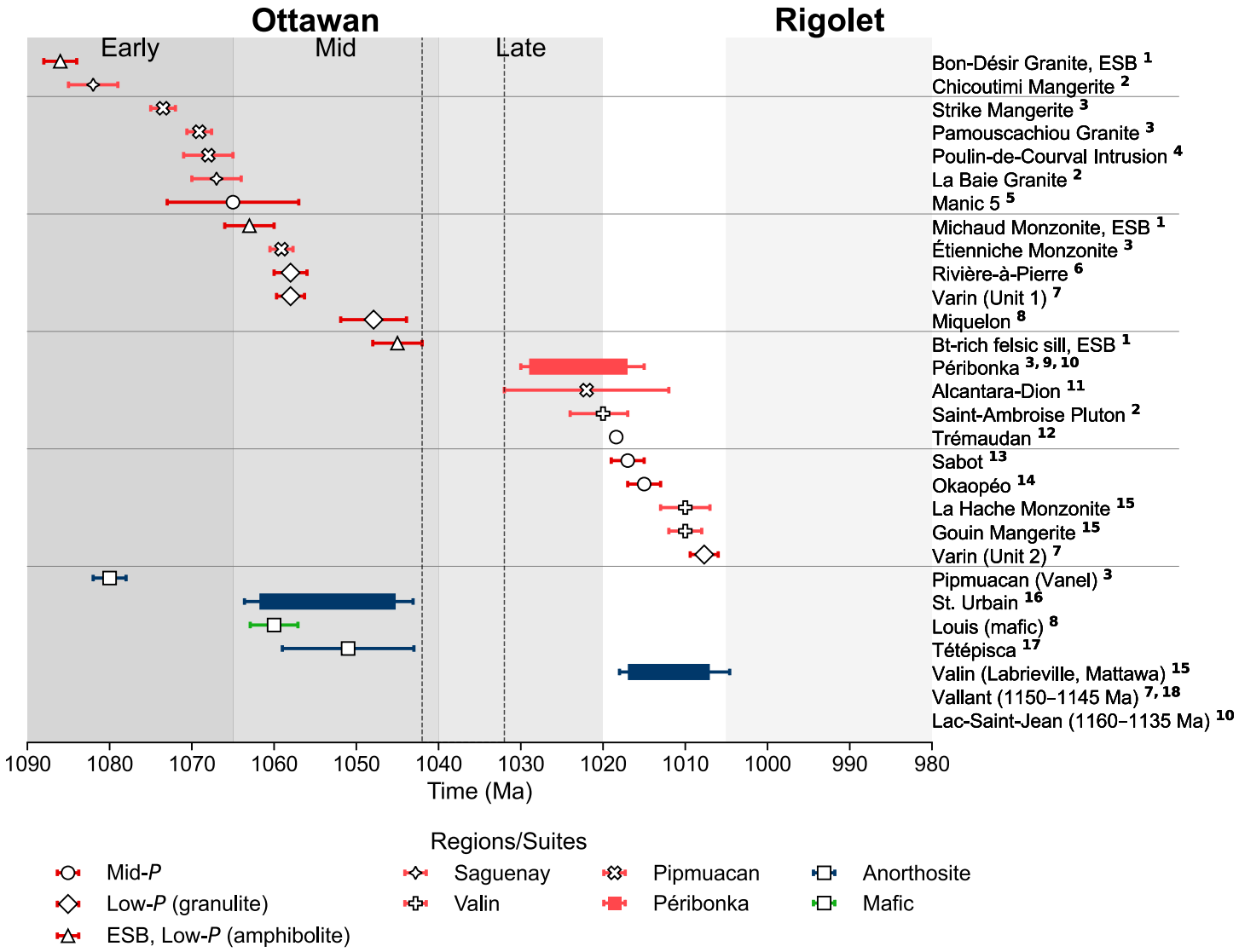

Figure 3.2 Compilation of the zircon U–Pb ages of plutonic suites/units in the central Grenville Province between 1100 and 1000 Ma, showing the timing of intrusions in ascending order. Error bars represent uncertainties at 2σ; if none, errors are less than symbol size. A gap between 1040–1030 Ma is apparent (dotted interval). The orogenic periods are indicated as coloured boxes. The anorthosites and their associated mafic suites are shown in blue. In the study region, Lac-St-Jean (1160–1135 Ma)[10] and Vallant Anorthosite Suite (1150–1145 Ma)[8] are out of the time range. Péribonka Plutonic Suite (1028–1018 Ma)[10] includes Astra Granite (1028 ± 2 Ma)[9], La Carpe Granite (1028 ± 2 Ma)[3], Psukè Granite (1024.2 ± 2.4 Ma)[3], Menton Granite (1019.6 ± 1.5 Ma)[3], Margane Monzonite (1018.4 ± 2.4 Ma)[3], and Farmer Monzonite (1018+7/-3 Ma)[18]. Valin AMCG Suite (1020–1008 Ma) includes Mattawa (1016 ± 3 Ma)[15] and Labrieville Anorthosite Suite (1010–1008 Ma)[15], Saint-Ambroise Intrusion (1020+4/-3 Ma)[2], Gouin Mangerite (1010 ± 2 Ma)[15] and La Hache Monzonite (1010 ± 3 Ma)[15]. Varin Plutonic Suite includes two dated plutonic units: Unit 1 granite/monzonite and Unit 2 orthopyroxene-bearing granite/monzonite (see text).

Reference: **1** – Groulier et al. (2018); **2** – Higgins and van Breemen (1996); **3** – van Breemen (2009); **4** – Hébert et al. (1998c); **5** – Dunning and Indares (2010); **6** – Moukhsil and Côté (2018); **7** – David et al. (2009); **8** – David et al. (2010b); **9** – Higgins et al. (2002); **10** – Hébert et al. (2009); **11** – David et al. (2010a); **12** – Davis et al. (2014); **13** – Gobeil et al. (2002); **14** – Augland et al. (2015); **15** – Hébert et al. (2005); **16** – Morisset et al. (2009); **17** – Moukhsil et al. (2013b); **18** – Emslie and Hunt (1990).

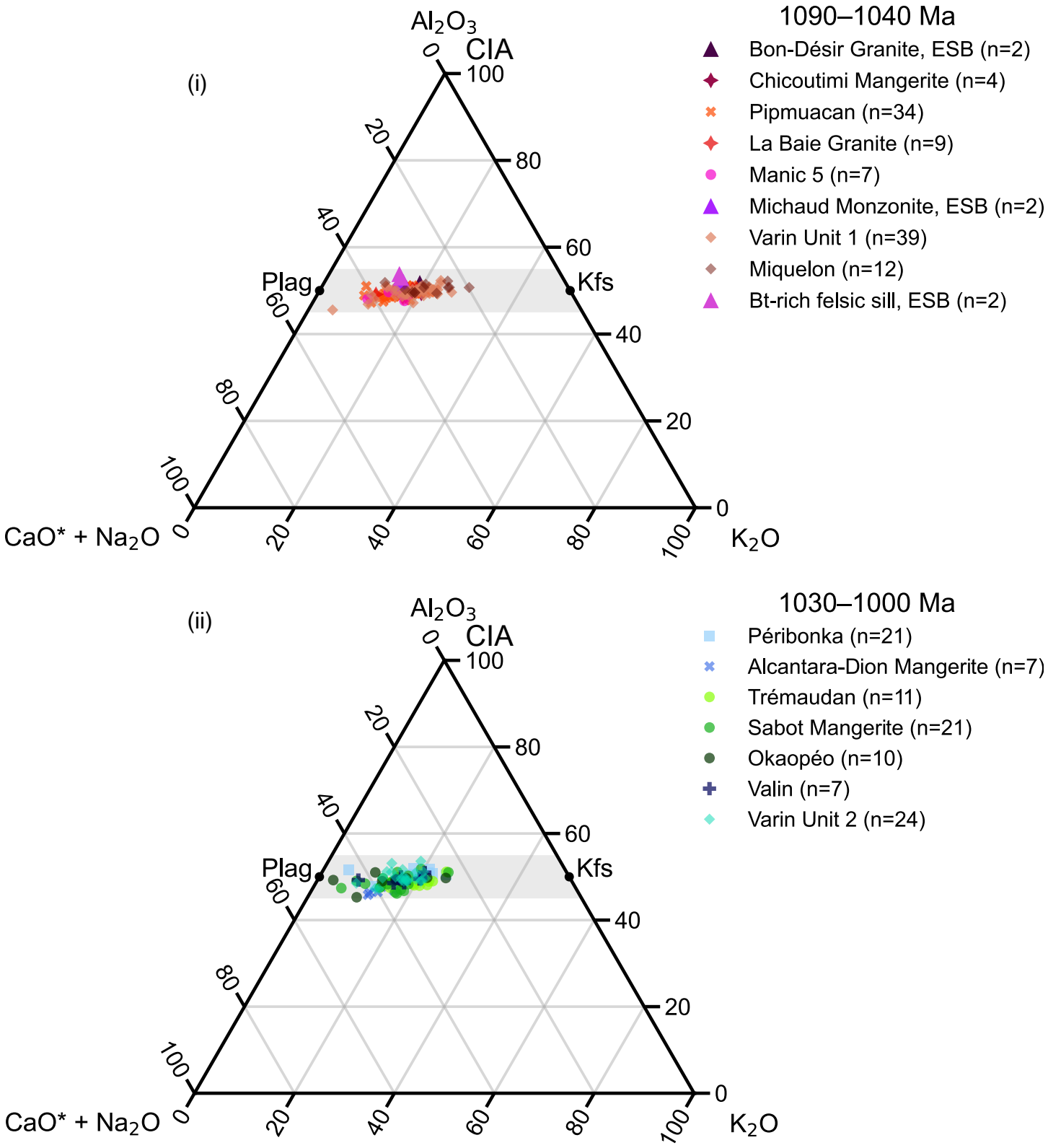

Figure 3.3 A–CN–K diagram for monitoring post-crystallisation alteration (Nesbitt & Young 1982). The chemical index of alteration (CIA) is represented by the proportion of Al_2O_3. Plagioclase (Plag) and K-feldspar (Kfs) are labelled. The shaded region is the average range of unaltered granites (CIA between 45 and 55). Two sets of plots are plotted for plutonic suites/units with their age of intrusion during **(i)** ca.1090–1040 Ma and **(ii)** ca. 1030–1000 Ma, before and after the age gap, respectively.

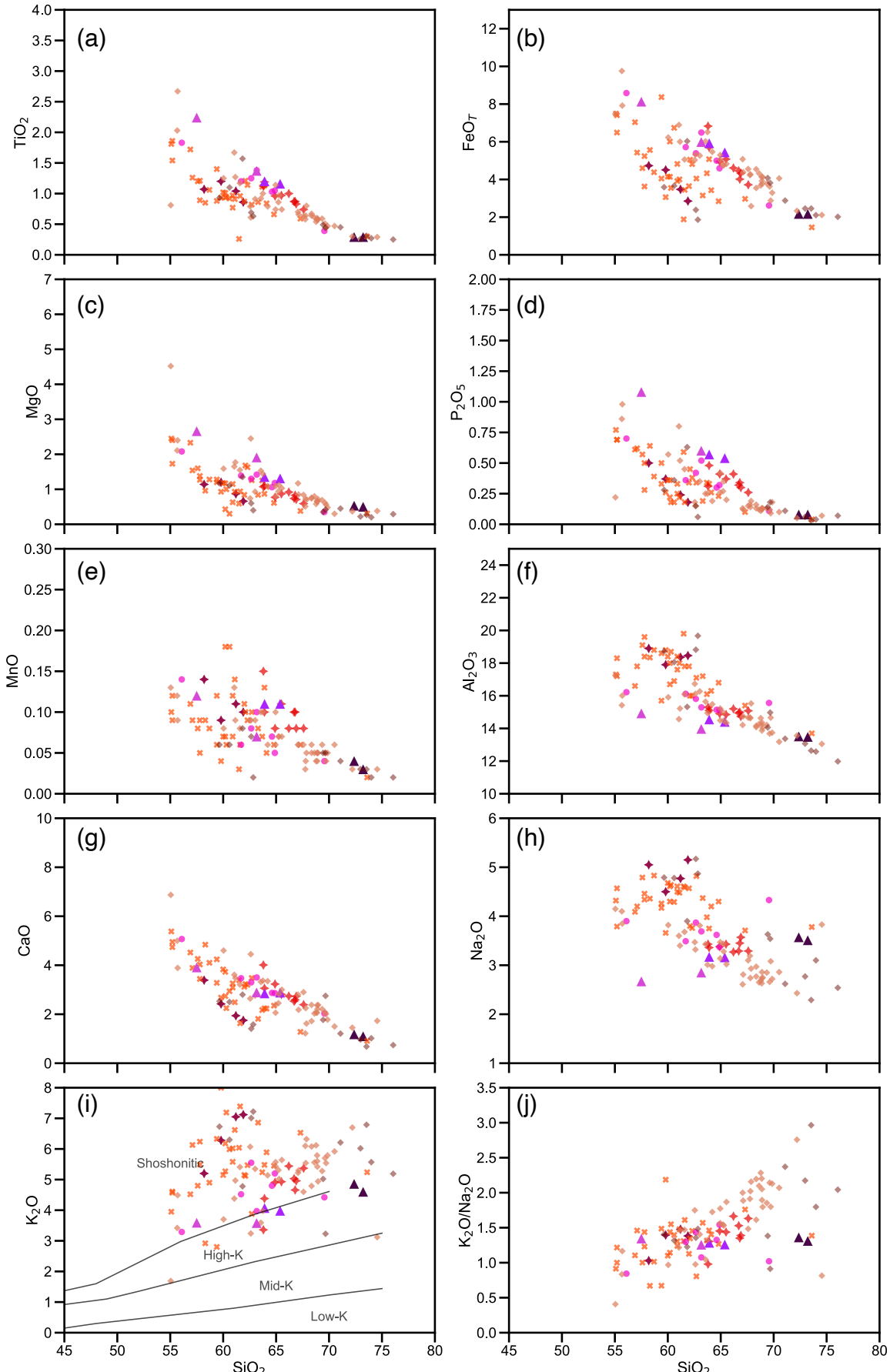

Figure 3.4 Major elements–silica diagram of ca.1090–1040 Ma high-*T* granitoids. **(a)** TiO_2, **(b)** FeO_T, **(c)** MgO, **(d)** P_2O_5, **(e)** MnO, **(f)** Al_2O_3, **(g)** CaO, **(h)** Na_2O, **(i)** K_2O (Peccerillo & Taylor 1976), **(j)** K_2O/Na_2O–SiO_2. Legend refers to **Fig. 3.3**.

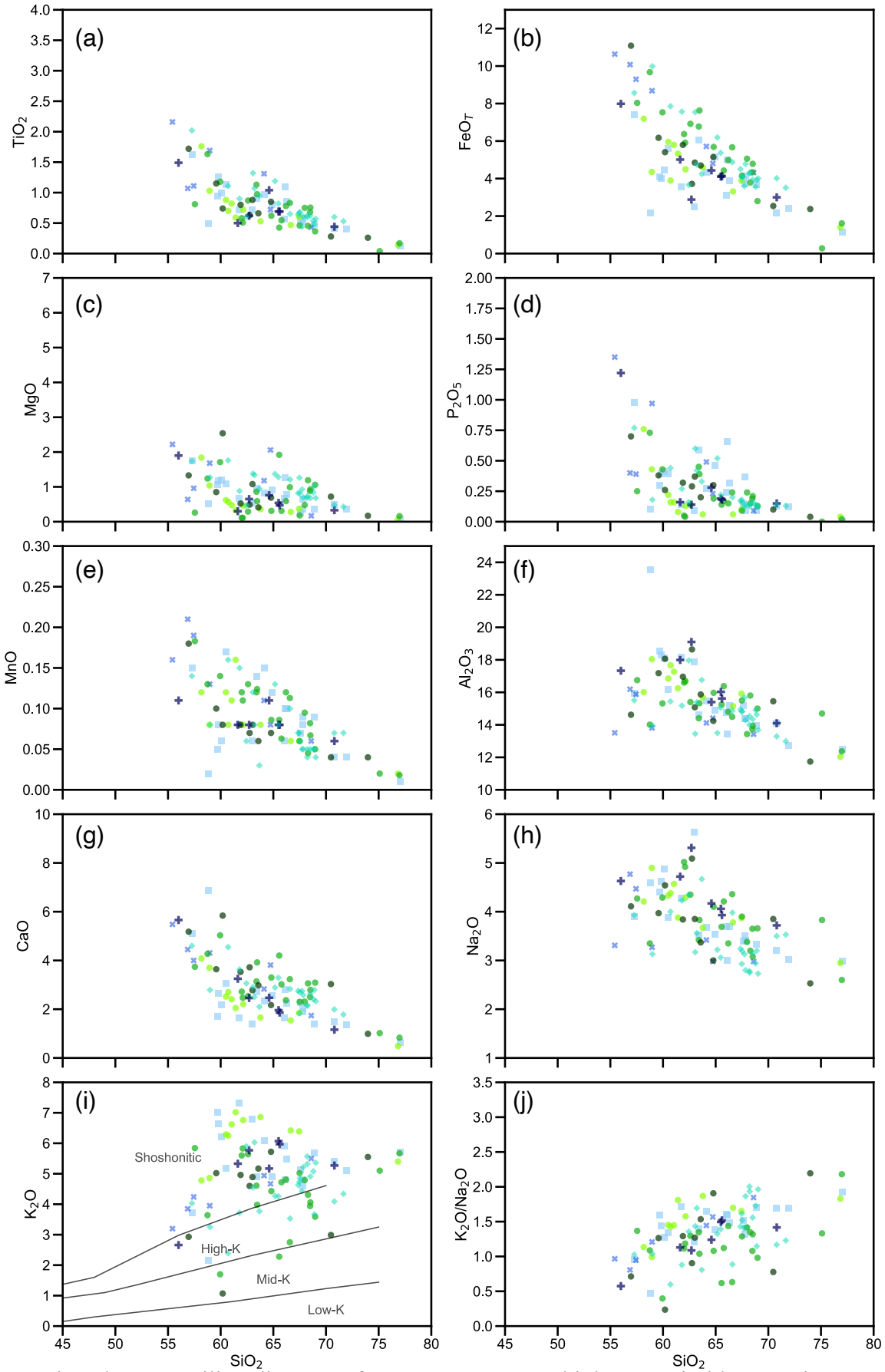

Figure 3.5 Major elements–silica diagram of ca.1030–1000 Ma high-*T* granitoids. **(a)** TiO_2, **(b)** FeO_T, **(c)** MgO, **(d)** P_2O_5, **(e)** MnO, **(f)** Al_2O_3, **(g)** CaO, **(h)** Na_2O, **(i)** K_2O (Peccerillo & Taylor 1976), **(j)** K_2O/Na_2O–SiO_2. Legend refers to **Fig. 3.3**.

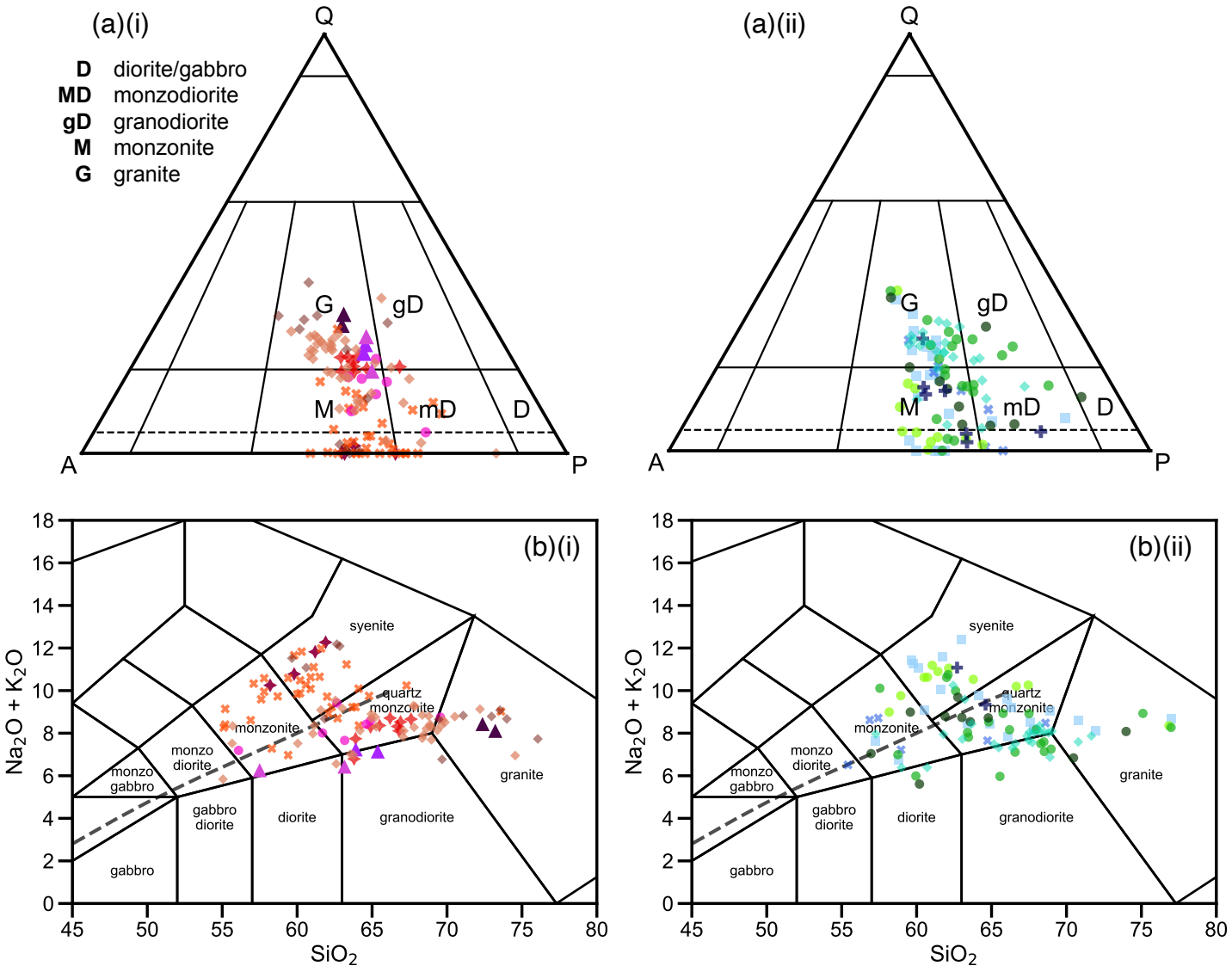

Figure 3.6 Granitoid classification. **(a)** QAP (Streckeisen 1976) and **(b)** TAS diagram (Middlemost 1994) for granite classification. The general distinction between alkaline and subalkaline compositions is shown in grey dashed lines (Irvine & Baragar 1971). For intrusion ages and legend, refer to **Fig. 3.3**.

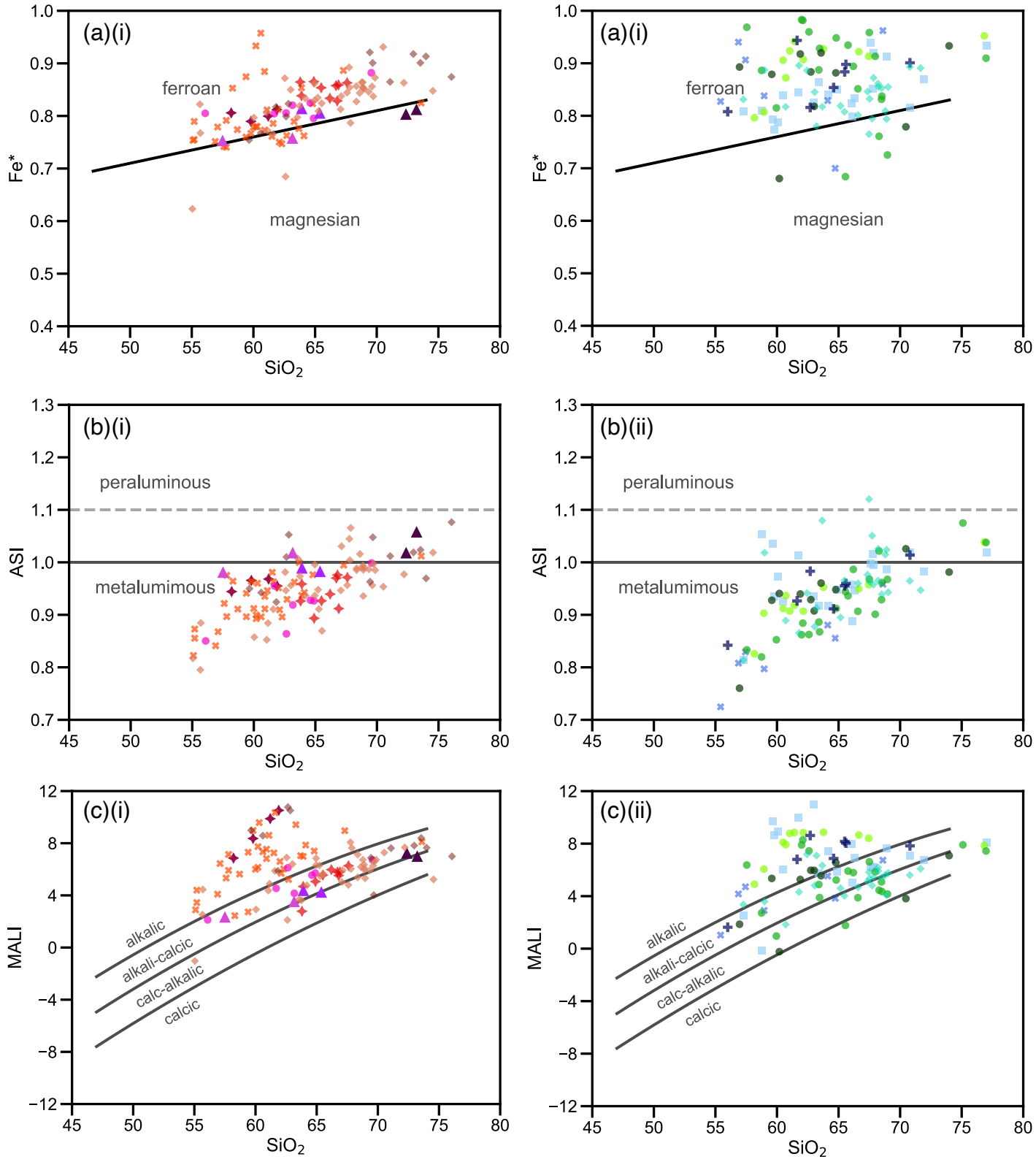

Figure 3.7 Granite descriptive classification based on major elements (Frost et al. 2001a). **(a)** Fe number Fe* = $FeO_T/(FeO_T + MgO)$, **(b)** Aluminous saturation index ASI = Al/(Ca − 1.67P + Na + K), and **(c)** Modified alkali-lime index MALI = $Na_2O + K_2O - CaO$. For intrusion ages and legend, refer to **Fig. 3.3**.

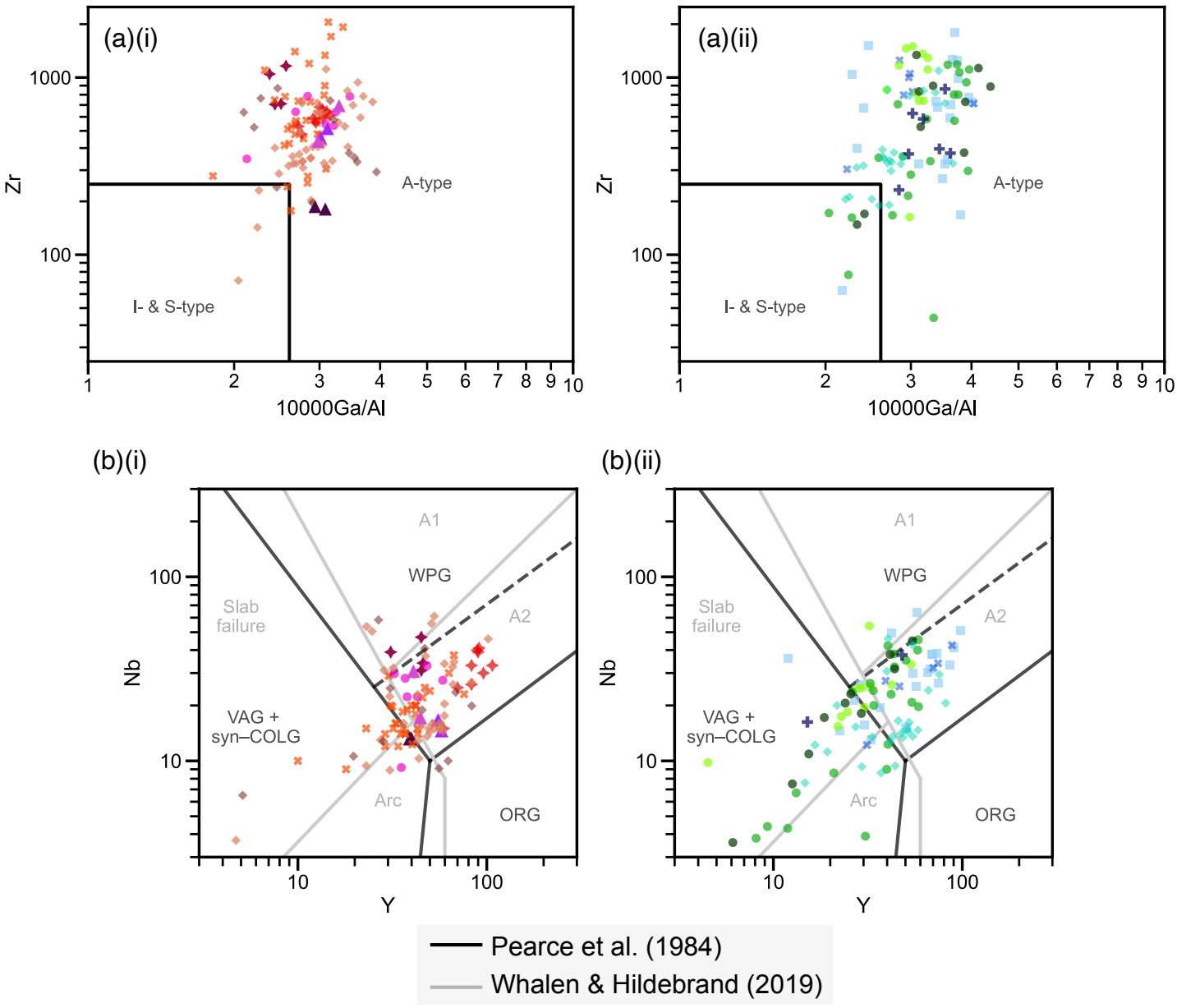

Figure 3.8 Tectonic discrimination diagrams based on trace elements. **(a)** Zr–Ga/Al (Whalen et al. 1987), and **(b)** Nb–Y (Pearce et al. 1984; Whalen & Hildebrand 2019). For intrusion ages and legend, refer to **Fig. 3.3**.

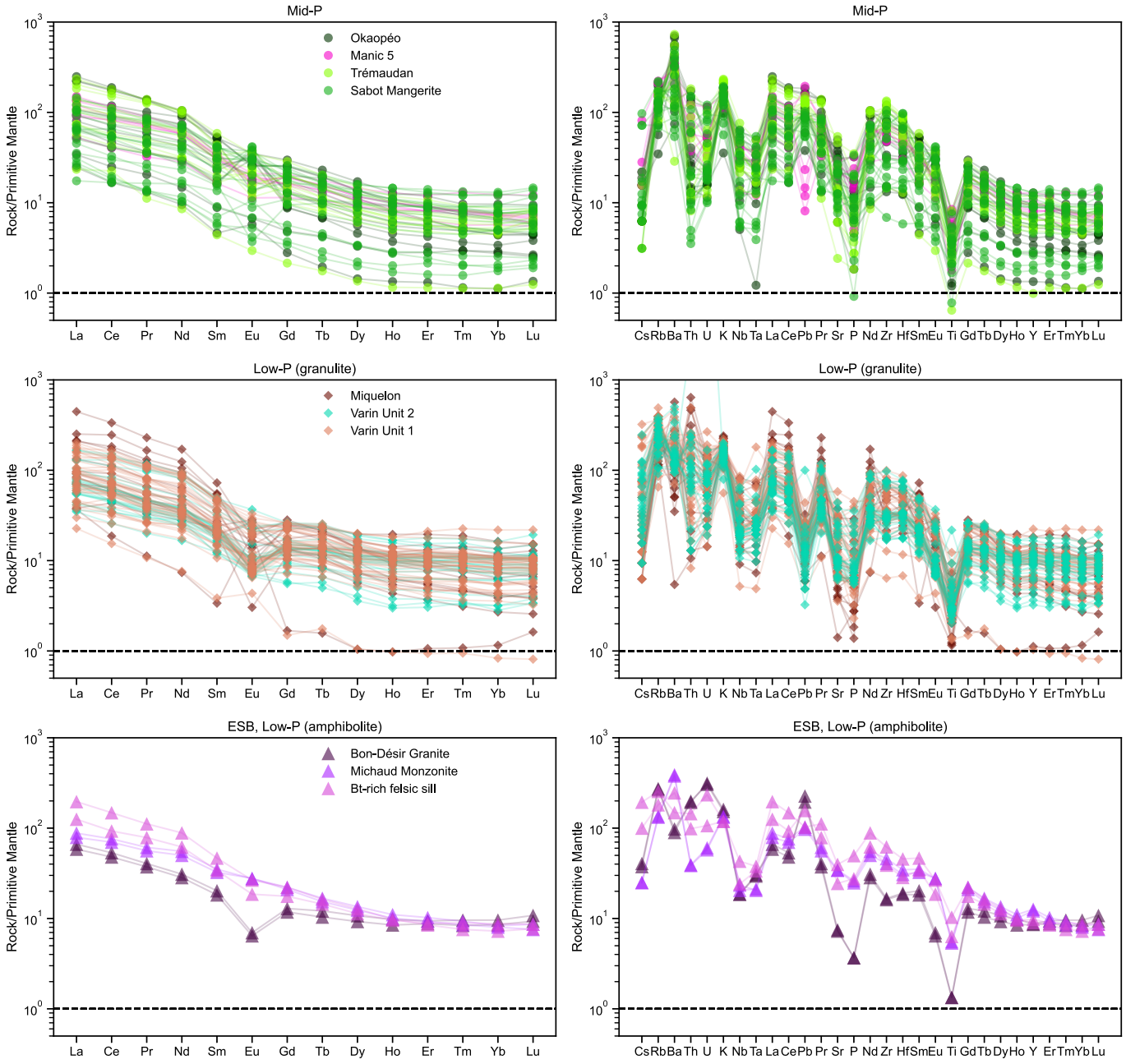

Figure 3.9 Primitive mantle-normalised (Sun & McDonough 1989) REE (*left column*) and extended trace element diagrams (*right*) of mid- and low-P (granulite) segments and ESB.

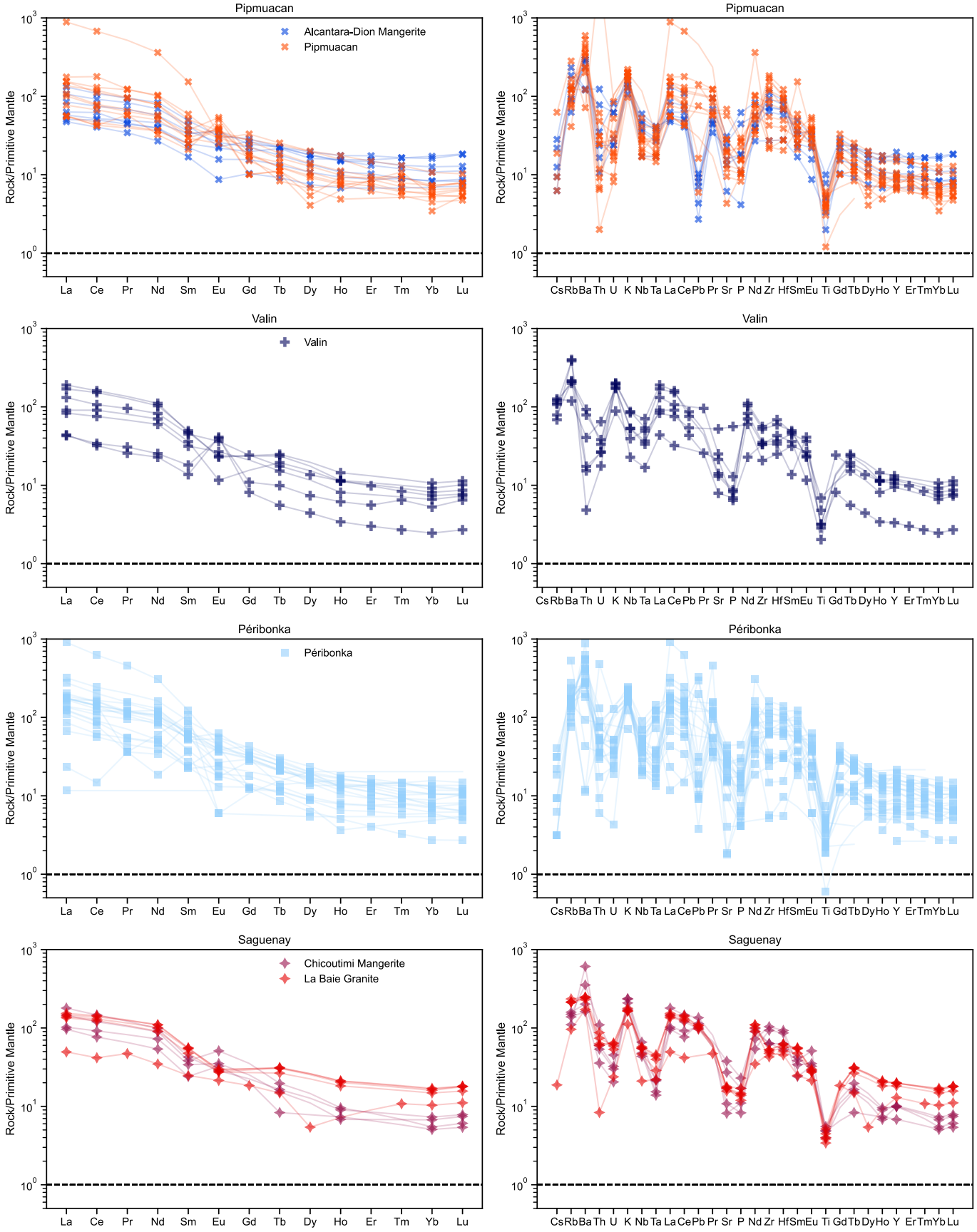

Figure 3.10 Primitive mantle-normalised (Sun & McDonough 1989) REE (*left column*) and extended trace element diagrams (*right*) of Pipmuacan, Valin, Péribonka suites and granitoids in the Saguenay region.

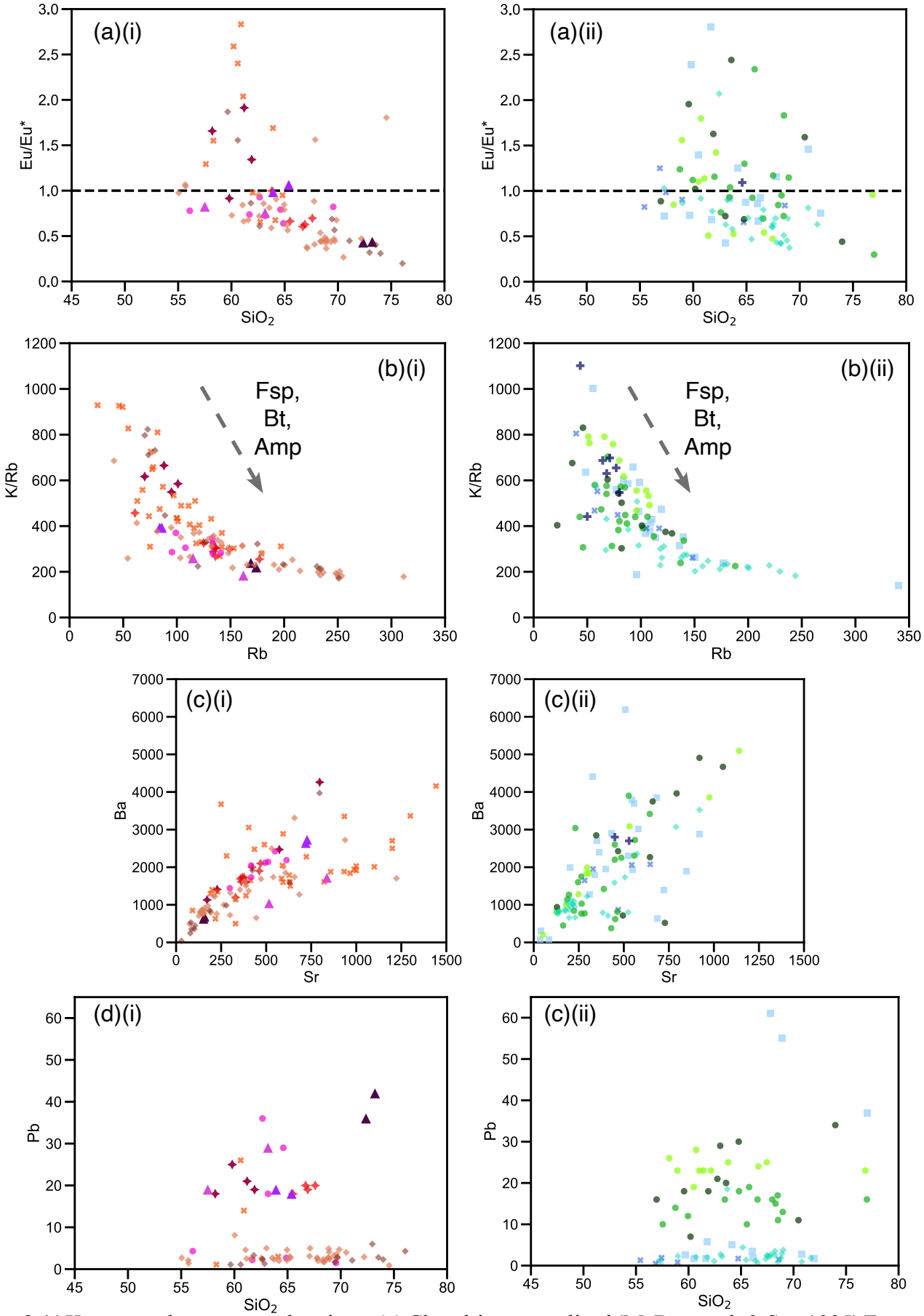

Figure 3.11 Key trace elements geochemistry. **(a)** Chondrite-normalised (McDonough & Sun 1995) Eu anomaly Eu/Eu*–SiO_2. **(b)** K/Rb–Rb, fractionation of Rb and K. **(c)** Ba–Sr and **(d)** Pb–SiO_2 diagrams, showing LILE trends. For intrusion ages and legend, refer to **Fig. 3.3**.

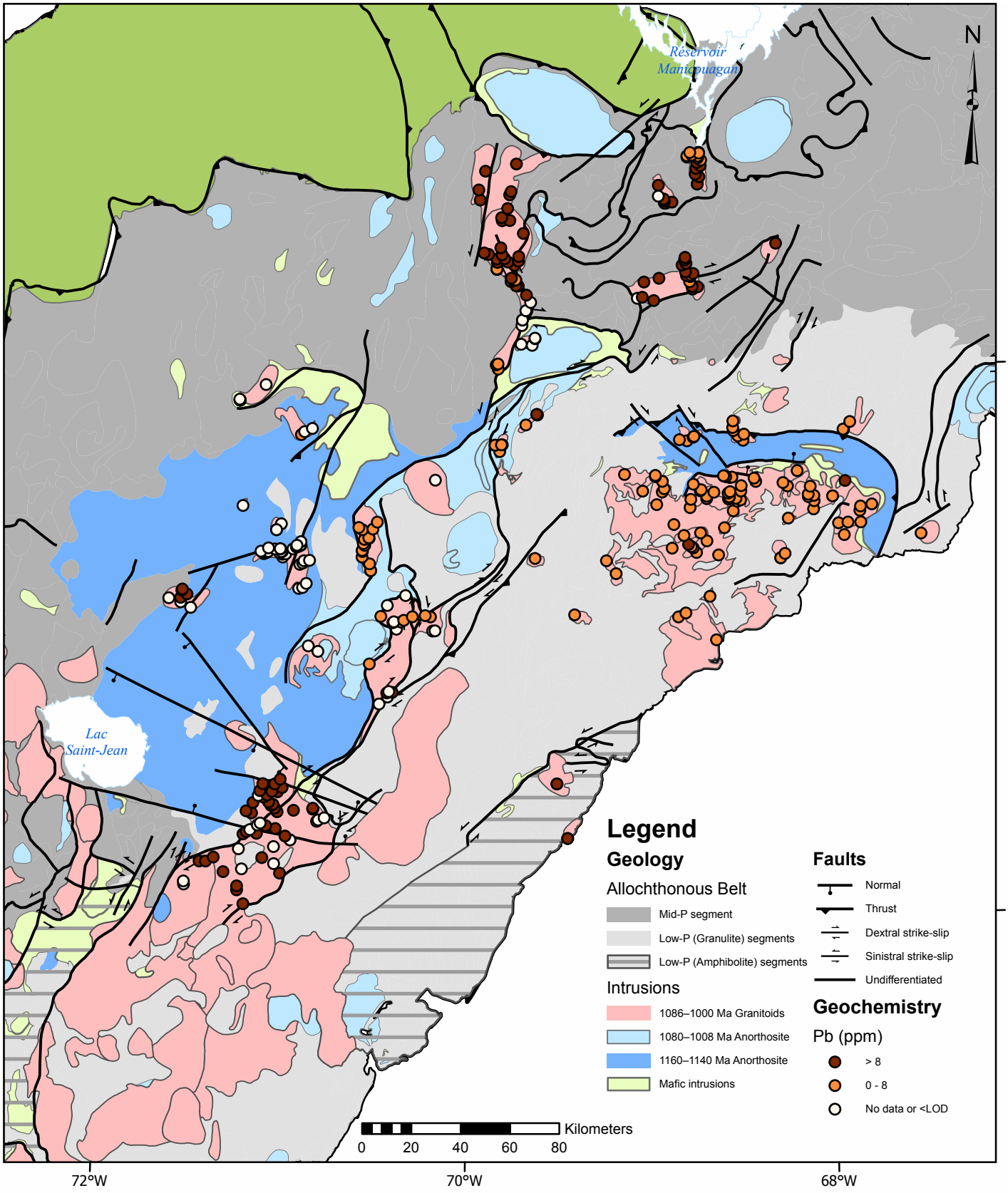

Figure 3.12 Distribution of Pb (ppm) in high-*T* granitoids in the study region. Data lower than limit of detection (LOD) are discarded.

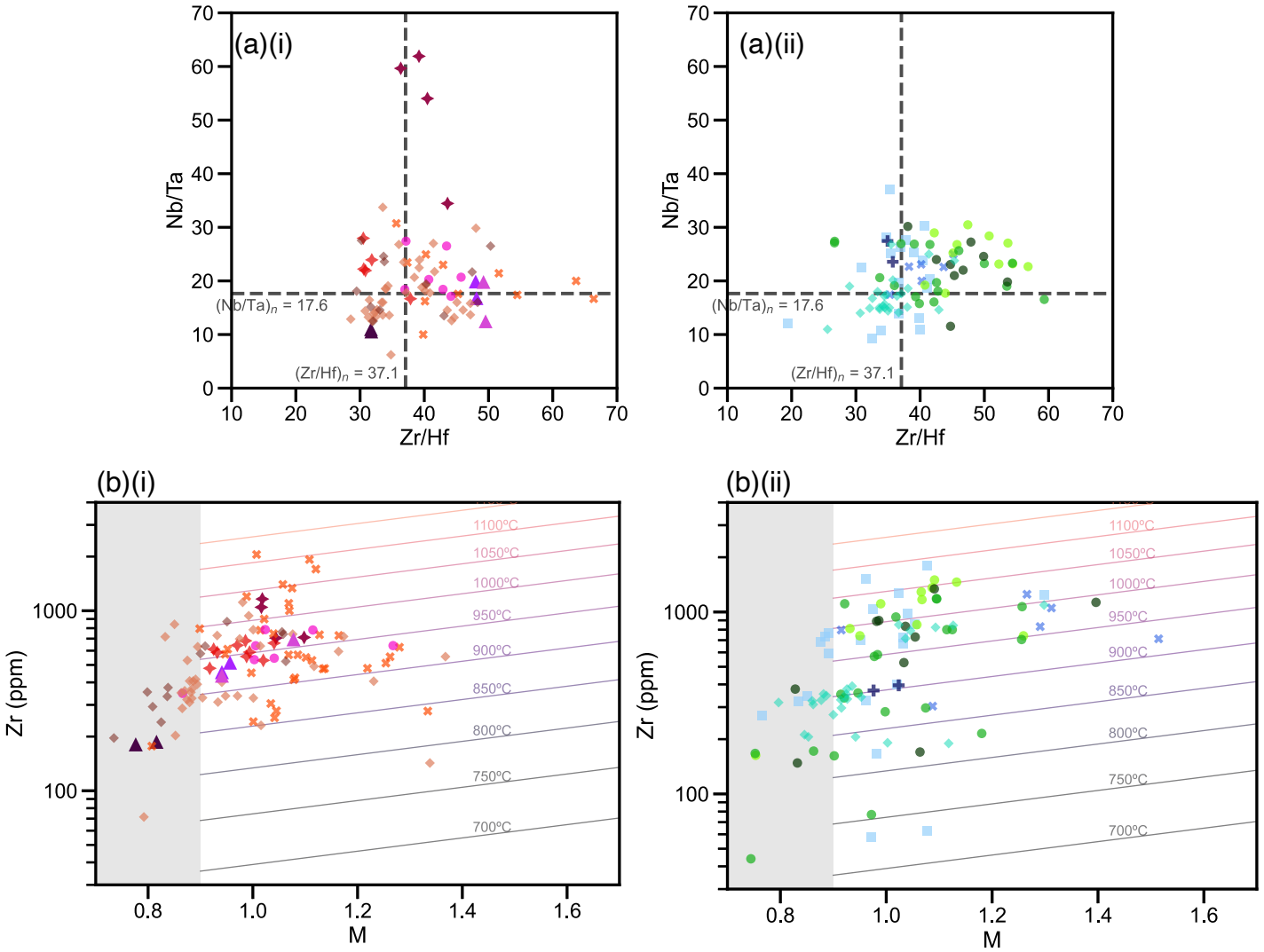

Figure 3.13 Key trace elements geochemistry continued. **(a)** Nb/Ta–Zr/Hf, with the chondritic ratios (black dashed lines, McDonough & Sun 1995). **(b)** Zircon saturation temperature (T_{Zr}, Watson & Harrison 1983). The data falling into the uncalibrated region (shaded) are considered invalid. For intrusion ages and legend, refer to **Fig. 3.3**.

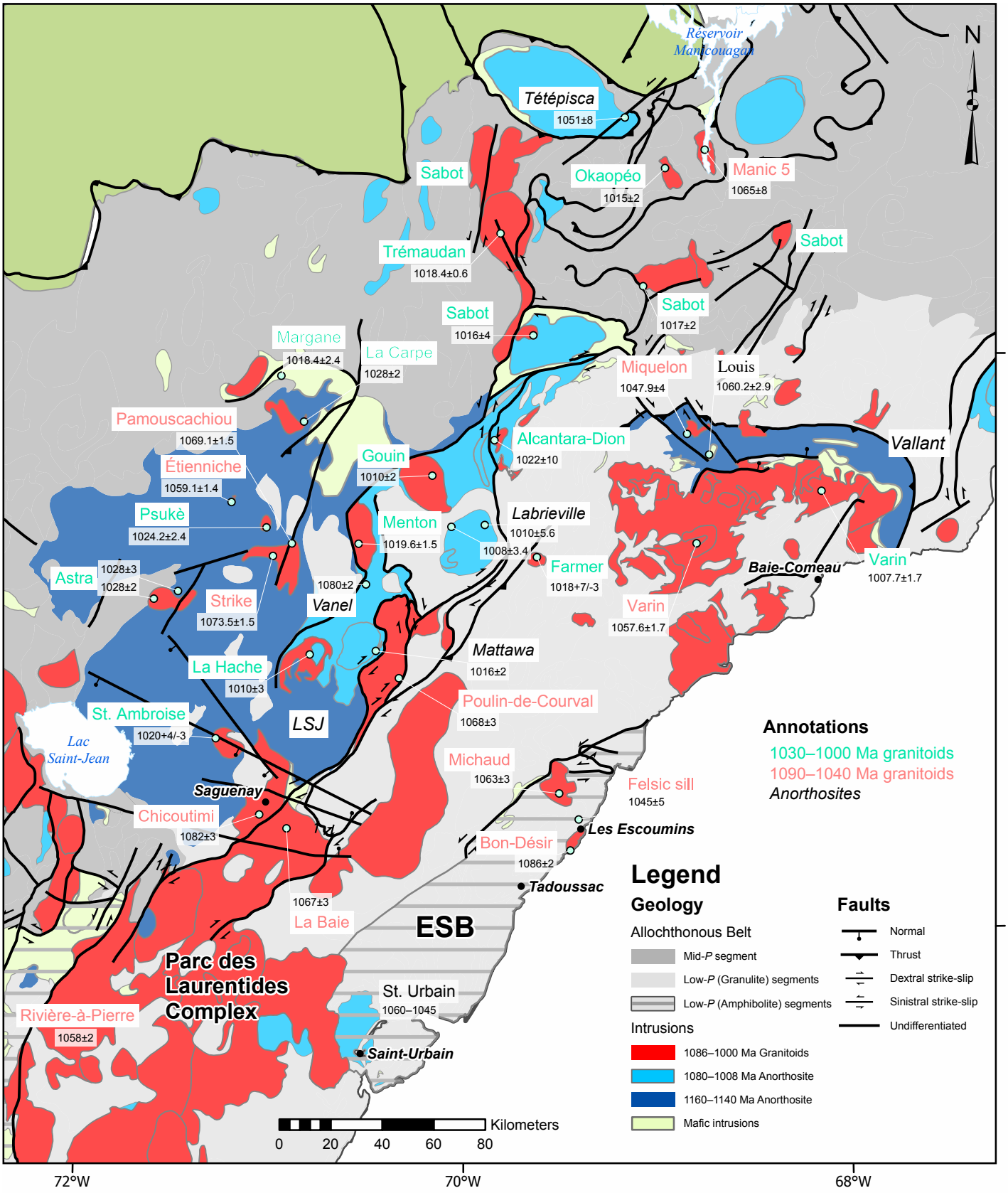

Figure 3.14 Spatial distribution of syn-orogenic magmatism in the central Grenville Province with colour-coded annotation showing 1030–1000 and 1090–1040 Ma granitoids, modified from the MRNF SIGÉOM database (MRNF 2021). Zircon U–Pb ages are reported with uncertainties at 2σ (reference in Table 3.1). White cross – Geochemistry sample location; and orange star – location of samples discussed in Chapter 4.

Chapter 4. In-depth characterisation of orogenic high-*T* granitoids

This chapter focuses on samples from five granitoid plutons exposed in different crustal levels in the Manicouagan–Escoumins/Baie Comeau area (Central Grenville Province). From north to south, these are Manic 5 Plutonic Suite (04-445a, 04-445b) in the mid-*P* segment; Varin Plutonic Suite (22-AF-37) in the granulite-facies portion of the low-*P* segment (Baie Comeau area); and Michaud Monzonite (15-PA-187A) and Bon-Désir Granite (15-PA-107A) in the amphibolite-facies, low-*P* Escoumins Supracrustal Belt (ESB). The locations of the samples are shown in Fig. 3.1). Numbers in parentheses refer to the investigated samples. The chapter first summarises the general characteristics, as well as the petrography and mineral chemistry of the investigated samples from each pluton. Next, the results of thermobarometry, whole-rock major, trace and Sm–Nd isotope geochemistry are presented, followed by extensive characterisation of zircon in terms of geochemistry, Lu–Hf isotopic signatures and U–Pb ages.

4.1. General characteristics, petrography and mineral chemistry

This section documents key characteristics at the outcrop and at the sample scale for each pluton. Outcrop photographs are shown in Figure 4.1. For each sample, mineral modes estimated by SEM–MLA are listed in Table 4.1. Associated false colour mineral maps are shown in Figure 4.2, and photomicrographs in Figure 4.3. Mineral chemistry data is presented in Figure 4.4, Tables 4.2 and 4.3, and Appendix B.

Table 4.1 Mineral modes (area %) of the granitoid samples examined in this study.

Unit	04-445a	04-445b	22-AF-37	15-PA-187A	15-PA-107A
	Manic 5 monzonite	Manic 5 "leucogranite"	Varin monzonite	Michaud monzonite	Bon-Désir granite
Quartz	14	30	14	27	33
Plagioclase ($An_{5–100}$)	38	32	35	30	24
K-Feldspar	38	33	36	17	32
Albite ($An_{0–5}$)	Trace	3	Trace	2	4
Total Alkali Feldspar	*38*	*36*	*36*	*19*	*36*
Amphibole	5	-	10	4	-
Biotite	2	Trace	2	9	4
Clinopyroxene	-	-	-	Trace	-
Ilmenite	1	Trace	1	2	-
Iron Oxide	Trace	2	1	4	-
Titanite	Trace	-	-	-	-
Rutile	-	-	-	-	-
Pyrite	-	-	-	Trace	Trace
Pyrrhotite	-	-	-	Trace	-
Apatite	Trace	-	Trace	2	Trace
Allanite	Trace	-	Trace	Trace	-
Zircon	Trace	Trace	Trace	Trace	Trace
Monazite	-	-	-	-	Trace
Fergusonite	-	Trace	-	-	-
Chlorite	Trace	Trace	1	2	1

Major mineral ≥ 10%; Minor mineral 1 – 10%; Trace mineral < 1%.

4.1.1. Manic 5 Plutonic Suite (04-445a, 04-445b)

The Manic 5 Plutonic Suite is exposed in the mid-*P* segment, south of the Manicouagan Reservoir, as a north-south trending kilometre-scale pluton (Fig. 3.1) that intruded the ca. 1.50 Ga Plus-Value Complex (Dunning & Indares 2010; Moukhsil et al. 2013b; Moukhsil et al. 2014). The Suite is dominated by porphyritic granite to monzonite (sample 04-445a; 1065 ± 8 Ma; Fig. 4.1a, grey unit) with commingling texture and diffuse contacts between felsic components and is apparently crosscut by a pinkish “leucogranite” unit (04-445b; undated; Fig. 4.1a pink unit).

Sample 04-445a of the main unit is a weakly foliated monzonite dominated by porphyroclastic alkali feldspar (perthite to mesoperthite) with subordinate plagioclase and quartz

and with minor amphibole and biotite (Fig. 4.2a; Fig 4.3a). Anhedral plagioclase commonly contains an oligoclase core (~Ab_{80}) enclosed by a thin albite rim (~Ab_{98}) with an abrupt boundary (Fig. 4.4a). Perthite consists of an orthoclase host (~Or_{87}) with oligoclase exsolution ($Ab_{81\text{-}83}$; Fig. 4.4b). Subhedral to anhedral, medium-grained pargasite amphibole (X_{Fe} ~0.59 – 0.62, Fig 4.4c) and biotite (X_{Mg} ~0.4 – 0.5; Al^{VI} ~0.1 – 0.2 apfu, Fig. 4.4d–f) is associated with trace of titanite + ilmenite + magnetite, zircon, apatite and allanite. Biotite is commonly altered to chlorite.

The second unit (04-445b, "leucogranite") is dominated by porphyroclastic microperthitic mesoperthite, plagioclase, and quartz, with trace of accessory minerals (Fig. 4.2b). Anhedral plagioclase is almost pure albite (Fig. 4.4a). The mesoperthite has an orthoclase host (~Or_{91}) with albite exsolution (~Ab_{81}; Fig. 4.4b). Trace minerals include ilmenite, magnetite, chlorite, anhedral zircon, and rare, micrometre-scale fergusonite. No pyroxene, amphibole or biotite is present.

4.1.2. Varin Plutonic Suite (22-AF-37)

The Varin Plutonic Suite is a 100-km wide batholith in the Baie-Comeau region, bordering the ~1.14 Ga Vallant Anorthosite Complex to the north (Fig 3.1). The Suite was first documented by Gobeil et al. (2006), and was described as megacrystic, locally orthopyroxene-bearing monzonite (Moukhsil et al. 2009; Moukhsil et al. 2011). Two monzonite samples were dated at 1057.6 ± 1.7 Ma and 1007.7 ± 1.7 Ma in two different parts of the suite (David et al. 2009; Fig. 3.1). The investigated sample, 22-AF-37, was collected in the southeastern part of the suite and is a massive, megacrystic monzonite (Fig. 4.1b).

This sample (Fig. 4.2c) is dominated by alkali feldspar and plagioclase with minor biotite and amphibole. Subhedral plagioclase is mantled by anhedral alkali feldspar in an anti-rapakivi texture (Fig. 4.3b). Euhedral biotite and poikilitic amphibole fill the interstitial space associated with inclusions of anhedral quartz, ilmenite-magnetite, euhedral zircon, subhedral apatite and euhedral allanite (Fig. 4.3c). The average plagioclase composition is $Ab_{76,}$ and it is normally zoned from core to rim (Ab_{73} to Ab_{80}; Fig. 4.4a). Alkali feldspar is perthitic to mesoperthitic and consists of an orthoclase host (~Or_{93}) with oligoclase exsolution (~Ab_{93}; Fig. 4.4b). In the interstitial space, subhedral to anhedral, homogeneous, medium-grained, poikilitic pargasite

amphibole (X_{Fe} ~0.76 – 0.78; Fig. 4.4c) and euhedral, skeletal annite biotite (X_{Mg} ~0.2 – 0.3; Al^{VI} < 0.2 apfu; Fig. 4.4d–f) are present.

Table 4.2 Average compositions of amphibole and results of amphibole-based thermobarometry

Plutonic Suites/Units	Amphibole Texture	∑C site	∑A site	*P* (kbar) [1]	*T* (ºC) [2]
Manic 5 monzonite 04-445a	inclusion-free	0.67	0.90	6.1	962
	poikilitic	0.63	0.93	6.0	968
	inclusion-free	0.69	0.89	6.0	967
	poikilitic	0.64	0.93	6.1	965
	poikilitic	0.70	0.87	6.0	965
	poikilitic	0.67	0.87	6.1	947
Varin monzonite # 22-AF-37	poikilitic	0.84	0.81	6.5	972
	poikilitic	0.85	0.81	6.7	969
	poikilitic	0.85	0.80	6.7	964
	poikilitic	0.86	0.80	6.4	977
	poikilitic	0.83	0.83	6.7	968
	poikilitic	0.87	0.79	6.9	951
	inclusion-free	0.84	0.79	6.8	949
	inclusion-free	0.84	0.82	7.0	960
	inclusion-free	0.89	0.79	7.0	965
	inclusion-free	0.87	0.81	6.6	975
	inclusion-free	0.88	0.79	6.6	968
	poikilitic	0.88	0.79	6.8	963
Michaud monzonite 15-PA-187A	inclusion-free	0.76	0.69	5.4	848
	inclusion-free	0.75	0.67	5.3	834
	inclusion-free	0.79	0.64	5.5	825
	pseudomorph after Cpx	0.73	0.66	5.4	819
	pseudomorph after Cpx	0.70	0.66	5.2	812

[1] Al-in-amphibole barometer (Anderson & Smith 1995).

[2] Plagioclase-Amphibole thermometry (Holland & Blundy, 1994).

T could be underestimated due to chemical disequilibria in rapakivi granitoids (Anderson & Smith, 1995).

4.1.3. Michaud Monzonite (15-PA-187A)

Michaud Monzonite is a kilometre-scale pluton located at the northern boundary of the ESB (Fig 3.1). The unit was first reported by Rondot (1986) and further investigated by Groulier et al. (2018a). The core of the Michaud pluton is coarse-grained monzonite with enclaves of

mafic and metasedimentary rocks. Sample 15-PA-187A from this intrusion is dated at 1063 ± 3 Ma (Fig. 4.1c; Groulier et al. 2018a).

Sample 15-PA-187A is a weakly foliated quartz-monzonite. In thin section (Fig. 4.2d), it consists of megacrystic perthitic alkali feldspar rimmed by myrmekite in a quartz and plagioclase groundmass with clusters of anhedral, medium-grained amphibole, biotite, resorbed clinopyroxene, Fe-Ti oxides and apatite (Fig. 4.3d). Anhedral plagioclase is locally anti-perthitic, with orthoclase exsolution (~$Or_{93}Ab_{7}$) within oligoclase grains (~Ab_{70}; Fig. 4.4a). The alkali feldspar composition is orthoclase (~$Or_{90}Ab_{10}$) with oligoclase exsolution (~$Ab_{75}An_{25}$; Fig. 4.4b). The mafic minerals include pargasite amphibole (X_{Fe} ~0.43 – 0.47, Fig. 4.4c), biotite (X_{Mg} ~0.5 – 0.6; $Al^{VI} < 0.2$ apfu; Fig. 4.4d–f) and resorbed diopside clinopyroxene (Fig. 4.4g). Other trace minerals include zircon, apatite, allanite and Fe-sulphides.

Table 4.3 Summary of the average compositions of feldspars in the studied granitoids.

Unit	Type	n	Areal proportion		Afs composition (%)			Plag composition (%)			Re-integrated composition (%)			Ternary feldspar *T* (ºC)[1]
			Afs	Plag	Or	Ab	An	Or	Ab	An	Or	Ab	An	
Manic 5 monzonite 04-445a	M	2	0.7	0.3	89.4	10.7	0.0	0.8	83.3	15.9	59.3	35.3	5.4	~950–1000
	P	3	0.8	0.2	89.5	10.4	0.0	0.8	82.7	16.5	74.0	23.0	2.9	~800–900
	Plag	3	-			-		1.7	79.5	18.8		-		-
"Manic 5 "leucogranite" 04-445b	M	6	0.5	0.5	93.4	6.6	0.0	0.7	93.0	6.3	51.0	46.1	2.9	~800–850
	Plag	4	-			-		0.6	93.2	6.2		-		-
Varin monzonite 22-AF-37	C	1	0.7	0.3	91.4	8.4	0.2		-			-		-
	M	3	0.6	0.4	91.1	8.9	0.1	0.8	81.4	17.8	55.6	37.4	7.0	~1000
	P	7	0.7	0.3	91.4	8.6	0.1	0.7	81.5	17.8	66.4	28.6	4.9	~900–1000
	Plag	6	-			-		1.7	76.1	22.2		-		-
Michaud monzonite 15-PA-187A	A	1	0.0	1.0	93.3	6.7	0.0	2.0	69.4	28.6	5.0	67.4	27.7	~700
	P	4	0.8	0.2	90.2	9.8	0.0	0.9	75.6	23.5	70.6	24.3	5.2	~1000
	Plag	4	-			-		1.5	70.9	27.6		-		-
Bon-Désir granite 15-PA-107A	A	2	0.2	0.8	99.1	0.8	0.0	0.9	77.4	21.8	22.9	60.2	16.9	~1000
	P	4	0.9	0.1	94.6	5.4	0.0	0.6	98.4	1.0	82.6	17.2	0.2	< 600
	Plag	3	-			-		1.0	77.5	21.5		-		-

Note: Afs – Alkali feldspar; A – anti-perthite; C – cryptoperthite; M – mesoperthite; P – perthite; Plag – plagioclase

[1] *T* ranges estimated graphically by ternary feldspar model at 5 kbar (Elkins & Grove 1990)

4.1.4. Bon-Désir Granite (15-PA-107A)

The Bon-Désir Granite is a kilometre-scale pluton outcropping in southern ESB, with its southern part incised by the Saint Lawrence River (Fig. 3.1). This pluton was first reported by Rondot (1986) with further investigated by Groulier et al. (2018a). The core of the Bon-Désir pluton is coarse-grained granite with centimetric mafic enclaves (Fig. 4.1d). Sample 15-PA-107A (1086 ± 2 Ma; Groulier et al. 2018a) comes from the homogeneous part of the core.

Sample 15-PA-107A contains porphyritic, perthitic alkali feldspar and quartz, with lesser plagioclase and minor biotite associated with accessory minerals (Fig. 4.2e). Plagioclase is locally anti-perthitic, with orthoclase blebs (~Or_{99}) or exsolution within oligoclase grains (~Ab_{77}; Fig. 4.4a). Perthitic alkali feldspar consists of an orthoclase host (~$Or_{94}Ab_6$) with albite exsolution (~Ab_{99}; Fig. 4.4a). Biotite, rich in Fe and Al, is close to the siderophyllite end-member (X_{Mg} ~0.3 – 0.4; Al^{VI} ~0.6 – 0.7 apfu; Fig. 4.4d–f). Undulatory extinction and subgrain rotation in quartz attest to post-crystallisation ductile deformation. Traces of apatite, zircon, monazite, and pyrite are present, but amphibole and Fe-Ti oxides are absent. Rare, fractured, anhedral monazite is associated with apatite.

4.2. Thermobarometry based on major minerals

For a given bulk rock composition, intensive parameters: *P, T*, and fO_2 govern the mineral chemistry. This section presents the results of amphibole-based thermobarometry and ternary feldspar thermometry. Pargasite amphibole is common in the samples from the Manic-5 (04-445a), Varin (22-AF-37) and Michaud (15-PA-187A) monzonites. Therefore, Al-in-amphibole barometry and amphibole–plagioclase thermometry were applied to these samples to infer *P–T* conditions of magma crystallisation. On the other hand, ternary feldspars with similar textures are ubiquitous in all samples, so they are invaluable for estimating and comparing the crystallisation *T* between plutons across the region. Lastly, Fe–Ti oxide oxybarometry has been attempted to estimate the fO_2 of the magma, but where present, analysed ilmenite and magnetite pairs have almost ideal compositions; therefore, estimation of fO_2 by the Fe–Ti oxide oxybarometer (Ghiorso & Evans 2008) was unfeasible.

4.2.1. Amphibole-based thermobarometry and thermometry

The Al-in-amphibole barometer (Anderson & Smith 1995) yields crystallisation *P* ranging from 5.4 kbars (Michaud) to 6.1 kbars (Manic 5) and 6.7 kbars (Varin; Fig. 4.5a). Yet, the highest *P*, recorded by the Varin monzonite, may be overestimated because the anti-rapakivi texture is observed in this sample (Anderson & Smith 1995). On the other hand, the crystallisation *T* estimated by the amphibole–plagioclase thermometer (Holland & Blundy 1994) is in the range of 947 – 968ºC and 949 – 977ºC for the Manic 5 and Varin monzonites, respectively (Fig. 4.5b). In contrast, the Michaud monzonite gave a lower *T* range of 812 – 848ºC, which is still in the high-*T* regime (Miller et al. 2003).

4.2.2. Ternary feldspar thermometry

Perthitic alkali feldspar and plagioclase are present in all samples, so the crystallisation *T* ranges can be estimated by ternary feldspar thermometry, using reintegrated feldspar compositions (e.g. Nekvasil 1992). Perthite and mesoperthite are present in Manic 5 (04-445a), Varin (22-AF-37) and Michaud (15-PA-187A) monzonite samples with a composition of orthoclase, and oligoclase (04-445a and 22-AF-37) or andesine (15-PA-187A) exsolution lamellae (for details on feldspar compositions see Table 4.2). Generally, the *T* increases with *P*, but between 5 and 8 kbars, the ternary feldspar model (Elkins & Grove 1990) is little affected by *P*, and the model at 5 kbars was taken for the minimum *T* estimation. Overall, the re-integrated compositions of the alkali feldspar yielded a *T* range of ~800–1000ºC at 5 kbar. The results for each sample are shown in Figure 4.6.

In 04-445a, mesoperthite and perthite have distinct compositions and record different *T* conditions. The mesoperthite has a higher albite content and records *T* at ~950–1000ºC. In contrast, perthite has a higher modal orthoclase and yields *T* at ~800–900ºC. Moreover, in 04-445b, alkali feldspar is orthoclase with albite exsolution lamellae and yields *T* of ~800–850ºC. In 22-AF-37, K-feldspar crystallised over a steep *T* profile. The mesoperthite and some perthite were formed at a *T* of ~1000ºC, but increasing modal orthoclase in perthite results in a decreasing crystallisation *T* of ~900–1000ºC.

Both samples from the granites of the ESB contain perthite and anti-perthite. In 15-PA-187A, perthite has an orthoclase host with oligoclase exsolution lamellae, with the average re-integrated composition yielding ~1000ºC. Anti-perthite has an oligoclase host with subhedral orthoclase exsolution and records *T* below 700ºC. Conversely, in 15-PA-107A, anti-perthite has an oligoclase composition with subhedral blebs of pure orthoclase and records *T* slightly below 1000ºC, while perthite has an orthoclase composition with almost pure albite exsolution lamella, with a re-integrated composition yielding *T* below 600ºC.

4.3. Whole-rock lithogeochemistry

The samples analysed for lithogeochemistry (major, trace and Sm–Nd) are 04-445a (monzonite), 04-445b ("leucogranite") of the Manic 5 Plutonic Suite and 22-AF-37 from the Varin Plutonic Suite. The major and trace element geochemistry of the Michaud monzonite and Bon-Désir granite from the ESB was presented by Groulier et al. (2018a). All data from Manic 5, Varin and the ESB plutons are reported in Appendix A and are highlighted in Figures 4.7 to 4.9.

In the Manic 5 Plutonic Suite, sample 04-445a is a ferroan, metaluminous, alkali-calcic, high-Zr monzonite, and falls within the within-plate field close to the boundary with volcanic arc field (Figs. 4.7a & 4.8a). It has variably positive Eu anomalies, is enriched in Ba and Rb on the PM-normalised plot, and its REE profile is comparable to the overall REE profiles of the Suite (Fig. 4.9a). In contrast, the Manic 5 "leucogranite" is very depleted in MgO and high in silica, despite being ferroan, weakly peraluminous, and alkali-calcic, and has 592 ppm Zr. It distinctively falls in the volcanic-arc granite field on the Nb–Y plot (Figs. 4.7a & 4.8a). On the PM-normalised diagram, the sample is low in Ba but high in Rb, very fractionated Zr/Hf and Nb/Ta ratios, and is very depleted in REE relative to the REE abundances in the rest of the Suite (Fig. 4.9a). These features indicate that sample 04-445a is a strongly fractionated felsic rock.

The sample (22-AF-37) of the Varin Plutonic Suite is a ferroan, metaluminous to weakly peraluminous, alkali-calcic monzonite. It has 829 ppm Zr and falls on the boundary between the volcanic arc and within-plate granite fields (Figs. 4.7b & 4.8b). The PM-normalised diagram shows positive or lacks negative Eu anomalies, low Rb and enrichment in REE relative to the remainder of the rocks of the Varin Plutonic Suite (Fig. 4.9b).

The sample (15-PA-187A) of the Michaud pluton is a ferroan, metaluminous alkali-calcic monzonite, has 456 – 515 ppm Zr, and falls within the within-plate granite field on the Nb–Y plot (Figs. 4.7c & 4.8c). On the PM-normalised diagram, the sample is high in Ba but depleted in Sr, exhibits chondritic-like Zr/Hf and Nb/Ta ratios, no Eu anomaly, and LREE enrichment relative to HREE. It is worthwhile noting that the Bon-Désir granite (15-PA-107A) is the only analysed magnesian, weakly peraluminous granite and plots in the volcanic-arc granite field (Fig. 4.7c & 4.8c). Although it has 181 – 187 ppm Zr, lower than the samples from the other plutons, it is still classified as A-type granite because of its high Ga/Al ratio (Fig. 4.7c). The sample is enriched in Th and U, with a pronounced negative Eu anomaly and high Rb, as well as strongly negative Nb–Ta–Ti anomalies (Fig. 4.9c). The Bon-Désir granite stands apart from the Michaud monzonite, having different major element geochemistry and REE profiles. These differences suggest the two plutons likely have different magmatic histories and origins.

4.3.1. Zircon saturation temperature

Zircon saturation temperatures (T_{Zr}) were estimated from the whole-rock geochemistry (Watson & Harrison 1983) (Fig. 4.10). Varin monzonite (22-AF-37) gave the highest T_{Zr} at ~1000ºC, compared to the Manic 5 monzonite (04-445a, T_{Zr} ~ 952ºC) and Michaud monzonite (15-PA-187A, T_{Zr} ~ 927 – 940 ºC), all having compositional M values between 0.92 to 1.00 within the calibrated range. The result shows that the zircon in these plutons reached saturation at high-*T*. Nevertheless, the Manic 5 "leucogranite" (04-445b) and Bon-Désir granite (15-PA-107A) fall in the uncalibrated range (M < 0.85) and are unsuitable for the thermometry.

4.3.2. Whole-rock Sm–Nd isotopes

Samples from Manic 5 and Varin were analysed for Sm–Nd isotopes, and the data are considered together with those obtained by Groulier et al. (2018a) for Michaud and Bon-Désir. The results are displayed in Table 4.4 and Figure 4.11. The $\varepsilon_{Nd}(t)$ values were calculated based on previously published crystallisation ages available by TIMS (Manic 5 monzonite, Dunning & Indares 2010; ESB granitoids, Groulier et al. 2018a), except for the Manic 5 "leucogranite" and the Varin monzonite that were previously undated, and for which new LA–ICP–MS dates were used (See section 4.4).

The two samples from the Manic 5 Plutonic Suite gave contrasting results. Sample 04-445a from the main monzonitic unit (one analysis) yielded a $^{147}Sm/^{144}Nd$ ratio of 0.1163, and a $^{143}Nd/^{144}Nd$ ratio of 0.511954 ± 7, corresponding to $\varepsilon_{Nd}(0) = -13.3$ and $\varepsilon_{Nd}(t) = -2.4$ at 1063 Ma. The Nd model age (T_{DM}) at 1699 Ma suggests the rock is derived from a Labradorian-age source. Sample 04-445b from the 'leucogranite' (duplicate analysis) yielded $^{147}Sm/^{144}Nd$ ratios of 0.1127 and 0.1060 and 0.512195 and $^{143}Nd/^{144}Nd$ ratios of 0.512160 ± (5–7). The analyses yield $\varepsilon_{Nd}(0)$ of −8.6 and −9.3, equivalent to $\varepsilon_{Nd}(t)$ +5.9 and +6.4 at 1361 Ma, respectively. The $\varepsilon_{Nd}(t)$ plots above the depleted mantle model (ε_{Nd} of DM equals +4.9 at 1361 Ma), indicating that the "leucogranite" represents very primitive material extracted from a juvenile mantle.

Sample 22-AF-37 from the Varin Plutonic Suite (triplicate analysis) yielded $^{147}Sm/^{144}Nd$ ratios from 0.1141 to 0.1174 and $^{143}Nd/^{144}Nd$ ratios from 0.512049 to 0.512071 (± 6–7). These data define a narrow range of $\varepsilon_{Nd}(0)$ from −11.1 to −11.5, equivalent to $\varepsilon_{Nd}(t)$ from −1.0 to −1.1 at 986 Ma. The calculated T_{DM} at 1534 and 1518 Ma correspond to a Pinwarian age.

Table 4.4 Result of Sm–Nd isotopic data.

Plutonic Suites/Units	analysis	Rock Type[2]	Nd (ppm)	Sm (ppm)	$^{147}Sm/^{144}Nd$	$^{143}Nd/^{144}Nd$	2SE	$\varepsilon_{Nd}(0)$	*t* (Ma)	$\varepsilon_{Nd}(t)$	T_{DM} (Ma)
Manic 5 monzonite 04-445a	1	M	58.98	11.35	0.1163	0.511954	7	−13.3	1065	−2.4	1699
Manic 5 "leucogranite" 04-445b	1	G	2.66	0.50	0.1127	0.512195	5	−8.6	1361	+5.9	–
	2		2.63	0.46	0.1060	0.512160	7	−9.3		+6.4	–
Varin monzonite 22-AF-37	1	M	51.84	10.07	0.1174	0.512071	6	−11.1	986	−1.1	1534
	2		53.66	10.29	0.1159	0.512064	7	−11.2		−1.0	1522
	3		53.43	10.09	0.1141	0.512049	7	−11.5		−1.1	1518
Michaud monzonite 15-PA-187A[1]	1	M	71.72	14.56	0.1227	0.512159	7	−9.3	1063	+0.7	1478
Bon-Désir granite 15-PA-107A[1]	1	G	37.73	7.82	0.1253	0.512161	7	−9.3	1085	+0.6	1517

Note: ε_{Nd} is calculated using present-day CHUR ratios $^{143}Nd/^{144}Nd = 0.512638$ and $^{147}Sm/^{144}Nd = 0.1967$ (DePaolo 1988). 2SE – two times the standard error of the mean of the isotopic ratios reported in the last decimal place; $\varepsilon_{Nd}(0)$ – ε_{Nd} at present-day; $\varepsilon_{Nd}(t)$ – ε_{Nd} at the time of crystallisation *t* (Ma). **1** – The Sm–Nd isotopic data of samples 15-PA-107A and 15-PA187A were analysed by Groulier et al. (2018a). **2** – Abbreviation: M – monzonite; G – granite.

On the ε_{Nd}–age plot (Fig. 4.11), the $\varepsilon_{Nd}(t)$ of the samples, except for 04-445b, are at or immediately below CHUR. Their T_{DM} values (~1.7–1.4 Ga) and their evolution lines largely overlapping the evolution of the Quebecia crust imply that the granitoids are formed by partial melting of Mesoproterozoic or Paleoproterozoic crustal components derived from the depleted mantle at 1.7 – 1.4 Ga. In the low-*P* segments, all samples have a similar isotopic evolution and Pinwarian T_{DM} (Varin: 1534 – 1518 Ma; Bon-Désir: 1517 Ma; Michaud: 1478 Ma). In contrast, in the mid-*P* segment yielded an older T_{DM} (1699 Ma) for the Manic 5 monzonite and indicates the reworking of the Paleoproterozoic crust.

4.4. Zircon data

Zircon from all samples was analysed in situ with LA–ICP–MS for U–Pb dating, trace element geochemistry and Lu–Hf isotopes. Manic 5 monzonite and the granitoids for the ESB (Michaud and Bon-Désir) were previously dated by TIMS U–Pb zircon analysis. The reasons for the new, in-situ LA–ICP–MS dating are: (a) to check for potential inheritance in the zircon record; (b) to test the hypothesis that the Manic leucogranite is indeed part of the Manic 5 plutonic Suite; and (c) to provide additional age data on the Varin Plutonic Suite, that so far, has the widest range of crystallisation ages (1058 and 1007 Ma, Moukhsil et al. 2011).

Representative zircon photomicrographs and CL images are shown in Figures 4.12 and 4.13, respectively, and the full CL image collages for each sample are in Appendix C. Data for zircon U–Pb analyses, concordia diagrams and weighted average ages are reported in Appendix D and displayed in Figures 4.14 and 4.15. The results are summarised in Table 4.5.

4.4.1. Zircon morphologies and U–Pb ages

4.4.1.1. Sample 04-445a (Manic 5 monzonite)

Zircons in 04-445a are prismatic euhedral or rounded, clear to brown or yellow grains. with rare anhedral grains with irregular shapes. The width-to-length ratio ranges from 1:2 to 1:5, with widths ranging from 70 to 150 μm. Local brown corrosion rings, mineral inclusions and radial fractures are noted. Under CL, the grains show homogeneous zones or sector growth. Irregular dark-CL bands are present in overall homogeneously bright-CL zones. Also, dark-CL rims with recrystallised or convoluted textures are interpreted as metamict domains.

Thirty-one analyses cover all CL domains. First, 20 analyses in the sector-zoned or homogeneous domains produce 19 overlapping but discordant points, with a lead loss shown in a wide range of $^{206}Pb/^{238}U$ ages from 1064 to 984 Ma and $^{207}Pb/^{206}Pb$ ages from 1114 to 1026 Ma. A discordant age model anchored at present-day (0 Ma) returns a concordant age at the upper intercept at 1073 ± 19 Ma (MSWD=0.43, p=0.98), interpreted as the age of crystallisation. Second, 11 analyses in recrystallised or convoluted domains yielded 10 overlapping concordant points, with a range of $^{206}Pb/^{238}U$ ages from 1051 to 999 Ma and $^{207}Pb/^{206}Pb$ ages from 1104 to 1028 Ma. The weighted average $^{206}Pb/^{238}U$ age at 1026 ± 12 Ma (MSWD=0.89, p=0.53) is inferred to be a metamorphic age.

4.4.1.2. Sample 04-445b (Manic 5 "leucogranite")

Zircons in 04-445b are clear yellow to turbid, stubby euhedral to rounded grains, and commonly anhedral or fragmented. The width-to-length ratio ranges from 1:1 to 1:3, with the widths ranging from 40 to 100 μm. Internal concentric fractures and resorption texture are often displayed. Under CL, dark-CL oscillatory zoning or "fir-tree" zoned domains are dominant. Oscillatory zoning is formed by igneous crystallisation, while fir-tree zoning is a metamorphic overgrowth texture (Vavra et al. 1999; Corfu et al. 2003). Most grains only display one of the two domains. Nevertheless, rare grains display a clear relationship between an oscillatory-zoned core and a fir-tree overgrowth rim, which grows in different crystallographic orientations and is bounded by a geometrically irregular resorption surface.

The zircon internal textures and ages are inherently associated in this sample. Twenty-six in-situ analyses of zircon from this rock yield two age clusters that correspond to CL domains. First, four out of six overlapping concordant points in the oscillatory-zoned domains have a range of $^{206}Pb/^{238}U$ concordant ages from 1366 to 1353 Ma and $^{207}Pb/^{206}Pb$ ages from 1372 to 1351 Ma. The weighted mean $^{206}Pb/^{238}U$ age of 1361 ± 11 Ma (MSWD=0.21, p=0.89) is interpreted as the crystallisation age of the protolith. Second, 17 out of 20 analyses in the fir-tree domain yielded a concordant cluster with a range of $^{206}Pb/^{238}U$ concordant ages from 1063 to 1026 Ma and $^{207}Pb/^{206}Pb$ ages from 1096 to 1048 Ma. The weighted mean $^{206}Pb/^{238}U$ age of 1042.0 ± 3.7 Ma (MSWD=2.1, p=0.0067) is inferred to be a metamorphic age. The crystallisation age shows that

the “leucogranite” is older than, and not part of, the ca. 1065 Ma Manic 5 Plutonic Suite. Instead, the ‘leucogranite’ may be a raft in the magma chamber or part of the wall rock.

4.4.1.3. Sample 22-AF-37 (Varin monzonite)

Zircons in 22-AF-37 are clear to pale yellow, prismatic or equant euhedral grains with rare anhedral examples. The width-to-length ratio ranges from 1:1 to 1:5, with the widths ranging from 50 to 200 μm. Mineral inclusions are rare. Under CL, the grains show homogeneous or sector-zoned domains. Dark and bright CL bands are present inside some grains.

Twenty-one in-situ analyses of zircon from this rock yielded an older cluster and younger dispersed data, with an overall range of $^{206}Pb/^{238}U$ ages from 991 to 933 Ma and $^{207}Pb/^{206}Pb$ ages from 1130 to 1020 Ma, with 3–15% discordance. On the other hand, with the same discordance filter, the older cluster ($^{206}Pb/^{238}U$ age >975 Ma, n=4) yielded a weighted average $^{206}Pb/^{238}U$ age of 986 ± 19 Ma (MSWD=0.024, p=1). In addition, considering all data which are less than 10% discordant, calculation of 13 analyses yielded a weighted average $^{206}Pb/^{238}U$ age of 960 ± 10 Ma (MSWD=1.1, p=0.38) and a weighted average $^{207}Pb/^{206}Pb$ age of 1045 ± 25 Ma (MSWD=0.14, p=1). The $^{207}Pb/^{206}Pb$ age is comparable to, but the $^{206}Pb/^{238}U$ age is younger than the published TIMS ages (~1058–1007 Ma). The younger ages are interpreted to reflect Pb loss rather than a younger magmatic event. Therefore, the weighted average $^{206}Pb/^{238}U$ age of the older cluster (986 ± 19 Ma) would be used as a minimum age of crystallisation, but further verification of the final crystallisation age by TIMS is suggested.

4.4.1.4. Sample 15-PA-187A (Michaud monzonite)

Zircons in 15-PA-187A are clear to pale yellow, euhedral prismatic grains. The width-to-length ratio ranges from 1:2 to 1:4, with the widths ranging from 80 to 200 μm. Mineral inclusions are rare. Under CL, an internal cyclic CL pattern is prominent in most of the grains. The resorbed bright, chaotic or sector-zoned inner core is surrounded by a resorbed dark lobate or sector-zoned outer core, then another bright, sector-zoned rim. Otherwise, single homogeneous or sector-zoned grains are present. Inherited zircon occurs as resorbed dark, xenocrystic cores.

Fifty-three in-situ analyses of zircon from this rock yield 46 clustered concordant points at Grenvillian age and three outliers of xenocrystic cores. The Grenvillian cluster has $^{206}Pb/^{238}U$

ranging from 1103 to 1013 Ma and $^{207}Pb/^{206}Pb$ from 1142 to 983 Ma, including sector-zoned, dark lobate aurora-light or homogeneous domains, even though the latter two domains have younger concordant ages. The weighted average of $^{206}Pb/^{238}U$ ages at 1061.9 ± 4.6 Ma (MSWD=1.2, p=0.2) is interpreted as the crystallisation age of this intrusion. As for the inherited zircons, two out of three analyses in xenocrystic cores are concordant, returning $^{207}Pb/^{206}Pb$ ages at 2045 ± 77 Ma and 1886 ± 79 Ma in the 2.0 – 1.8 Ga range, interpreted as the inherited age of the Paleoproterozoic crust.

4.4.1.5. Sample 15-PA-107A (Bon-Désir granite)

Zircons in 15-PA-107A are clear to yellow, rarely turbid, prismatic euhedral grains; some irregularly rounded to anhedral grains are present. The width-to-length ratio ranges from 1:1 to 1:3, with the widths ranging from 60 to 150 μm. Mineral inclusions are rare. The rim is commonly concentrically fractured along the geometrical faces. Under CL, the grains show aurora-light, homogeneous or sector-zoned cores with a dark, concentric, severely fractured rim. Local recrystallisation, as transgressive patchy, lobate or chaotic texture is observed within sector growth domains. Also, resorbed dark, xenocrystic cores are noted in some zircon grains. Annealed cracks filled with dark-CL material are commonly observed.

Twenty-nine in-situ analyses yield 12 points of Grenvillian age, three points clustering at 1.4–1.3 Ga and four points at 1.8–1.7 Ga. The rest of analyses were rejected due to mixed domains, which produced mixed ages lower than the main cluster, or discordance over 10%. First, 12 points form an array in Grenvillian-age, with Pb-loss evident by a range of $^{206}Pb/^{238}U$ ages from 1100 to 1048 Ma and $^{207}Pb/^{206}Pb$ ages ranging from 1144 to 1061 Ma. The weighted average of $^{206}Pb/^{238}U$ ages at 1070 ± 11 Ma (MSWD=0.48, p=0.92) is interpreted as the crystallisation age of this intrusion. Second, the 1.4–1.3 Ga cluster includes two concordant and one discordant point, with a range of $^{206}Pb/^{238}U$ ages from 1462 to 1290 Ma and $^{207}Pb/^{206}Pb$ ages from 1479 to 1433 Ma. A discordant age model anchored at present-day (0 Ma) returns a concordant age at the upper intercept at 1458 ± 45 Ma (MSWD=0.5, p=0.61), interpreted as a Pinwarian, inherited age. Third, four overlapping concordant points in the 1.8–1.7 Ga forms a cluster, with a range of $^{206}Pb/^{238}U$ ages from 1797 to 1732 Ma and $^{207}Pb/^{206}Pb$ ages from 1853 to 1805 Ma. A weighted average $^{207}Pb/^{206}Pb$ age at 1826 ± 41 Ma (MSWD=0.25, p=0.86) is

interpreted as an inherited age at Paleoproterozoic. The LA–ICP–MS crystallisation age is slight younger than the published TIMS age (1086 ± 2 Ma).

Table 4.5 Summary of zircon U–Pb ages from the literature (TIMS) and this study (LA–ICP–MS)

Plutonic Suites/Units	Ellipse Distribution	Analysis type	Age ± 2σ	n	MSWD	Interpretation
Manic 5 monzonite 04-445a	concordant to slightly discordant	TIMS w. m. $^{207}Pb/^{206}Pb$	**1065 ± 8** [a]	4	0.24	crystallisation
	overlapping, concordant cluster	w. m. $^{206}Pb/^{238}U$	1026 ± 12	10	0.89	metamorphic
	overlapping but discordant	Disc. at 0Ma upper intercept	1074 ± 19	19	0.43	crystallisation
Manic 5 "leucogranite" 04-445b*	overlapping, concordant cluster	w. m. $^{206}Pb/^{238}U$	1042 ± 3.7	17	2.1	metamorphic
	overlapping, concordant cluster	w. m. $^{206}Pb/^{238}U$	1361 ± 11	6	0.21	crystallisation
Varin monzonite 22-AF-37*	An older cluster with younger dispersion	w. m. $^{206}Pb/^{238}U$	986 ± 19	4	0.024	crystallisation
		w. m. $^{207}Pb/^{206}Pb$	1058 ± 20	21	0.43	crystallisation
Michaud monzonite 15-PA-187A	overlapping, concordant cluster	TIMS w. m. $^{207}Pb/^{206}Pb$	**1063 ± 3** [b]	5	0.13	crystallisation
	overlapping, concordant cluster	w. m. $^{206}Pb/^{238}U$	1061.9 ± 4.6	46	1.2	crystallisation
Bon-Désir granite 15-PA-107A	overlapping, concordant cluster	TIMS w. m. $^{207}Pb/^{206}Pb$	**1086 ± 2** [b]	6	0.26	crystallisation
	overlapping, concordant cluster	w. m. $^{206}Pb/^{238}U$	1070 ± 11	12	0.48	crystallisation
	2 concordant points, 1 discordant point	Disc. at 0Ma upper intercept	1458 ± 45	3	0.5	inherited
	overlapping, concordant cluster	w. m. $^{207}Pb/^{206}Pb$	1826 ± 41	4	0.25	inherited

Note: 2σ – two times standard deviation; w. m. – weighted mean
* No reported TIMS ages; [a] Dunning & Indares (2010); [b] Groulier et al. (2018)

4.4.2. Trace element geochemistry

Trace elements can provide additional information on the origin of different zircon CL domains. For instance, chondrite-normalised REE diagrams show the fractionation of REE in zircons (McDonough & Sun 1995). Th/U *vs* Ce/U ratios can be used to distinguish magmatic versus metamict zircons (Roberts et al. 2024), and U/Yb *vs* Gd/Yb ratios illustrate zircon fractionation versus the MREE–HREE depletion (Grimes et al. 2015). The trace element data is reported in Appendix E, and selected plots are shown in Figures 4.16 and 4.17.

Based on CL images, most zircons are magmatic, homogeneous or have oscillatory, sector zoning (Fig. 4.13). In addition, they show negative REE slopes with depleted LREE and enriched HREE, which are typical REE patterns for igneous zircon (Fig. 4.16). In the Th/U–Ce/U diagram (Fig. 4.17a), these domains have high Th/U and Ce/U, consistent with a magmatic origin (Roberts et al. 2024). In the U/Yb–Gd/Yb diagram (Fig. 4.17b), the magmatic zircon domains in each sample form unique arrays for their fractionation trends, and their slopes are negatively correlated.

In addition, Grenvillian-age metamict zircon domains (fir-tree, convoluted, recrystallised, etc.) were also identified in the two Manic 5 samples, and these have different trace element patterns compared to the magmatic zircons. In the monzonite, metamict zircon domains form a cluster with low Th/U (<0.3) and Ce/U (<0.05) away from magmatic domains, which have contrastingly higher Th/U and Ce/U (Fig. 4.17a). In the "leucogranite", the metamict zircons are enriched in Hf (~3–4 wt% HfO_2) and Y and depleted in Th (Fig. 4.16b). Specifically, the "leucogranite" fir-tree domain forms a cluster below a Th/U ratio of 0.1. Both metamict zircon domains reflect a metamorphic event (or a fluid event, while the crust was still hot) postdating the emplacement of the Manic 5 Plutonic Suite.

Two other patterns in the U/Yb–Gd/Yb diagram are notable (Fig. 4.17b), depending on the crustal segment where the granitoid intruded. Concerning the three monzonite samples, the zircon of Manic 5 (mid-*P* segment) has higher U/Yb and Gd/Yb than those of Varin and Michaud (low-*P* segments). The Manic 5 "leucogranite" and the Bon-Désir granite are exceptions from this trend because of their different petrology and geochemistry. Moreover, trace-element variation is revealed in the cyclic CL pattern in the zircons of the Michaud monzonite (Fig. 4.13d). The dark-CL domain is U-rich and MREE-depleted relative to the bright-CL domain, and both domains have a similar age range. Collectively, the texture implies periodic recharge of a more evolved or crustal-derived melt in the magma chamber.

4.4.2.1. Ti-in-zircon thermometry and trace element oxybarometry

Using Ti-in-zircon temperature (TIZT) and the Ce–U–Ti oxybarometry (Ferry & Watson 2007; Loucks et al. 2020), the fO_2 (ΔFMQ)–*T* relationship of the zircons is displayed in Figure 4.18. To estimate the minimum *T*, αTiO_2=0.6 and αSiO_2=1 are taken for quartz-present, rutile-

absent granitoids in this study (Hayden & Watson 2007). *P*=6 kbar, calculated by the Al-in amphibole barometry (Section 4.2.1), is assumed to provide a conservative *T* estimation.

The Manic 5 monzonite has TIZT at 845–920ºC. The zircon crystallised under a more oxidising condition than the FMQ buffer (ΔFMQ−0.1 – +1.9). Furthermore, Manic 5 "leucogranite" has a fO_2 at FMQ at a TIZT of 812ºC. However, as the *P* of the protolith is unconstrained, a higher *P* effect will lead to a higher estimated *T* and a more reducing condition.

In the low-*P* segments, Varin monzonite has TIZT at 856–947ºC. The zircons crystallised under a more reduced condition (ΔFMQ−1.0 – 0). As the *P* may be overestimated, a lower *P* would yield an even lower fO_2, consistent with a reducing condition. All zircon domains of the Michaud monzonite crystallised at a wide range of *T* and have positive ΔFMQ, implying oxidising magma conditions. In particular, the high-U dark CL domain has a lower TIZT at 786–879ºC with ΔFMQ+0.6 to +1.6. Other domains have a higher *T* at 816–1114ºC with ΔFMQ+0.3 to +2.6. In the Bon-Désir granite, not many zircons have detectable Ti concentration, but the zircon crystallised at a *T* of 791–933ºC with a wide range of ΔFMQ (−1.5 – +3.5), suggesting the magma originated under variable redox conditions.

4.4.3. Lu–Hf isotopes

In-situ Lu–Hf isotopic analysis on zircon domains illuminates the potential sources of magma. Overall, each sample consists of a cluster of a single zircon population at the Grenvillian age, except Manic 5 "leucogranite". In these populations, no dispersion outside individual errors in the Lu–Hf data is observed. The Grenvillian zircons have a near-CHUR $\varepsilon_{Hf}(t)$ ranging from −1.9 to +4.3. Some analyses on inherited cores return variable $\varepsilon_{Hf}(t)$ at older crystallisation ages. The Lu–Hf isotope data are reported in Appendix F, and the results are displayed as ε_{Hf} versus crystallisation age in Figure 4.19.

In the Mid-*P* segment, Manic 5 monzonite and "leucogranite" gave contrasting results. The Manic 5 monzonite (04-445a) has the lowest range of $\varepsilon_{Hf}(t)$ among the analysed samples, with Grenvillian-age zircons having $\varepsilon_{Hf}(t)$ values from −1.9 to +0.8, clustering near the CHUR value. The T_{DM} ages of the zircons range between ~1710 Ma and 1850 Ma, suggesting that the Paleoproterozoic crust is an important magma source. This result is in agreement with the

Okaopéo Plutonic Suite (1015 ± 2 Ma) which possesses a similar isotopic composition with a T_{DM} at 1.9 Ma (Augland et al. 2015). Additionally, Manic 5 "leucogranite" (04-445b) has two age clusters with highly positive $\varepsilon_{Hf}(t)$ of similar values at +6.7 to +7.6. The oscillatory zoned domains that crystallised at ~1350 Ma yielded $\varepsilon_{Hf}(t)$ between +7.0 to +7.7. The igneous zircons are likely derived from a Pinwarian juvenile source younger than 1550 Ma. In addition, the Grenvillian-age metamict domains have ε_{Hf} at +7.0 to +7.9.

In the Low-*P* segments, Varin monzonite (22-AF-37) yielded a range of near-chondritic $\varepsilon_{Hf}(t)$. Although the age of the sample remains uncertain, between 1058–986 Ma (see Section 4.4.1), $\varepsilon_{Hf}(t)$ from 0 to +2.0 at 986 Ma provides a minimum estimation. Nevertheless, the T_{DM} ages of the zircons range between ~1710 Ma and 1550 Ma, suggesting the reworking of Labradorian or Pinwarian-age crust. In the ESB, Michaud monzonite and Bon-Désir granite have similar, positive $\varepsilon_{Hf}(t)$ at Grenvillian age. Michaud yields a range between +1.3 to +3.8 $\varepsilon_{Hf}(t)$ while Bon-Désir has a similar range from +1.7 to +3.8 $\varepsilon_{Hf}(t)$, corresponding to T_{DM} ranging between ~1710 Ma and 1550 Ma in the same array. A few xenocrysts are observed in both Michaud and Bon-Désir. In the Michaud monzonite, one Paleoproterozoic xenocryst (crystallisation age ~2000 Ma) with a T_{DM} at ~2500 Ma was discovered, indicating inheritance from the Paleoproterozoic crust. In the Bon-Désir granite, four xenocrysts with Pinwarian and Paleoproterozoic crystallisation ages have T_{DM} in the ranges of over 2500 Ma and ~2000–1900 Ma, indicating the inheritance from diverse Paleoproterozoic crustal sources.

4.5. Discussion

This section summarises the findings for each pluton regarding geochemical signatures and zircon data and discusses the crystallisation conditions (*P*, *T*, fO_2) and the possible magma sources.

4.5.1. Summary of geochemistry and ages of the five granitoids, and general insights

The following section summarises the main characteristics of the studied high-*T* granitoids in the central Grenville Province, from north to south.

4.5.1.1. Manic 5 monzonite and 'leucogranite'

The Manic 5 monzonite (1065 ± 8 Ma) is the dominant unit of the Manic 5 Plutonic Suite, exposed in the mid-*P* segment. The monzonite contains biotite, hornblende and allanite as minor phases, and crystallised at high-*T*. Geochemically, the sample is ferroan, metaluminous, alkali-calcic, and high-K. It has negative Nb–Ta–Ti anomalies, lacks Eu anomalies, and is weakly fractionated in terms of Nb/Ta while Zr/Hf is high. Less radiogenic (low ε_{Nd} and ε_{Hf}), Paleoproterozoic model ages (Nd T_{DM} ~1699 Ma; Hf T_{DM} ~1710–1850 Ma) as well as oxidising magma condition (positive ΔFMQ), suggest that the Manic 5 monzonite was generated from the partial melting of Paleoproterozoic crust. Additionally, a metamorphic age of 1026 ± 12 Ma was recorded by zircon metamict rims.

The monzonite unit also contains deca-metric rafts of "leucogranite" (1361 ± 11 Ma) with diffuse contacts. The "leucogranite" lacks mafic minerals except for rare biotite and is ferroan, weakly peraluminous and alkali-calcic. It is depleted in MREE and has negative Nb and Ti anomalies but is enriched in Ta; hence, it has very low Nb/Ta. On the Nb–Y plot, it falls into the VAG field. Unaltered, oscillatory-zoned zircons crystallised at ~1361 Ma, representing the crystallisation age of the felsic protolith. In addition, a metamorphic age of 1042 ± 3.7 Ma is recorded by zircon metamict rims. Hf enrichment (~3–4 wt% HfO_2), Nd T_{DM} at ~1275 Ma and high $\varepsilon_{Hf}(t)$ of the metamict zircon rims indicate possible fluid influence during metamorphism, which partially reset the isotopic systems (Kinny & Maas 2003). Hf in magmatic zircon domains remained relatively immobile. Based on the above, and together with the highly positive ε_{Hf} and Hf T_{DM} at ~1550 Ma, the Manic 5 "leucogranite" could be sourced from juvenile magma extracted from the mantle in the Mesoproterozoic. Therefore, the Manic 5 "leucogranite" is interpreted as a felsic orthogneiss of volcanic arc origin formed at the late stage of Pinwarian in Quebecia. During the Grenville Orogeny, the protolith was incorporated into the main Manic 5 pluton as large rafts and subjected to metamorphism.

In the Manicouagan Region, the Manic 5 Plutonic Suite is spatially associated with the Plus Value metasedimentary sequence which records monazite metamorphic ages between 1080 and 1060 Ma (Dunning & Indares 2010). Assuming coeval zircon recrystallisation and crystallisation of perthite in the "leucogranite" at 800ºC, Granulite-facies metamorphism is

coeval with the emplacement of the main, monzonitic unit of Manic 5 (04-445a) whereas metamorphic recrystallisation in 04-445a and 04-445b at 1042–1035 Ma may indicate a younger metamorphic pulse.

4.5.1.2. Varin monzonite

The Varin monzonite is exposed in the Baie-Comeau region of the low-*P* (granulite) segments. The investigated sample (986 ± 19 Ma) contains rapakivi feldspars as well as minor biotite, hornblende and allanite and, crystallised at high-*T*. Geochemically, it is ferroan, weakly peraluminous, alkalic and high-K. It has negative Nb–Ta–Ti anomalies and positive Eu anomalies and has slightly fractionated Nb/Ta but high Zr/Hf. Homogeneous zircon and the absence of inherited zircon are consistent with a mantle origin. The Labradorian Hf T_{DM} and Nd T_{DM} (1538–1534 Ma) and reducing magma condition (negative ΔFMQ) suggest that the Varin monzonite was generated from the partial melting of a lithospheric mantle source with subsequent crustal assimilation.

4.5.1.3. Michaud Monzonite

The Michaud Monzonite (1063 ± 3 Ma) is a pluton exposed in a shear zone at the northern boundary of the ESB low-*P* segment. The monzonite contains minor biotite and amphibole and is high-K, ferroan, metaluminous and alkali-calcic. Negative Nb–Ta–Ti anomalies, no negative Eu anomalies, enrichment of LILE and the Paleoproterozoic inherited zircons with positive ε_{Hf} collectively suggest a significant crustal influence. The +1.3 to +3.8 $\varepsilon_{Hf}(t)$ and Labradorian Hf T_{DM} could be a mixed age of Pinwarian-age and older Paleoproterozoic crust. The oxidising character of the magma (positive ΔFMQ) and cyclic high-U domains in zircons are consistent with periodic melt recharge from a U-rich crustal source. Overall, Michaud Monzonite could be generated from the partial melting of older arc crust.

4.5.1.4. Bon-Désir Granite

The Bon-Désir Granite (1086 ± 2 Ma), outcropping in the southern part of the ESB, is the oldest pluton in the study region. The granite contains minor biotite and rare monazite and is high-K, magnesian, alkali-calcic, and weakly peraluminous. It is characterised by negative Nb–Ta–Ti anomalies, negative Eu anomalies and slightly fractionated Nb/Ta and Zr/Hf ratios.

Enrichment of LFSE and the presence of inherited zircons from ~1.8 Ga and ~1.4 Ga with negative ε_{Hf} suggests a prominent crustal source. The Nd T_{DM} at 1517 Ma coincides with the host rock age of the ESB (Groulier et al. 2018a), both oxidising and reducing magmas (variable ΔFMQ) suggest that Bon-Désir Granite was generated by the hybridisation of crustal and mantle magma sources.

4.5.2. Melt crystallisation P, T, fO_2 and links to the crustal levels of intrusion

The *P* and *T* were estimated by various petrological tools for the samples, and a summary is reported in Table 4.6. This section comments on the validity of the data and the petrogenetic implications of the results.

An uncertainty could arise from the *P* estimation of the Al-in-amphibole barometer because low fO_2 and atypical X_{Mg} could lead to an overestimated *P* (Anderson & Smith 1995). The *P* of Varin monzonite, for example, could also be overestimated due to fO_2 below the FMQ buffer. Although the uncertainties may propagate into *P*-dependent thermometers, the estimated *T* is still in the high-*T* regime (Miller et al. 2003), consistent with the petrography and zircon textures.

Four thermometers were applied based on whole-rock geochemistry and mineral chemistry of amphibole, feldspar and zircon, all producing mutually consistent results, with estimated high-*T* conditions from at least 800 up to 1000ºC. For T_{Zr}, Zr is saturated in the magma at a similar liquidus *T* as ternary feldspars, suggesting zircon and feldspars crystallised at a similar *T*. Although in rapakivi granitoids, the plagioclase-amphibole temperature may be overestimated (Anderson et al. 2008), the ternary feldspar temperature, T_{Zr} and TIZT comprise a considerable range in the Varin monzonite. The TIZT in all samples is about 50ºC lower than the other three thermometers, but it is still in the high-*T* regime. Exceptions include xenocrystic zircons in the Bon-Désir granite that crystallised at a slightly lower *T* and the high-U dark CL zone in the Michaud monzonite, which could correspond to the addition of a more evolved melt at a lower *T*.

Integrating the intensive parameters, the investigated granitoid samples appear to have crystallised at a high-*T* of 800–1000ºC at a *P* of 5–6 kbars, e.g., at 15–20 km deep in the middle

crust. In the Manicouagan region, the estimated *P–T* condition of coeval granulite-facies metamorphism is ~9–11 kbar at ~820–900ºC at ~1080–1060 Ma (Indares & Dunning 2018). The Manic 5 monzonite crystallised at a similar *T* range but at a lower *P*. A high heat flux is required to foster partial melting of the middle crust.

Table 4.6 Summary of estimated crystallisation *P* and *T*.

Plutonic Suites/Units	Al-in-Amp *P* (kbar)[1]	Plag-Amp *T* (ºC)[1]	Ternary Feldspar *T* (ºC)[2]	Zircon saturation *T* (T_{Zr} ºC)[3]	Ti-in-zircon Thermometry (TIZT)[4]			
					CL domains[5]	n	mean (ºC)	range (ºC)
Manic 5 monzonite 04-445a	6.0 – 6.1	947 – 968	~800 – 1000	958	SZ/H	7	876	845 – 920
Manic 5 "leucogranite" 04-445b	-	-	~800 – 850	-	oscillatory	2	812	-
Varin monzonite 22-AF-37	6.4 – 7.0	949 – 975#	~900 – 1000	1000	SZ/H	12	900	856 – 947
Michaud monzonite 15-PA-187A	5.2 – 5.5	812 – 848	~700 (A)	927 – 940	dark-CL domain	4	815	786 – 879
			~1000 (P)		Other domains	32	900	816 – 1114
Bon-Désir granite 15-PA-107A	-	-	~1000 (A)	-	SZ/H	5	869	791 – 930
			< 600 (P)		Inherited	4	885	825 – 933

[1] See Table 4.2 for details.
[2] See Table 4.3 for details. Abbreviations: A – antiperthite; P – perthite.
Plag-Amp *T* could be underestimated due to chemical disequilibria in rapakivi granites (Anderson & Smith, 1995).
[3] Watson and Harrison (1983);
[4] Ferry and Watson (2007). αTiO_2 taken as 0.6 and αSiO_2 as 1 for minimum *T* estimation in rutile-absent melt (Hayden & Watson, 2007). Pressure at 6 kbar also provides a conservative *T* estimate.
[5] Abbreviations: SZ – sector-zoned; H – homogeneous.

4.5.3. Sources of magma

The whole-rock Sm–Nd and zircon Lu–Hf isotopes of the granitoids, except for Manic 5 "leucogranite", are signatures of reworked crust. The Grenvillian-age granitoids are less radiogenic than juvenile melts in both isotopic systems. Their whole-rock Sm–Nd evolution overlaps with the isotopic evolution of the Quebecia arc crust, consistent with an input of melt derived from the partial melting of the crust (Fig. 4.11). On the other hand, the zircon ε_{Hf} in these samples (~−1.9 to +3.8) with comparable model ages is in agreement with the whole-rock Sm–Nd isotopes, representing reworking of Paleo- to Mesoproterozoic crustal components. Inherited zircons in the Bon-Désir granite also imply their derivation from reworked Paleoproterozoic

material derived from the Laurentian margin. In the case of magma hybridisation, a much older crustal source would be required to combine with juvenile mafic magma extracted from the depleted mantle, so the presence of a juvenile mantle-derived melt during the Grenvillian Orogeny is unlikely. Such a finding concurs with Nd mapping of Quebecia crust with Labradorian to Pinwarian T_{DM} ages (Vautour & Dickin 2019; Dickin et al. 2023) and whole-rock Hf T_{DM} at ~1.9 Ga in the Okaopéo Mangerite in the mid-*P* segment (Fig. 4.19; Augland et al. 2015). Moreover, the geochemistry of the granitoids also suggests that the precursor crust was likely formed in an arc setting (negative Nb–Ta–Ti anomalies), which is consistent with the regional geological constraints that suggest the Pinwarian and Labradorian crust is an important source of magma across the central Grenville Province. Therefore, the reworked crust is an important source of the orogenic high-*T* granitoids in the central Grenville Province.

In addition, the lithospheric mantle could have played an important role in the production of the high-*T* granitoids. The granitoids containing mafic enclaves, being ferroan and metaluminous, crystallising at high solidus *T*, and a lack of inherited zircon, collectively suggest the involvement of mafic magma in their petrogenesis. High LILE, such as Ba and Sr, also reflect a magma derived from the partial melting of lithospheric mantle. A metasomatised lithospheric mantle generates potassic, alkaline magmatism, enriched incompatible elements including LILE and HFSE, unfractionated HFSE canonical pairs, depleted Nb–Ta–Ti, and oxidising fO_2, all of which suggest an enriched mantle source. Multiple accretionary orogenic events before the Grenville Orogeny (~1.7–1.2 Ga) could have modified the composition of the lithospheric mantle.

Hybridisation of magma is observed on the mineralogical, field and regional scale. In single crystals, periodic U-rich melt recharge is observed in the zircons of the Michaud monzonite. At the field scale, the commingling of mafic magma with the intermediate-felsic host and xenoliths of Pinwarian age orthogneiss in the Manic 5 monzonite highlights the mixed, heterogeneous nature. Across the region, the plutons vary from crustal-dominant granites, such as monazite-bearing Bon-Désir Granite and amazonite-bearing Astra Granite (Higgins et al. 2002), to alkaline associations, such as Pipmuacan and Trémaudan Plutonic Suites (Hébert et al. 2009).

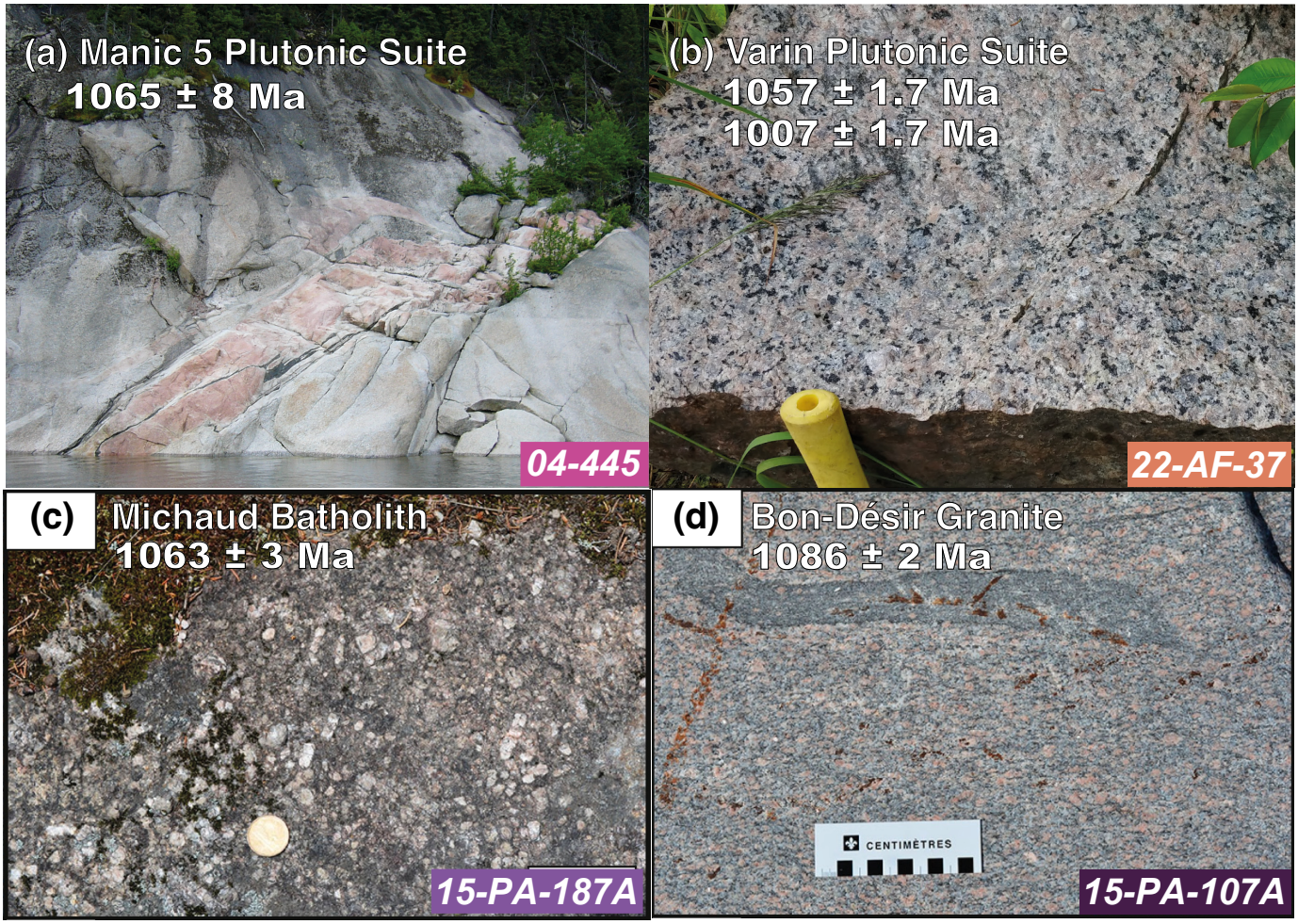

Figure 4.1 Photographs of the sampled outcrops. (a) Manic 5 Plutonic Suite 04-445a (grey) and 04-445b (pink), modified from Dunning and Indares (2010). **(b)** 22-AF-37 of the Varin Plutonic Suite (Courtesy of Arlin Fonseca). **(c)** 15-PA-187A of Michaud Monzonite, modified from Groulier et al. (2018a). **(d)** 15-PA-107A of Bon-Désir Granite, modified from Groulier et al. (2018a).

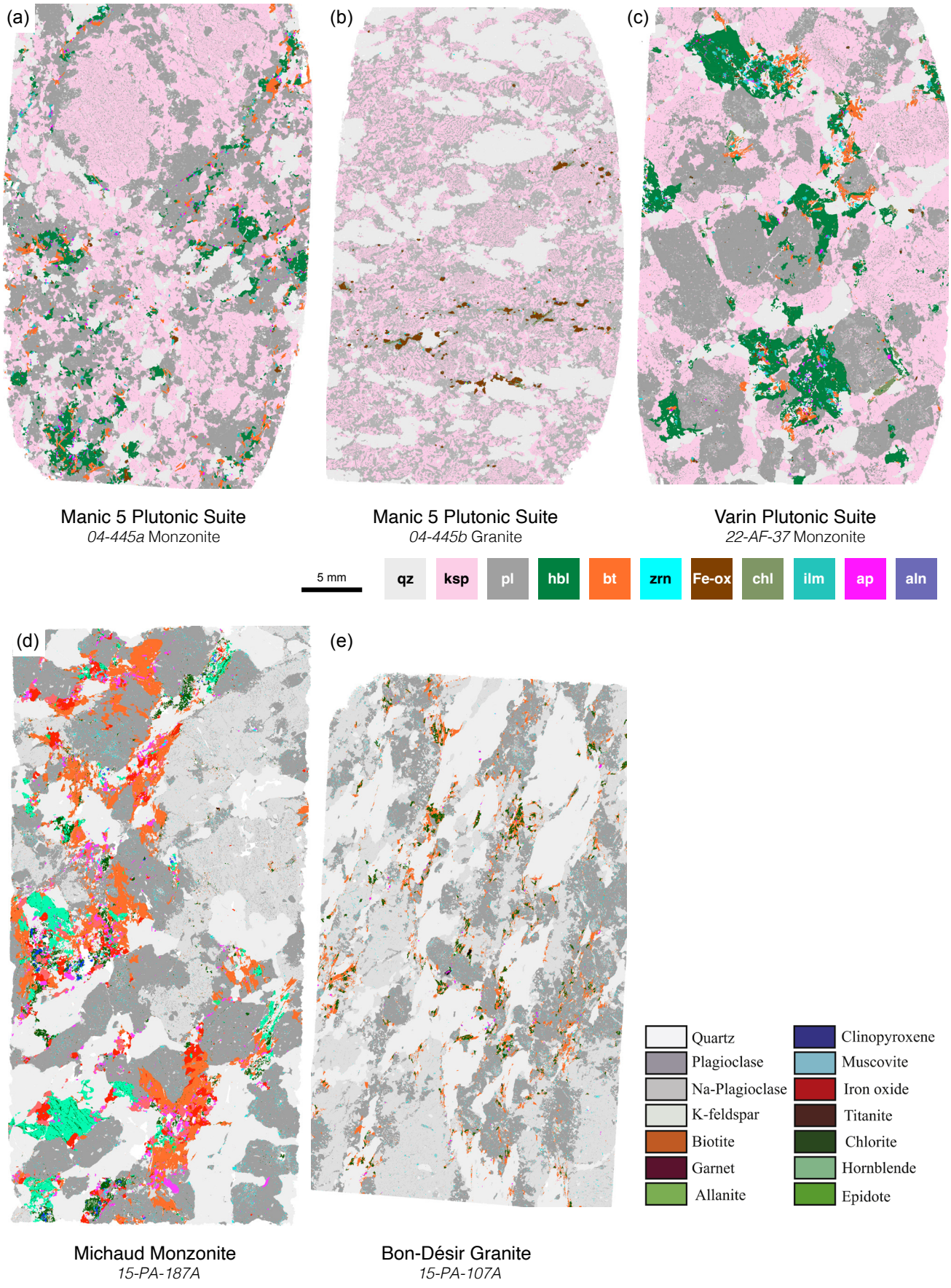

Figure 4.2 SEM–MLA false colour maps of thin sections, showing the distribution of minerals. This study: **(a)** 04-445a, **(b)** 04-445b, **(c)** 22-AF-37, Modified from Groulier et al. (2018a): **(d)** 15-PA-187A, and **(e)** 15-PA-107A.

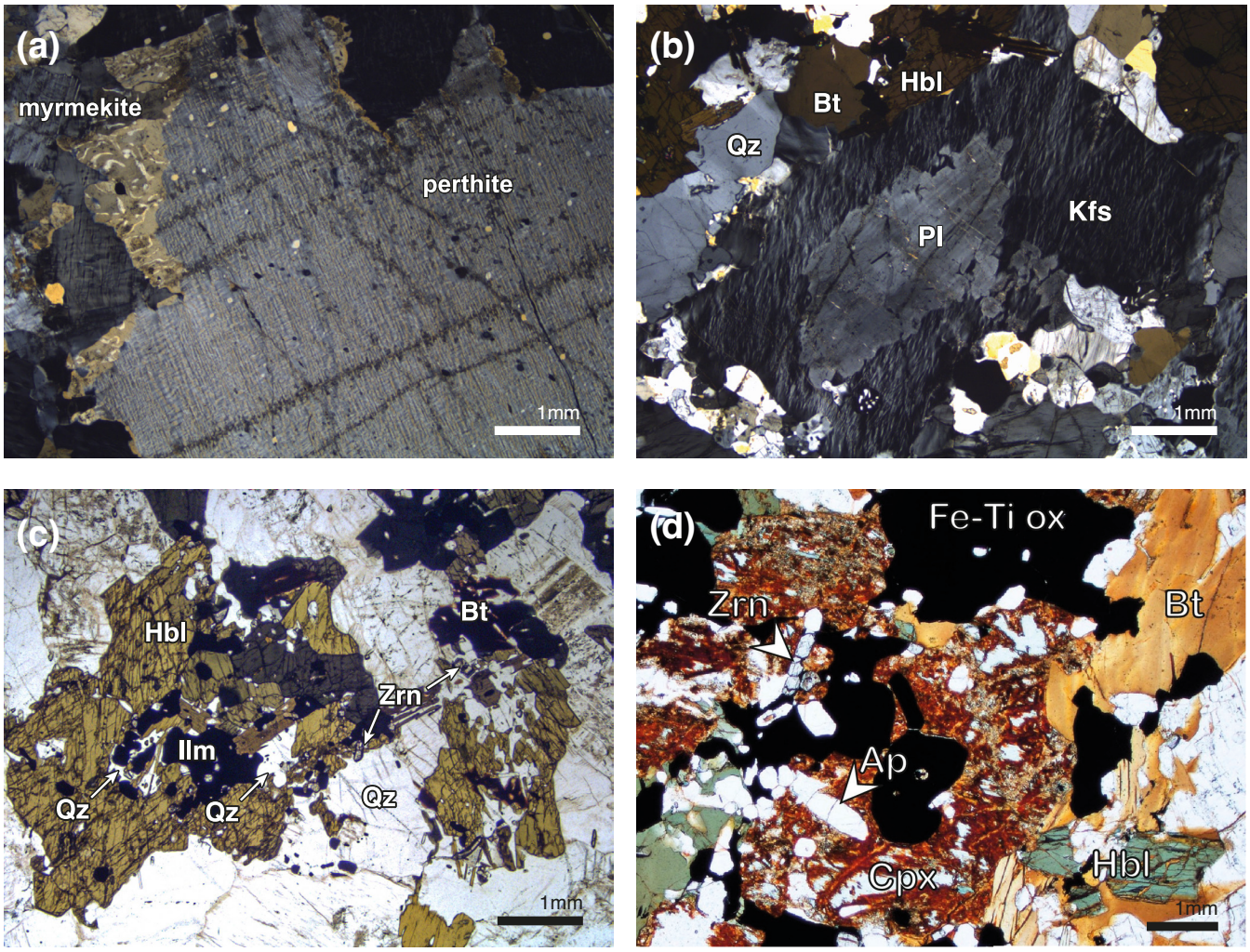

Figure 4.3 Photomicrographs of the samples. **(a)** Manic 5 monzonite (04-445a), myrmekite and perthite, XPL. Varin monzonite (22-AF-37), **(b)** anti-rapakivi texture showing K-feldspar mantling plagioclase, XPL, and **(c)** melt pockets containing poikilitic hornblende (pargasite), quartz, ilmenite, biotite and zircon, PPL. **(d)** Michaud monzonite **(**15-PA-187A), clusters of ferromagnesian and trace minerals, PPL, modified after Groulier et al. (2018a).

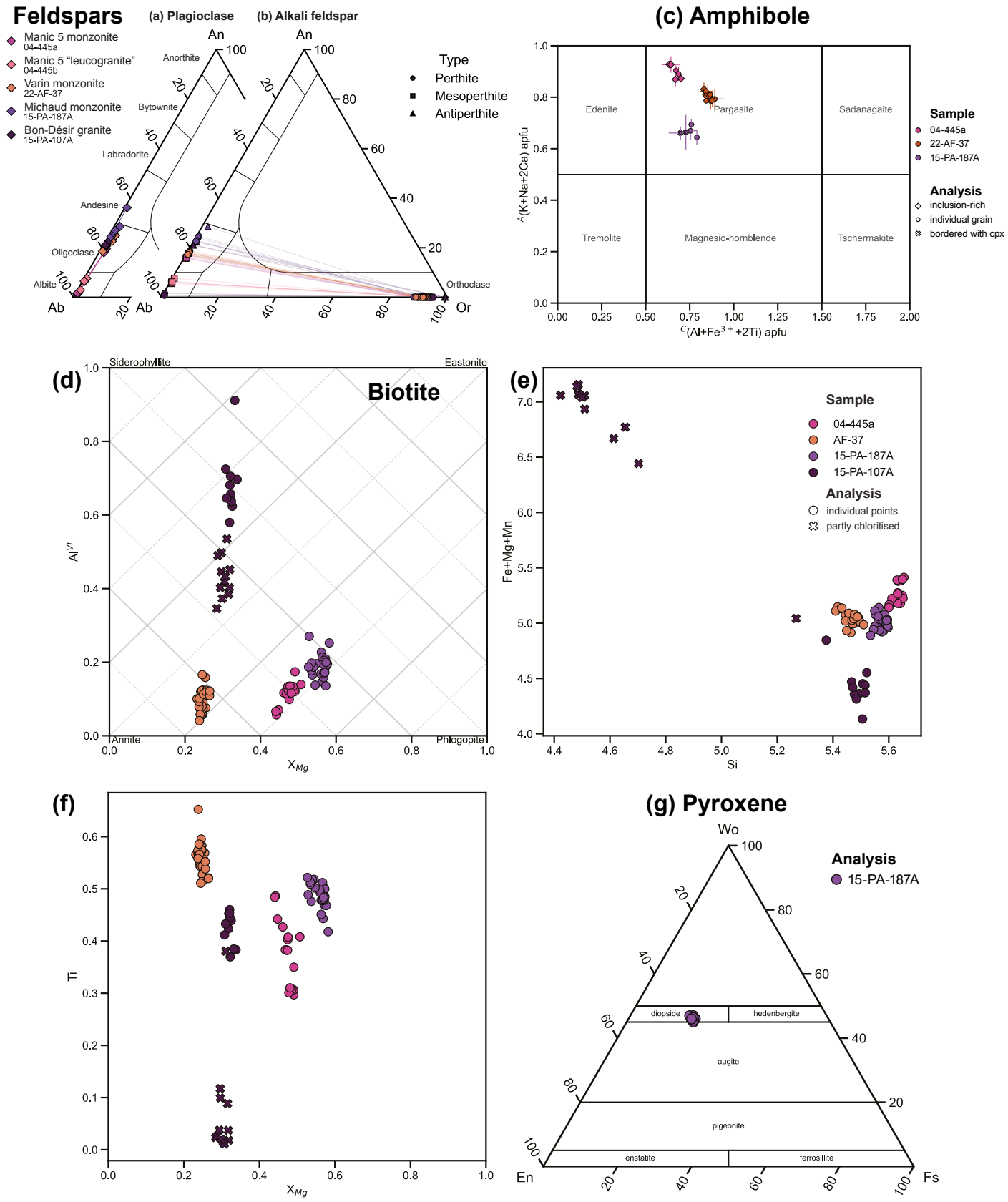

Figure 4.4 Mineral chemistry. **(a)** Plagioclase and **(b)** alkali feldspar (hosts and lamellae) compositions. **(c)** Calcic amphibole classification (Hawthorne et al. 2012). **(d)** Biotite nomenclature (Rieder et al., 1998), **(e)** (Fe+Mg+Mn)–Si showing alteration and **(f)** Ti–X_{Mg} plot. **(g)** Pyroxene composition in 15-PA-187A.

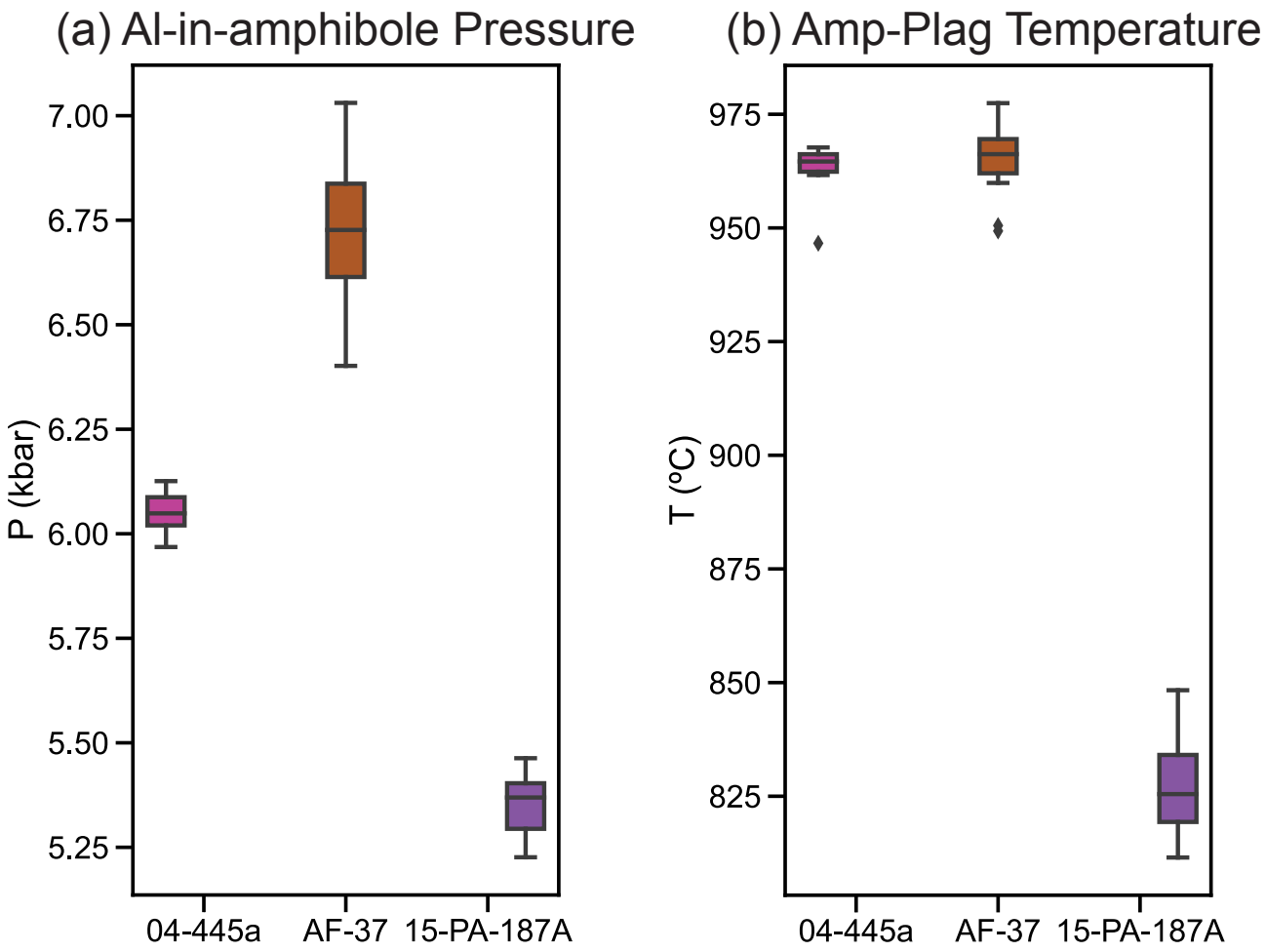

Figure 4.5 Thermobarometry results for Manic 5 (04-445a), Varin (22-AF-37) and Michaud monzonite (15-PA-187A). **(a)** *P* conditions are estimated by Al-in-amphibole barometry (Anderson & Smith 1995) and **(b)** *T* conditions amphibole-plagioclase thermometry (Holland & Blundy 1994).

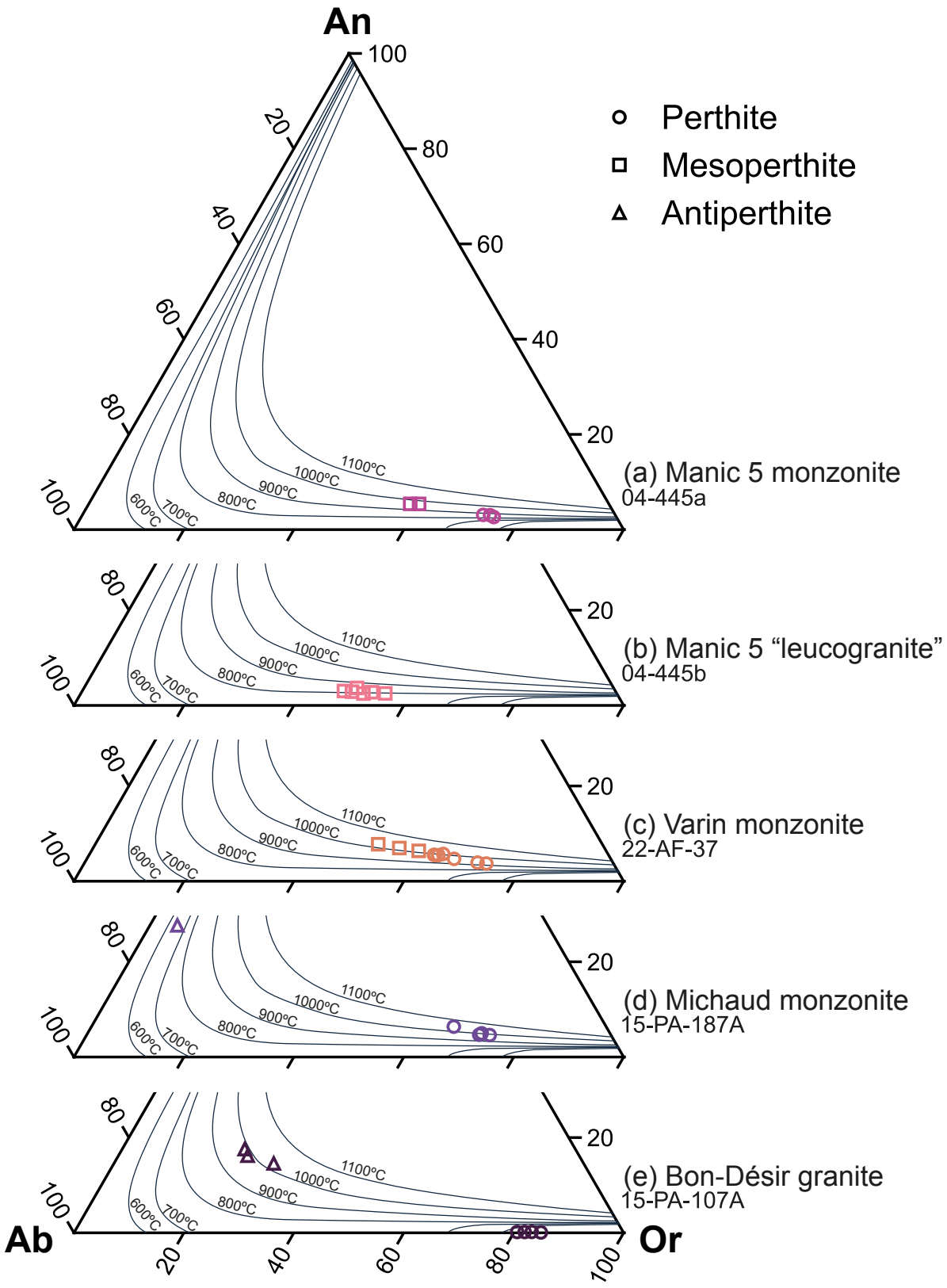

Figure 4.6 *T* results obtained by ternary feldspar thermometry. Ternary feldspar re-integrated compositions after Hokada (2001). Isotherms of thermodynamic models of ternary feldspars at 5 kbars are shown (Elkin & Grove 1990).

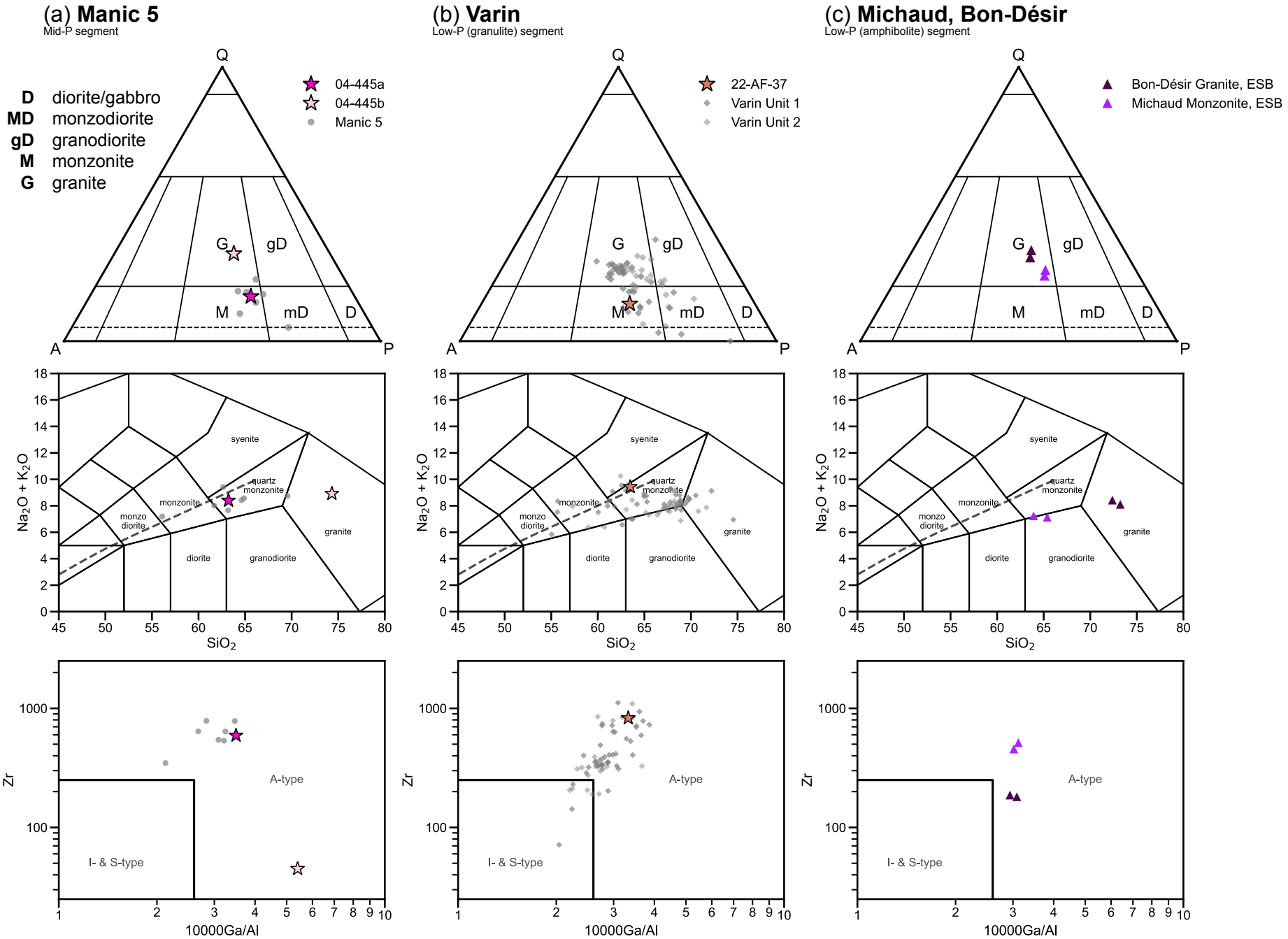

Figure 4.7 Granitoid classification for **(a)** Manic 5 Plutonic Suite, **(b)** Varin Plutonic Suite and **(c)** Michaud and Bon-Désir. *Row 1* QAP (Streckeisen 1976), *Row 2* TAS diagram (Middlemost 1994) and *Row 3* Zr–Ga/Al (Whalen et al. 1987). Data in grey are those from the literature for comparison.

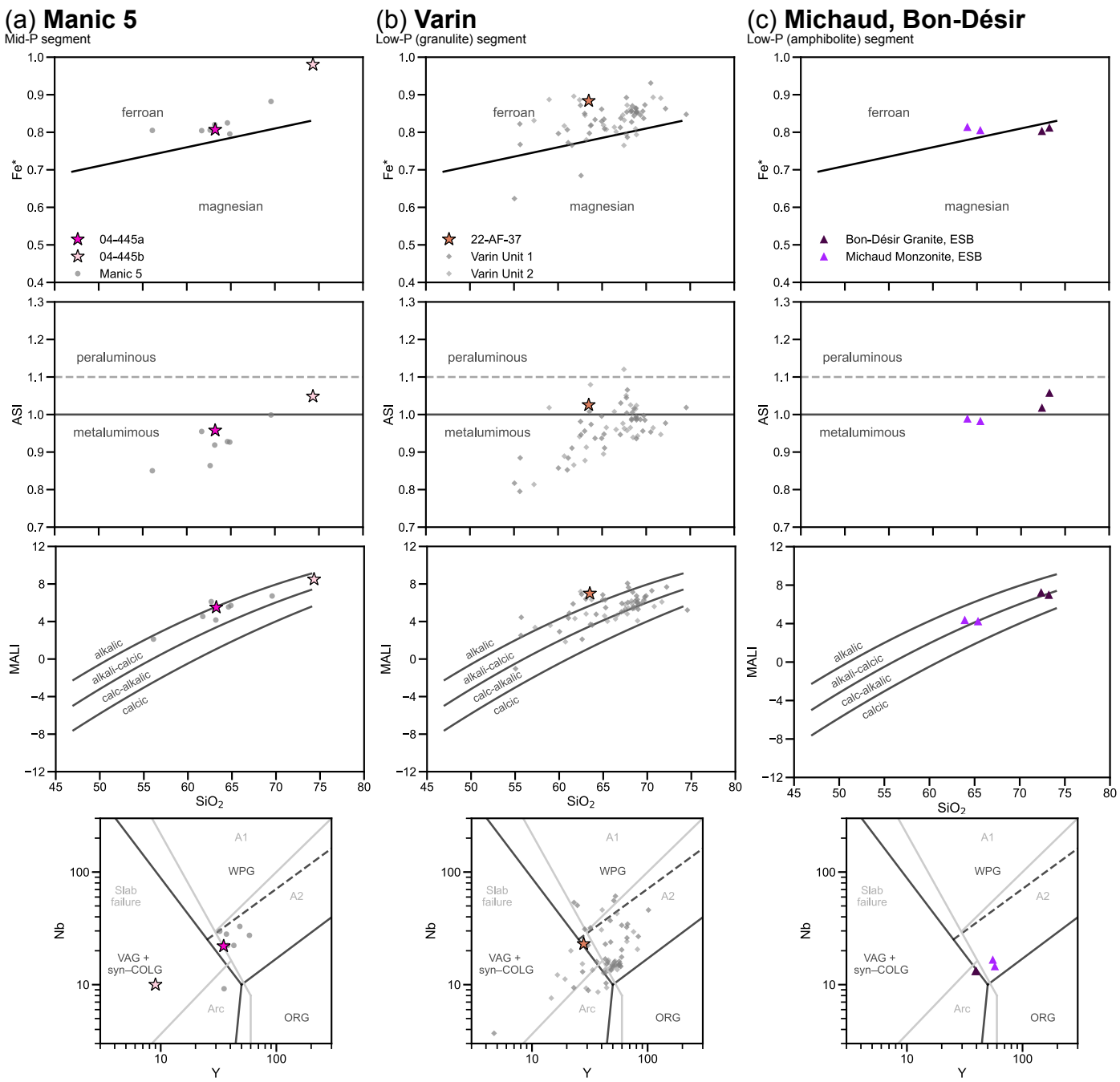

Figure 4.8 Granitoid classifications (continued) for **(a)** Manic 5 Plutonic Suite, **(b)** Varin Plutonic Suite and **(c)** Michaud and Bon-Désir. Row 1–3 Fe*, ASI, MALI– SiO_2 (Frost et al. 2001), and Row 4 Nb–Y diagram (Pearce et al. 1984; Whalen & Hildebrand 2019). Data in grey are those from the literature for comparison.

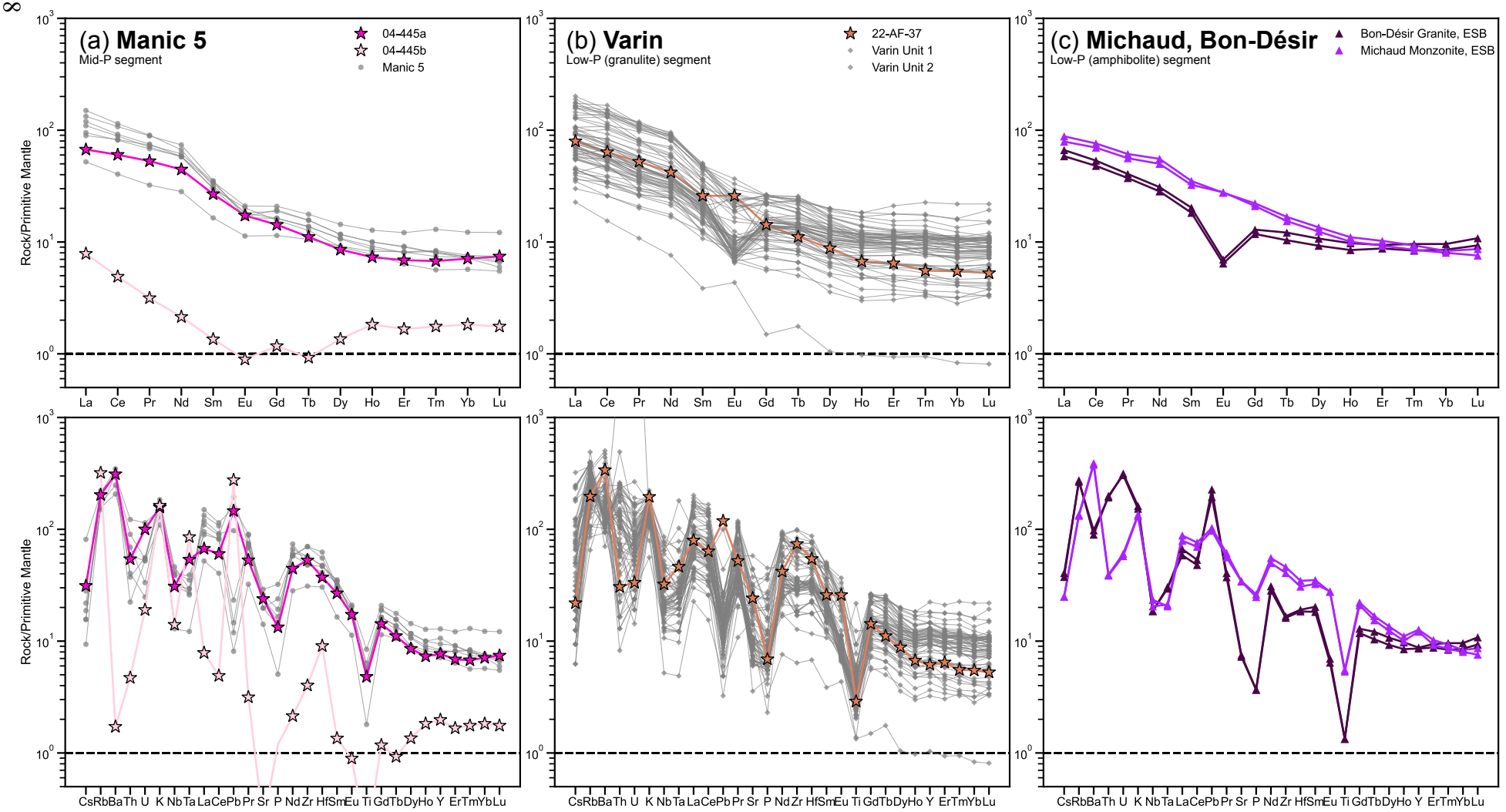

Figure 4.9 PM-normalised REE and extended trace element diagrams of granitoid samples for **(a)** Manic 5 Plutonic Suite, **(b)** Varin Plutonic Suite and **(c)** Michaud Monzonite and Bon-Désir Granite. Data in grey are those from the literature for comparison.

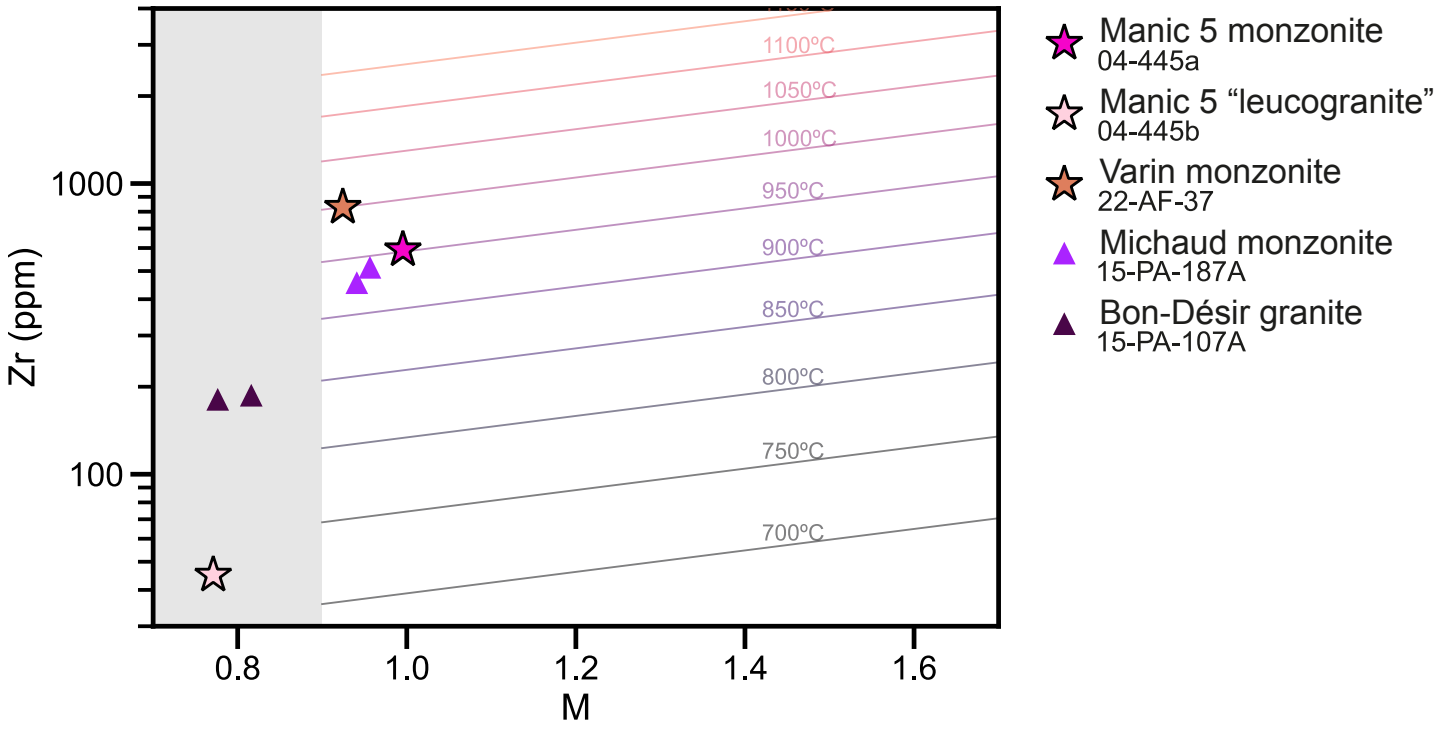

Figure 4.10 Zircon saturation temperature (T_{Zr}, Watson & Harrison 1983) of the studied samples. The data falling into the uncalibrated region (shaded) are considered invalid.

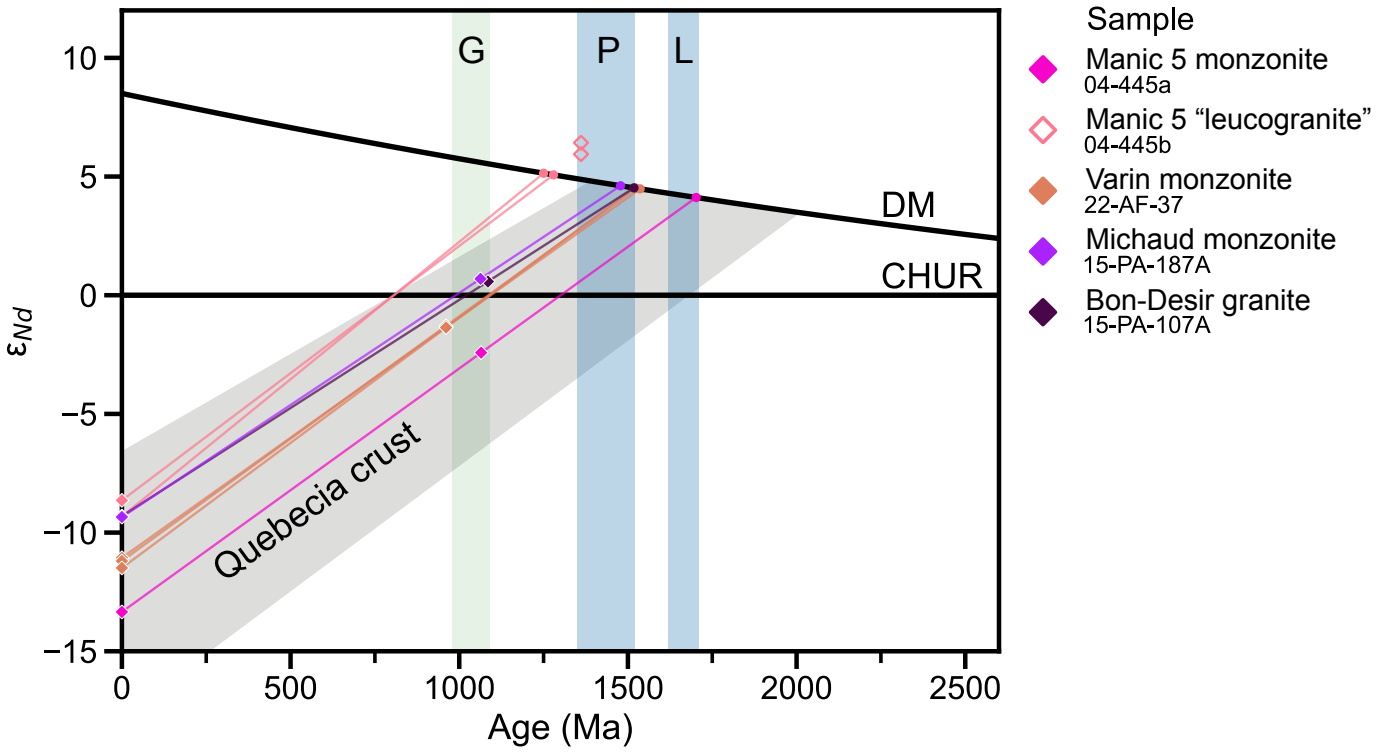

Figure 4.11 $\varepsilon_{Nd}(t)$ vs age diagram of the high-*T* granitoids. Data from the ESB (Sample No. 15-PA-107A and 15-PA-187A) are from Groulier et al. (2018a). Grey region represents the average evolution of Quebecia crust (Dickin 2000; Dickin & Higgins 1992; Vautour & Dickin 2019). Orogenic periods, G: Grenvillian; P: Pinwarian; L: Labradorian. Depleted mantle (DM) evolution curve from DePaolo (1981).

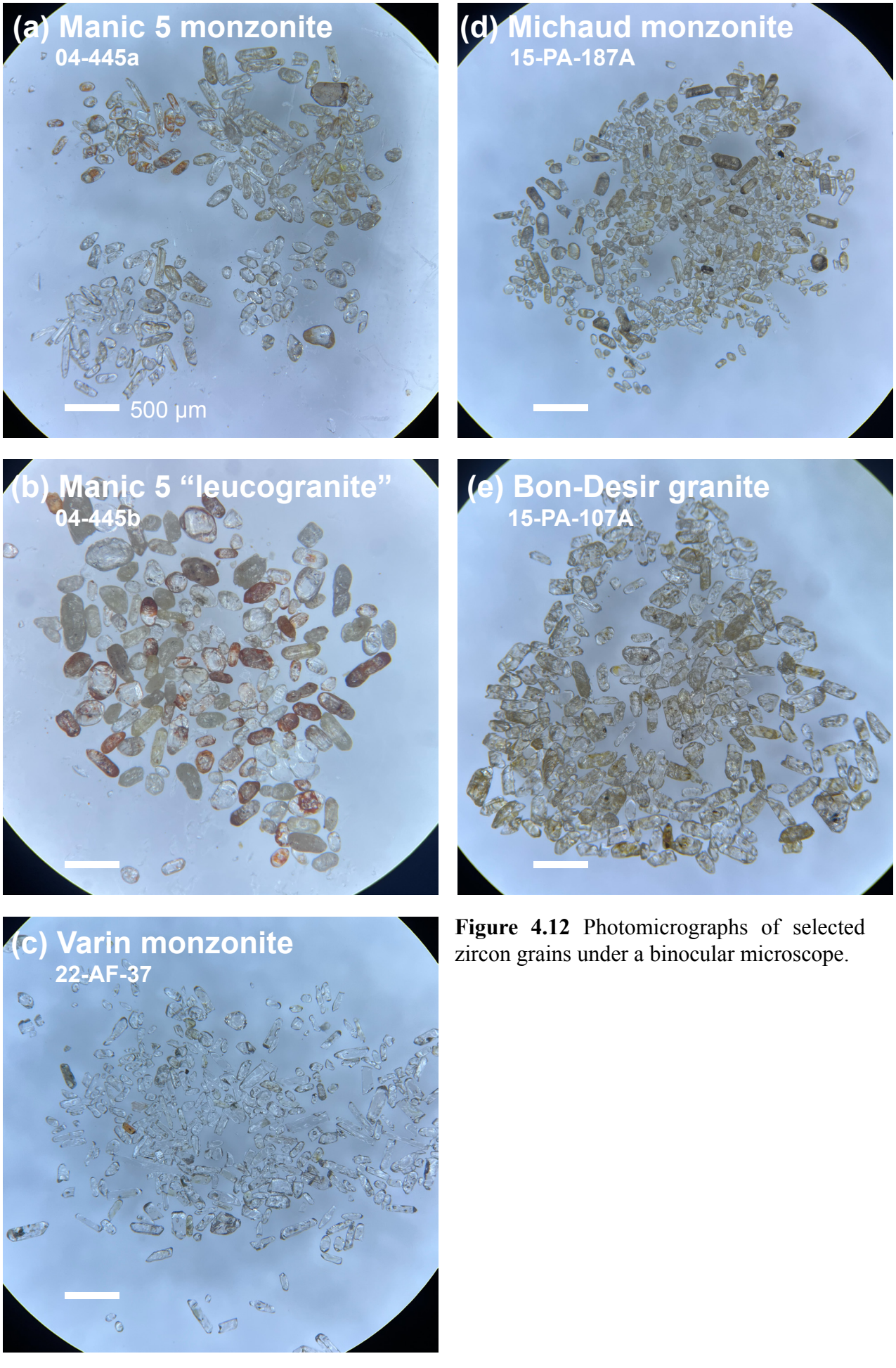

Figure 4.12 Photomicrographs of selected zircon grains under a binocular microscope.

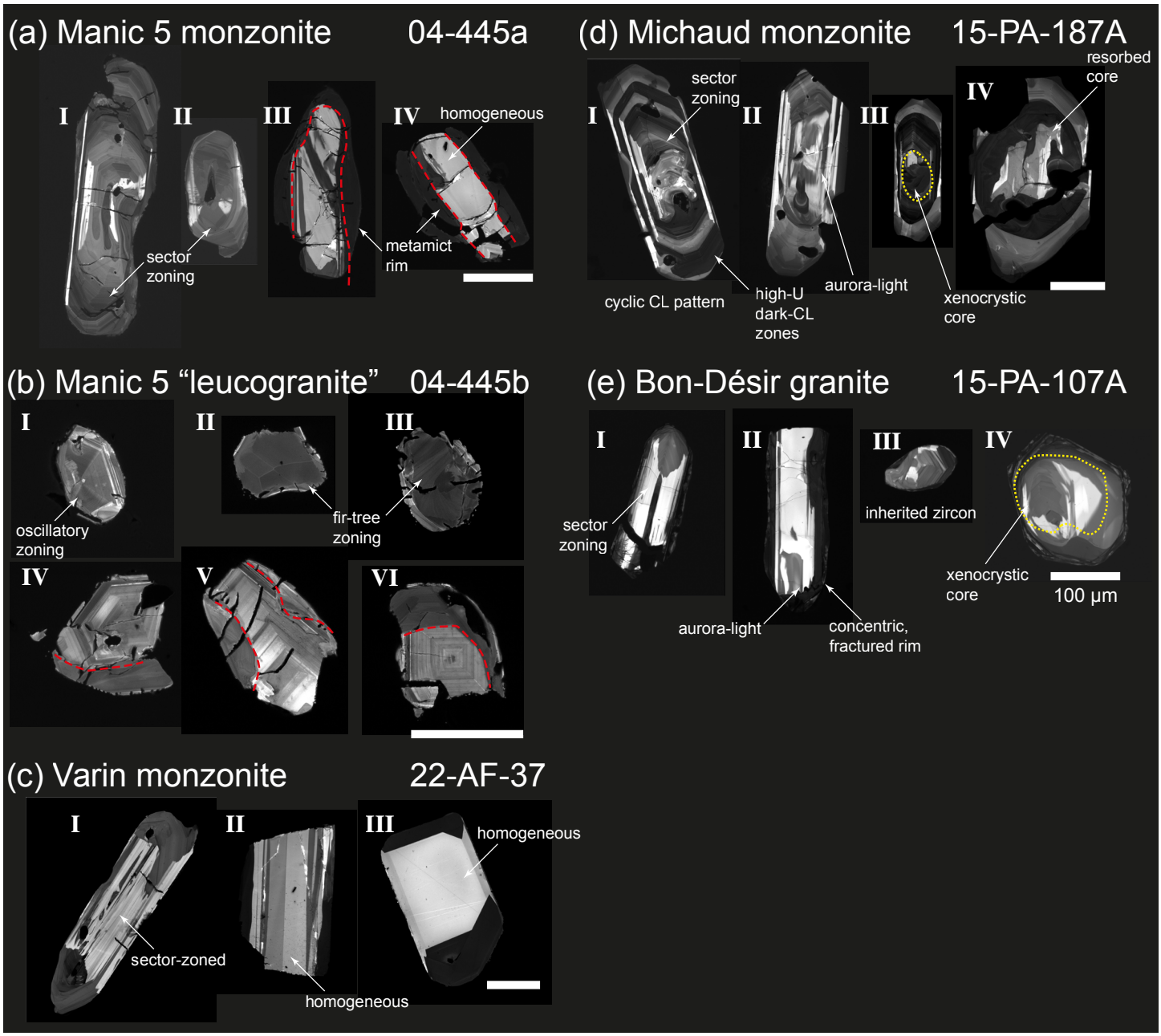

Figure 4.13 Representative zircon CL images. Scale bars are 100 µm long in each sample. Red dashed lines: boundary of different domains. Yellow dash: inherited cores.

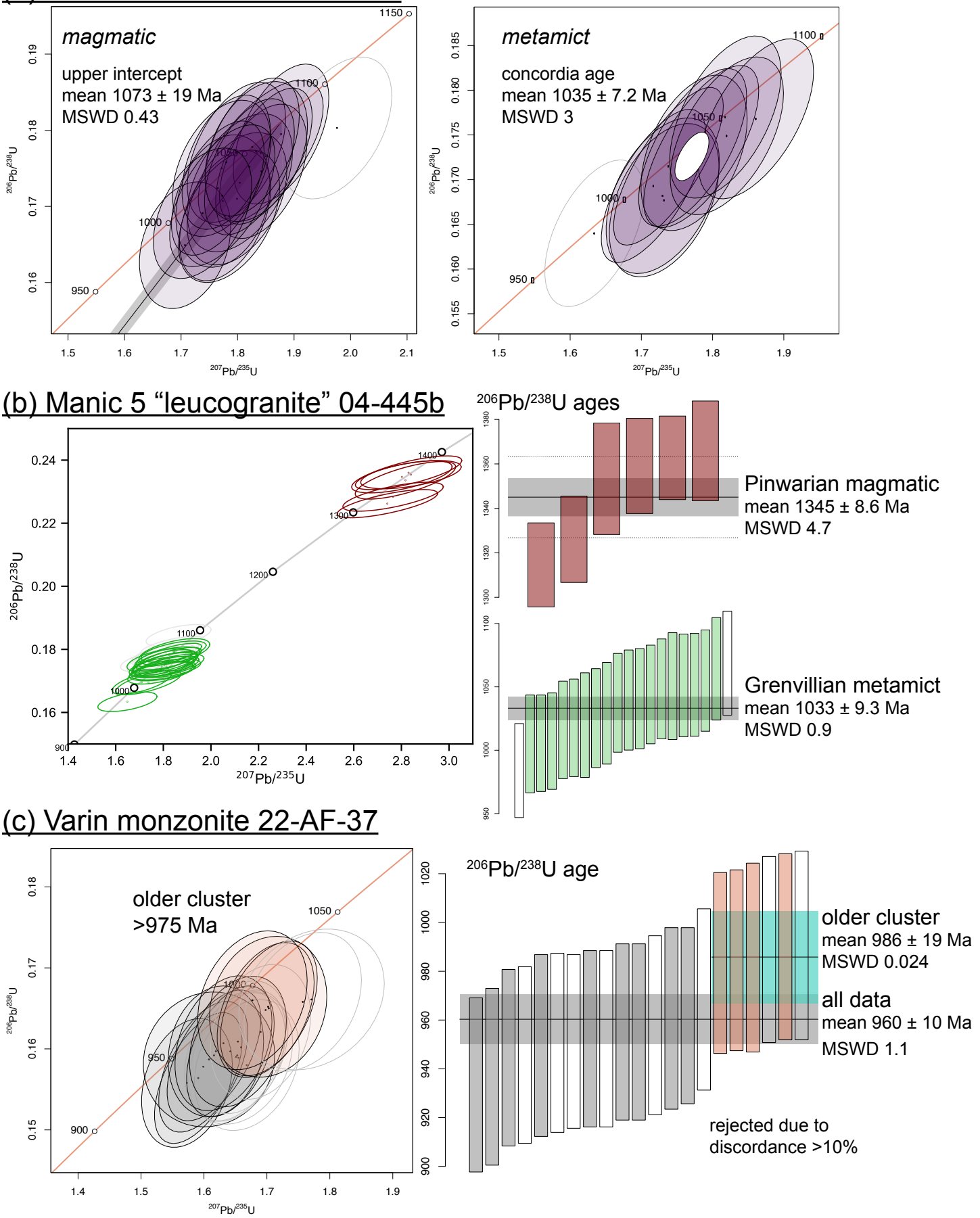

Figure 4.14 LA–ICP–MS zircon U–Pb concordia diagrams and weighted average $^{206}Pb/^{238}U$ ages of **(a)** Manic 5 monzonite and **(b)** "leucogranite", and **(c)** Varin monzonite.

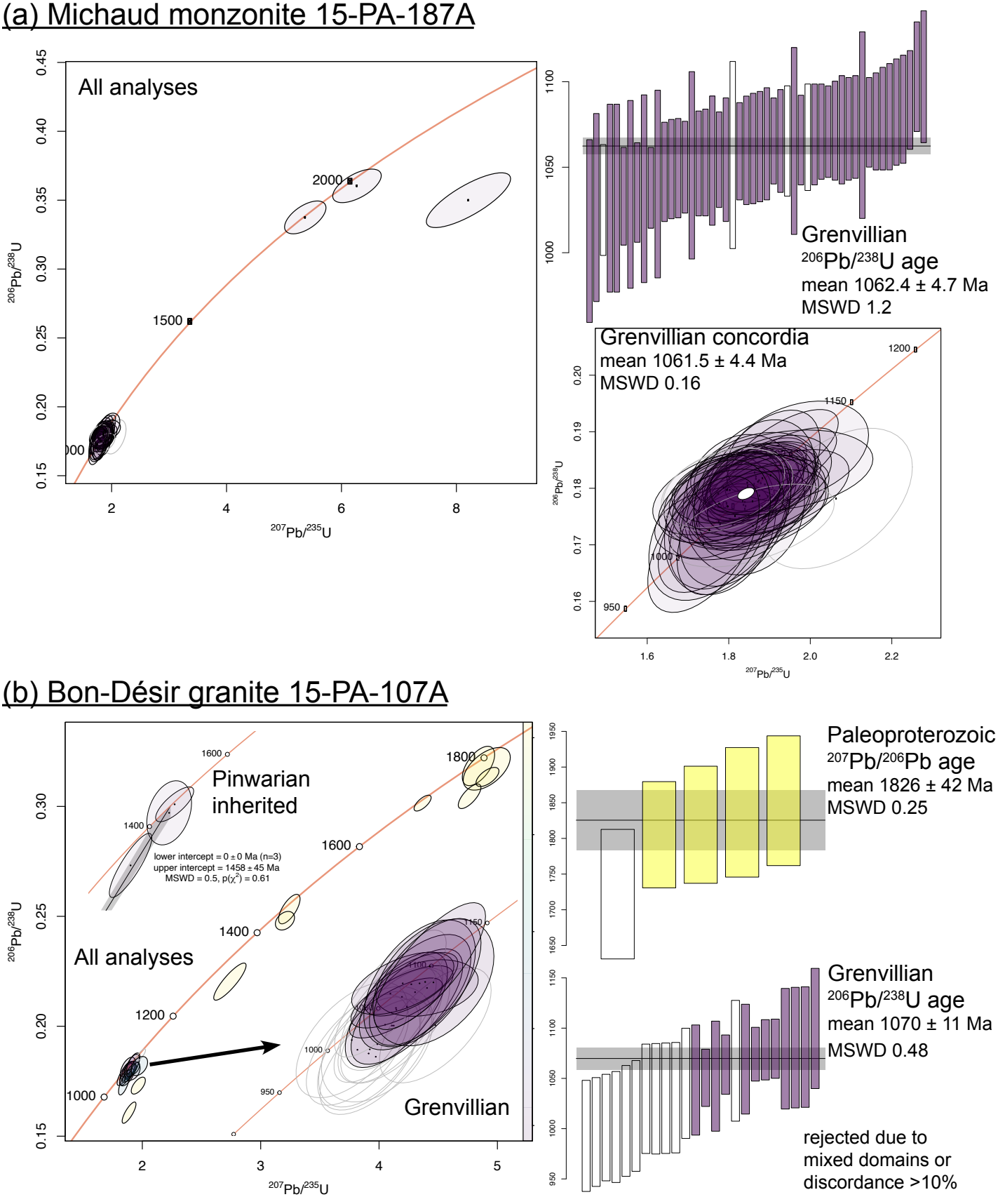

Figure 4.15 LA–ICP–MS zircon U–Pb concordia diagrams and weighted average $^{206}Pb/^{238}U$ ages of **(a)** Michaud monzonite and **(b)** Bon-Désir granite.

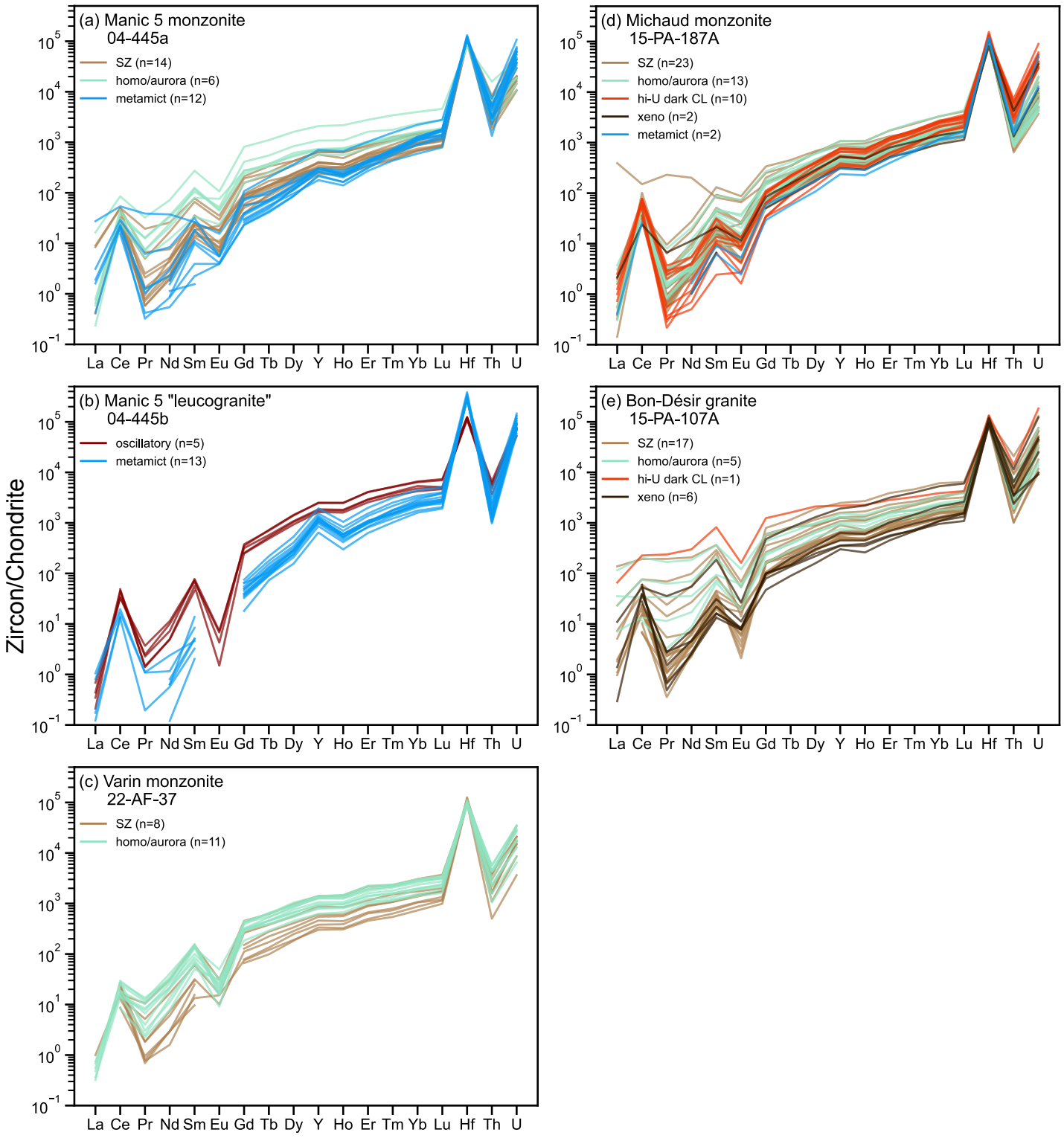

Figure 4.16 Zircon chondrite-normalised trace element diagrams (McDonough and Sun, 1995).

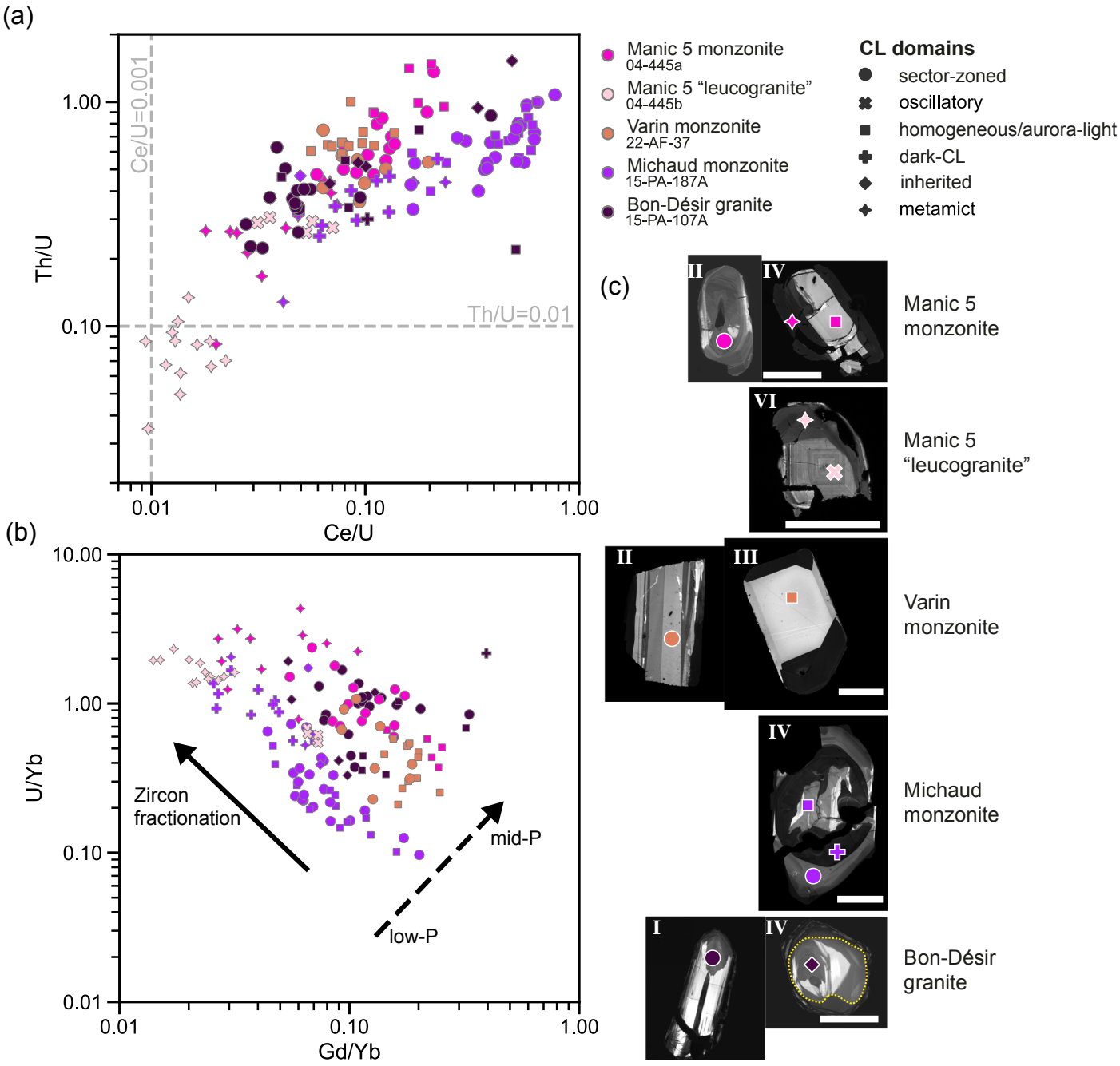

Figure 4.17 Zircon trace element diagrams. **(a)** Th/U–Ce/U distinguishing magmatic and metamict domains (Roberts et al. 2024). CHUR values (grey dashed lines) after McDonough and Sun (1995). **(b)** U/Yb–Gd/Yb (Grimes et al. 2015) with representative CL images showing textural relationships. (c) Graphical legend showing the domains and symbol relationship.

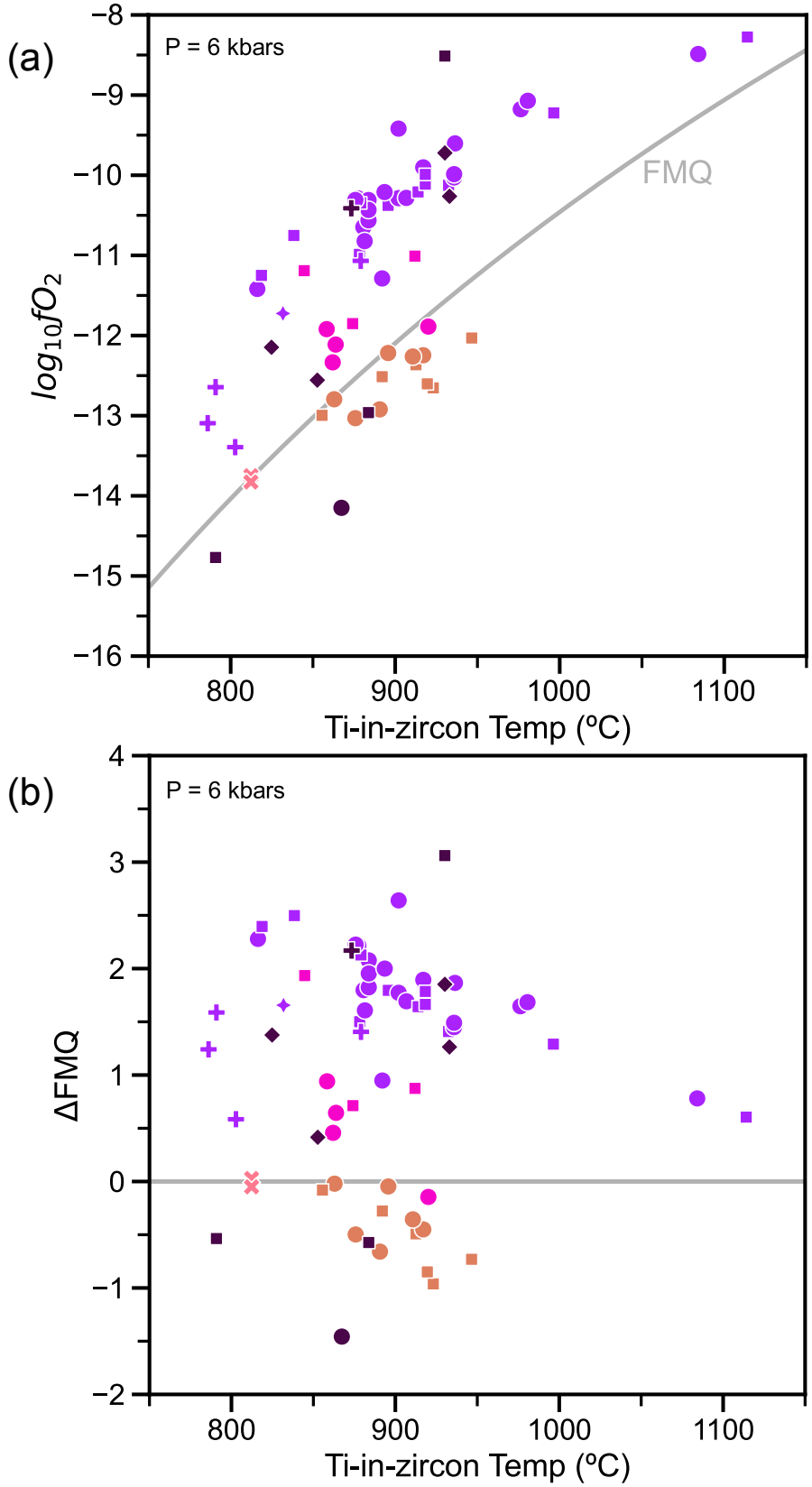

Figure 4.18 fO_2–TIZT at 6 kbars by zircon Ce–U–Ti oxybarometry and Ti-in-zircon thermometry (Loucks et al. 2020). **(a)** $\log_{10}fO_2$–TIZT diagram. Grey line: FMQ buffer (Frost 1991). **(b)** ΔFMQ–TIZT diagram, showing fO_2 with respect to the FMQ buffer. Symbol as in refers to **Fig. 4.17**.

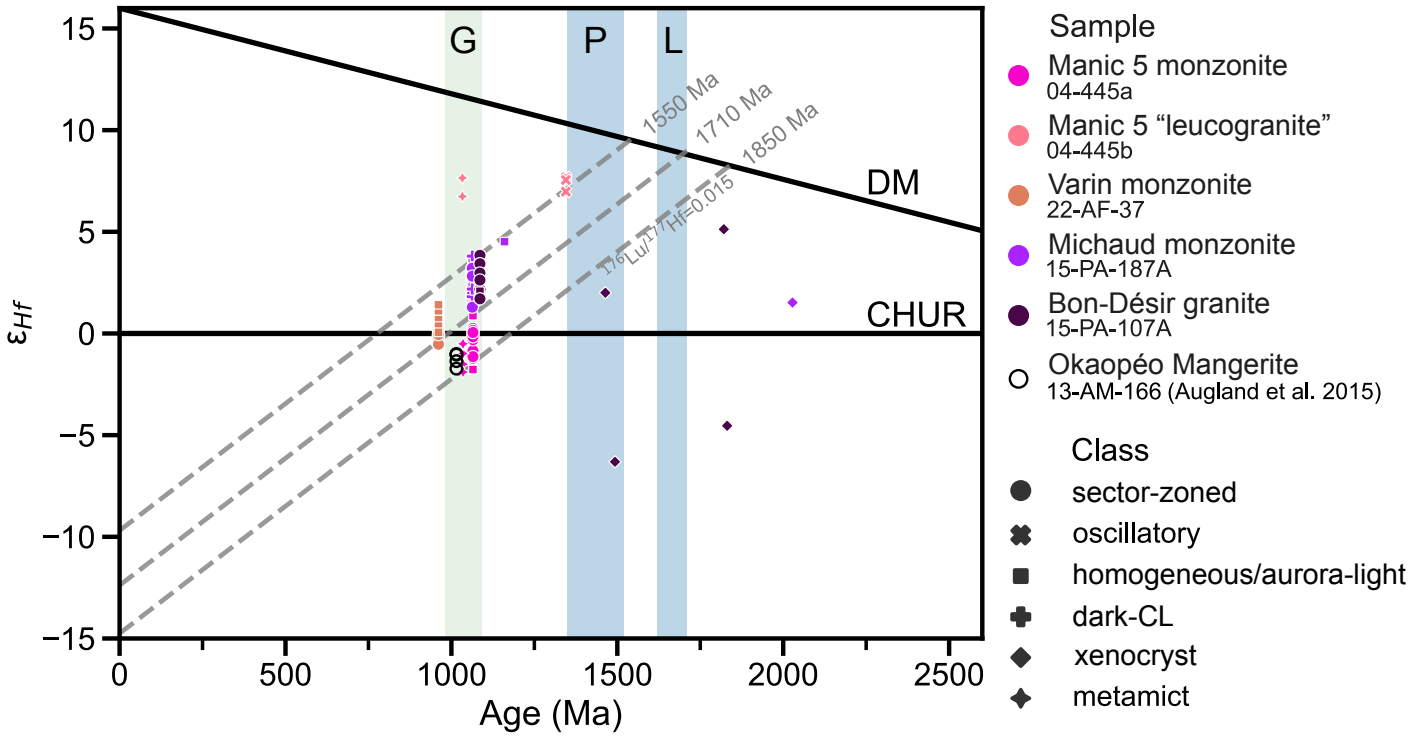

Figure 4.19 Zircon $\varepsilon_{Hf}(t)$ versus crystallisation age diagram. Crystallisation ages of zircon are assumed to be the same within each sample, except inherited zircons. In-situ zircon Lu–Hf with bulk crust evolution lines (grey), assuming $^{176}Lu/^{177}Hf = 0.015$ (Griffin et al. 2002), projecting minimum extraction ages from the depleted mantle. Orogenic periods, G: Grenvillian; P: Pinwarian; L: Labradorian. Depleted mantle (DM) evolution from Vervoort et al. (2018).

Chapter 5. Key points and Conclusions

Orogenic high-*T* granitoid magmatism is an important characteristic of the hinterland of the Grenville Province, but its overall significance in the context of the Grenville Orogen has remained elusive. Grenvillian-age granitoid plutons are unevenly distributed at the scale of the province and are particularly abundant in its central and southwestern parts, where they are variably associated in space with older, ~1.16–1.13 Ga anorthosite intrusions (Fig 1.2 & 1.3). This thesis explored the age, geochemical and isotopic patterns of orogenic high-*T* granitoids exposed in the central Grenville Province to provide a basis for a better understanding of high-*T* granitoid magmatism in a Mesoproterozoic orogenic setting.

The thesis is in two parts. The first part (Chapter 3) provided a synthesis of age and geochemistry data from the literature on granitoids from central Grenville, specifically on those that are intrusive into:

- the ~1.50–1.35 Ga terrane of Quebecia, and are now exposed on the mid- and low-*P* segments of the Grenville orogen (Manicouagan – Baie Comeau/Escoumins areas); and
- the westerly adjacent~1.16 Ga Lac-St-Jean anorthosite suite (Fig. 3.1).

This synthesis set the framework for a more detailed assessment using samples from five granitoids exposed in the mid and low-*P* segments, elaborated in the second part of the thesis (Chapter 4).

The age data summarized in Chapter 3 indicate that the granitoids were emplaced intermittently between ca. 1086 and 1007 Ma throughout the duration of the Grenvillian orogeny. A 10-Myr gap (~1042–1032 Ma) is identified from the available geochronological record, but no major geochemical differences are observed before and after the apparent hiatus. Both older and younger granitoids are exposed in the Lac-St-Jean region, but elsewhere, the older granitoids are mainly observed in the low-*P* segments, with some of them forming large, hecto-kilometric-scale plutons associated with earlier, ~1.16–1.13 Ga anorthosite intrusions, while the younger plutons are smaller, and mainly occur in the mid-*P* segment.

Based on the geochemical data synthetised in Chapter 3, the granitoids have zircon saturation temperatures (T_{Zr}) mostly in the range of ~800–950ºC, consistent with their

classification as high-*T* granitoids. On major-element descriptive classification diagrams, they are ferroan, metaluminous, alkali to alkalic calcic, consistent with derivation from the fractionation of tholeiitic magma. However, trace elements follow a range of signatures from within-plate to volcanic arc, the latter of which is consistent with an influence of arc crust. The granitoids intruded the arc crust of Quebecia that was formed at the eastern Laurentian margin in the Mesoproterozoic and may have partly originated from the partial melting of such crust, acquiring arc-like signatures into their geochemistry.

In addition, the focused study of samples from five granitoids exposed in the mid- to low-*P* segments (Chapter 4) revealed a consistently high-*T* range (~800–1000ºC), *P* at 5–6 kbars and variable redox states, based on amphibole-based thermobarometry, ternary feldspar thermometry, Ti-in zircon thermometry and zircon Ce–U–Ti oxybarometry, collectively in agreement with T_{Zr} outlined in Chapter 3. Also, because inherited zircons are absent or rare, this supports the high-*T* character of the granitoids. Inherited zircons are only present in the plutons from the southernmost low-*P* segment (ESB), where they record Pinwarian and Paleoproterozoic ages, providing further evidence of influence from an older crust. Nd and Hf isotopes consistently point towards older T_{DM}, suggesting that the magma could be derived from the partial melting of Quebecia crust, which in turn, has, in some instances, consisted of older Paleoproterozoic crustal components. Recycling of remnants of Quebecia arc crust, rather than fertile sedimentary sources, is evident by the largely overlapping geochemical signatures of these granitoids and the Nd T_{DM} of Quebecia crust.

Irrespective of the sources, high heat flux from the mantle is required for the formation of the high-*T* granitoid magma. It has been suggested that a hotter mantle, relative to modern times, could account for different orogenic styles and hotter magmatism in the Mesoproterozoic (Spencer et al. 2021), and this could be one possible explanation. However, in the regional context, high-*T* granitoid magmatism in central Grenville occurs in a very specific tectonic setting. It is spatially associated with:

- Quebecia, which formed in a sequence of events involving local rifting of the Laurentian margin, development of peri-cratonic island arcs and accretion of these arcs back to Laurentia, all of these within the interval of ~1.50–1.35 Ga; and

- 1.16–1.13 Ga anorthosites that mark major crustal boundaries (Fig. 3.1).

These associations suggest that there may be a connection between the ~1.16–1.13 Ga to Grenvillian-age high-*T* magmatism and lithospheric architecture and structures inherited from the evolution of Quebecia in the pre-Grenvillian, Mesoproterozoic Laurentian margin.

Orogenic high-*T* magmatism may be linked to these long-lived lithospheric structures that facilitated magma migration and heat transfer. In central Grenville, such structures may have been at the origin of major deformation zones, for instance, Saint-Fulgence and Pipmuacan, which are characterised by polyphase deformation, and were active from at least before 1090 Ma to ~1008 Ma (Owens et al. 1994; Higgins et al. 2002; Hébert et al. 2009). These deformation zones broadly mark the northern boundary of both the rifted and re-accreted portion of the Laurentian margin in Quebecia and the Grenvillian-age voluminous high-*T* granitoids associated with the 1.16 to 1.13 Ga large anorthosites. Therefore, they may represent a prime example of the control of old, inherited lithospheric features on orogenic architecture.

References

Albarède, F., Scherer, E. E., Blichert-Toft, J., Rosing, M., Simionovici, A., & Bizzarro, M. (2006). γ-ray irradiation in the early Solar System and the conundrum of the 176Lu decay constant. *Geochimica et Cosmochimica Acta*, *70*(5), 1261-1270. https://doi.org/10.1016/j.gca.2005.09.027

Anderson, J. L. (1996). Status of thermobarometry in granitic batholiths. *Earth and Environmental Science Transactions of the Royal Society of Edinburgh*, *87*(1-2), 125-138. https://doi.org/10.1017/s0263593300006544

Anderson, J. L., Barth, A. P., Wooden, J. L., & Mazdab, F. (2008). Thermometers and Thermobarometers in Granitic Systems. *Reviews in Mineralogy and Geochemistry*, *69*(1), 121-142. https://doi.org/10.2138/rmg.2008.69.4

Anderson, J. L., & Morrison, J. (2005). Ilmenite, magnetite, and peraluminous Mesoproterozoic anorogenic granites of Laurentia and Baltica. *Lithos*, *80*(1-4), 45-60. https://doi.org/10.1016/j.lithos.2004.05.008

Anderson, J. L., & Smith, D. R. (1995). The effects of temperature and fO2 on the Al-in-hornblende barometer. *American Mineralogist*, *80*(5-6), 549-559. https://doi.org/10.2138/am-1995-5-614

Augland, L. E., Moukhsil, A., Solgadi, F., Indares, A., & McFarlane, C. (2015). Pinwarian to Grenvillian magmatic evolution in the central Grenville Province: new constraints from ID–TIMS U–Pb ages and coupled Lu–Hf S–MC–ICP–MS data. *Canadian Journal of Earth Sciences*, *52*(9), 701-721. https://doi.org/10.1139/cjes-2014-0232

Barbarin, B. (1990). Granitoids - Main Petrogenetic Classifications in Relation to Origin and Tectonic Setting. *Geological Journal*, *25*(3-4), 227-238. https://doi.org/DOI 10.1002/gj.3350250306

Bea, F. (1996). Residence of REE, Y, Th and U in Granites and Crustal Protoliths; Implications for the Chemistry of Crustal Melts. *Journal of Petrology*, *37*(3), 521-552. https://doi.org/10.1093/petrology/37.3.521

Beaumont, C., Jamieson, R., & Nguyen, M. (2010). Models of large, hot orogens containing a collage of reworked and accreted terranes. *Canadian Journal of Earth Sciences*, *47*(4), 485-515. https://doi.org/10.1139/E10-002

Bickford, M. E. (1990). The formation of continental crust: Part 1. A review of some principles; Part 2. An application to the Proterozoic evolution of southern North America. In *Centennial Articles* (pp. 369-386). https://doi.org/10.1130/SPE253-p369

Black, L. P., Kamo, S. L., Allen, C. M., Aleinikoff, J. N., Davis, D. W., Korsch, R. J., & Foudoulis, C. (2003). TEMORA 1: a new zircon standard for Phanerozoic U–Pb geochronology. *Chemical Geology*, *200*(1-2), 155-170. https://doi.org/10.1016/s0009-2541(03)00165-7

Blichert-Toft, J., & Albarède, F. (1997). The Lu-Hf isotope geochemistry of chondrites and the evolution of the mantle-crust system. *Earth and Planetary Science Letters*, *148*(1-2), 243-258. https://doi.org/10.1016/s0012-821x(97)00040-x

Blundy, J. D., & Holland, T. J. B. (1990). Calcic amphibole equilibria and a new amphibole-plagioclase geothermometer. *Contributions to Mineralogy and Petrology*, *104*(2), 208-224. https://doi.org/10.1007/bf00306444

Boehnke, P., Watson, E. B., Trail, D., Harrison, T. M., & Schmitt, A. K. (2013). Zircon saturation re-revisited. *Chemical Geology*, *351*, 324-334. https://doi.org/10.1016/j.chemgeo.2013.05.028

Bonin, B. (1990). From orogenic to anorogenic settings: Evolution of granitoid suites after a major orogenesis. *Geological Journal*, *25*(3-4), 261-270. https://doi.org/10.1002/gj.3350250309

Bonin, B. (2007). A-type granites and related rocks: Evolution of a concept, problems and prospects. *Lithos*, *97*(1-2), 1-29. https://doi.org/10.1016/j.lithos.2006.12.007

Bonin, B., Janoušek, V., & Moyen, J.-F. (2020). Chemical variation, modal composition and classification of granitoids. *Geological Society, London, Special Publications*, *491*(1), 9-51. https://doi.org/10.1144/sp491-2019-138

Bouvier, A., Vervoort, J. D., & Patchett, P. J. (2008). The Lu–Hf and Sm–Nd isotopic composition of CHUR: Constraints from unequilibrated chondrites and implications for the bulk composition of terrestrial planets. *Earth and Planetary Science Letters*, *273*(1-2), 48-57. https://doi.org/10.1016/j.epsl.2008.06.010

Carr, M. J., & Gazel, E. (2016). Igpet software for modeling igneous processes: examples of application using the open educational version. *Mineralogy and Petrology*, *111*(2), 283-289. https://doi.org/10.1007/s00710-016-0473-z

Chappell, B. W., & White, A. J. R. (1974). Two Contrasting Granite Types. *Pacific Geology*, *8*, 173-174.

Chappell, B. W., & White, A. J. R. (2001). Two contrasting granite types: 25 years later. *Australian Journal of Earth Sciences*, *48*(4), 489-499. https://doi.org/10.1046/j.1440-0952.2001.00882.x

Chappell, B. W., White, A. J. R., Williams, I. S., & Wyborn, D. (2007). Low- and high-temperature granites. *Earth and Environmental Science Transactions of the Royal Society of Edinburgh*, *95*(1-2), 125-140. https://doi.org/10.1017/s0263593300000973

Chu, N.-C., Taylor, R. N., Chavagnac, V. r., Nesbitt, R. W., Boella, R. M., Milton, J. A., German, C. R., Bayon, G., & Burton, K. (2002). Hf isotope ratio analysis using multi-collector inductively coupled plasma mass spectrometry: an evaluation of isobaric interference corrections. *Journal of Analytical Atomic Spectrometry*, *17*(12), 1567-1574. https://doi.org/10.1039/b206707b

Clemens, J. D., Holloway, J. R., & White, A. J. R. (1986). Origin of an A-type granite; experimental constraints *American Mineralogist*, *71*(3-4), 317–324.

Collins, W. J., Beams, S. D., White, A. J. R., & Chappell, B. W. (1982). Nature and origin of A-type granites with particular reference to southeastern Australia. *Contributions to Mineralogy and Petrology*, *80*(2), 189-200. https://doi.org/10.1007/bf00374895

Condie, K. (2013). Preservation and Recycling of Crust during Accretionary and Collisional Phases of Proterozoic Orogens: A Bumpy Road from Nuna to Rodinia. *Geosciences*, *3*(2), 240-261. https://doi.org/10.3390/geosciences3020240

Corfu, F., Hanchar, J. M., Hoskin, P. W. O., & Kinny, P. (2003). Atlas of Zircon Textures. In *Zircon* (pp. 469-502). https://doi.org/10.1515/9781501509322-019

Corrigan, D., & Hanmer, S. (1997). Anorthosites and related granitoids in the Grenville orogen: A product of convective thinning of the lithosphere? *Geology*, *25*(1). https://doi.org/10.1130/0091-7613(1997)025<0061:Aargit>2.3.Co;2

Corrigan, D., & van Breemen, O. (1997). U – Pb age constraints for the lithotectonic evolution of the Grenville Province along the Mauricie transect, Quebec. *Canadian Journal of Earth Sciences*, *34*(3), 299-316. https://doi.org/10.1139/e17-027

Corriveau, L., Heaman, L. M., Marcantonio, F., & van Breemen, O. (1990). 1.1 Ga K-rich alkaline plutonism in the SW Grenville Province. *Contributions to Mineralogy and Petrology*, *105*(4), 473-485. https://doi.org/10.1007/bf00286834

Cutts, J. (2014). *Age and Geochemical Character of Granite and Syenite Plutons in the Grenville Province of Southeastern Ontario; Insights into Magmatism During the Ottawan Orogeny and Evidence of the Frontenac Intrusive Suite in the Sharbot Lake Domain* [MSc Thesis, Carleton University]. Ottawa, Ontario.

Dall'Agnol, R., Frost, C. D., & Rämö, O. T. (2012). IGCP Project 510 "A-type Granites and Related Rocks through Time": Project vita, results, and contribution to granite research. *Lithos*, *151*, 1-16. https://doi.org/10.1016/j.lithos.2012.08.003

Daniel, C. G., Indares, A., Medaris Jr, L. G., Aronoff, R., Malone, D., & Schwartz, J. (2023). Linking the Pinware, Baraboo, and Picuris orogens: Recognition of a trans-Laurentian ca. 1520–1340 Ma orogenic belt. In *Laurentia: Turning Points in the Evolution of a Continent* (pp. 175-190). https://doi.org/10.1130/2022.1220(11)

David, J., Moukhsil, A., Clark, T., Hébert, C., Nantel, S., Dion, C., & Sappin, A.-A. l. (2009). *Datations U-Pb effectuées dans les provinces de Grenville et de Churchill en 2006-2007* (RP 2009-03).

David, J., Moukhsil, A., & Dion, C. (2010a). *Datations U-Pb effectuées dans la Province de Grenville en 2008-2009* (RP 2010-10).

David, J., Moukhsil, A., Gobeil, A., Sappin, A.-A., & Dion, C. (2010b). *Datations U-Pb effectuées dans la Province de Grenville en 2007-2008* (RG 2010-02).

Davis, D. W., Moukhsil, A., Isabelle Lafrance, Hammouche, H., Goutier, J., Pilote, P., & Takam, F. T. (2014). *Datations U-Pb dans les provinces du Supérieur, de Churchill et de Grenville effectuées au JSGL en 2012-2013* (RP 2014-07).

Davis, D. W., Williams, I. S., & Krogh, T. E. (2003). Historical Development of Zircon Geochronology. *Reviews in Mineralogy and Geochemistry*, *53*(1), 145-181. https://doi.org/10.2113/0530145

DePaolo, D. (1988). *Neodymium isotope geochemistry: an introduction*. Springer-Verlag. https://doi.org/10.1007/978.3.642.48916-7

DePaolo, D. J. (1981). Neodymium isotopes in the Colorado Front Range and crust–mantle evolution in the Proterozoic. *Nature*, *291*(5812), 193-196. https://doi.org/doi.org/10.1038/291193a0

DePaolo, D. J., Linn, A. M., & Schubert, G. (1991). The continental crustal age distribution: Methods of determining mantle separation ages from Sm-Nd isotopic data and application to the southwestern United States. *Journal of Geophysical Research*, *96*(B2). https://doi.org/10.1029/90jb02219

DePaolo, D. J., & Wasserburg, G. J. (1976a). Inferences about magma sources and mantle structure from variations of143Nd/144Nd. *Geophysical Research Letters*, *3*(12), 743-746. https://doi.org/10.1029/GL003i012p00743

DePaolo, D. J., & Wasserburg, G. J. (1976b). Nd isotopic variations and petrogenetic models. *Geophysical Research Letters*, *3*(5), 249-252. https://doi.org/10.1029/GL003i005p00249

Dickin, A., Hynes, E., Landry, E., & Vautour, S. (2023). The significance of Nd isotope mapping in Precambrian orogenic belts: A case study from the Saguenay region of the Quebec Grenville Province. *Precambrian Research*, *394*, 107-126. https://doi.org/10.1016/j.precamres.2023.107126

Dickin, A. P. (2000). Crustal formation in the Grenville Province: Nd-isotope evidence. *Canadian Journal of Earth Sciences*, *37*(2-3), 165-181. https://doi.org/10.1139/e99-039

Dickin, A. P., & Higgins, M. D. (1992). Sm/Nd evidence for a major 1.5 Ga crust-forming event in the central Grenville province. *Geology*, *20*(2). https://doi.org/10.1130/0091-7613(1992)020<0137:Snefam>2.3.Co;2

Dickin, A. P., McNutt, R. H., Martin, C., & Guo, A. (2009). The extent of juvenile crust in the Grenville Province: Nd isotope evidence. *Geological Society of America Bulletin*, *122*(5-6), 870-883. https://doi.org/10.1130/b26381.1

Dunning, G., & Indares, A. (2010). New insights on the 1.7–1.0Ga crustal evolution of the central Grenville Province from the Manicouagan – Baie Comeau transect. *Precambrian Research*, *180*(3-4), 204-226. https://doi.org/10.1016/j.precamres.2010.04.005

Elkins, L. T., & Grove, T. L. (1990). Ternary feldspar experiments and thermodynamic models. *American Mineralogist*, *75*(5-6), 544-559.

Emslie, R. F., & Hunt, P. A. (1990). Ages and Petrogenetic Significance of Igneous Mangerite-Charnockite Suites Associated with Massif Anorthosites, Grenville Province. *The Journal of Geology*, *98*(2), 213-231. https://doi.org/10.1086/629394

Evans, O. C., & Hanson, G. N. (1993). Accessory-mineral fractionation of rare-earth element (REE) abundances in granitoid rocks. *Chemical Geology*, *110*(1-3), 69-93. https://doi.org/10.1016/0009-2541(93)90248-h

Ferriss, E. D. A., Essene, E. J., & Becker, U. (2008). Computational study of the effect of pressure on the Ti-in-zircon geothermometer. *European Journal of Mineralogy*, *20*(5), 745-755. https://doi.org/10.1127/0935-1221/2008/0020-1860

Ferry, J. M., & Watson, E. B. (2007). New thermodynamic models and revised calibrations for the Ti-in-zircon and Zr-in-rutile thermometers. *Contributions to Mineralogy and Petrology*, *154*(4), 429-437. https://doi.org/10.1007/s00410-007-0201-0

Fisher, C. M., Vervoort, J. D., & Hanchar, J. M. (2014). Guidelines for reporting zircon Hf isotopic data by LA-MC-ICPMS and potential pitfalls in the interpretation of these data. *Chemical Geology*, *363*, 125-133. https://doi.org/10.1016/j.chemgeo.2013.10.019

Fonseca-Martinez, A. B., & Indares, A. (2024). Low-P to Mid-P granulites in the Central Grenville Province: a new finding. Granulites & Granulites, Verbania, Italy.

Frith, R. A., & Doig, R. (1973). Rb–Sr Isotopic Ages and Petrologic Studies of the Rocks in the Lac St. Jean Area, Quebec. *Canadian Journal of Earth Sciences*, *10*(6), 881-899. https://doi.org/10.1139/e73-079

Frost, B. R. (1991). Introduction to Oxygen Fugacity and Its Petrologic Importance. In *Oxide Minerals : Petrologic and Magnetic Significance* (Vol. 25, pp. 1-9). <Go to ISI>://WOS:A1991BT93X00001

Frost, B. R., Barnes, C. G., Collins, W. J., Arculus, R. J., Ellis, D. J., & Frost, C. D. (2001a). A Geochemical Classification for Granitic Rocks. *Journal of Petrology*, *42*(11), 2033-2048. https://doi.org/10.1093/petrology/42.11.2033

Frost, B. R., & Frost, C. D. (2008). On charnockites. *Gondwana Research*, *13*(1), 30-44. https://doi.org/10.1016/j.gr.2007.07.006

Frost, C. D., Bell, J. M., Frost, B. R., & Chamberlain, K. R. (2001b). Crustal growth by magmatic underplating: Isotopic evidence from the northern Sherman batholith. *Geology*, *29*(6). https://doi.org/10.1130/0091-7613(2001)029<0515:Cgbmui>2.0.Co;2

Frost, C. D., & Frost, B. R. (2011). On Ferroan (A-type) Granitoids: their Compositional Variability and Modes of Origin. *Journal of Petrology*, *52*(1), 39-53. https://doi.org/10.1093/petrology/egq070

Ghiorso, M. S., & Evans, B. W. (2008). Thermodynamics of Rhombohedral Oxide Solid Solutions and a Revision of the FE-TI Two-Oxide Geothermometer and Oxygen-Barometer. *American Journal of Science*, *308*(9), 957-1039. https://doi.org/10.2475/09.2008.01

Gobeil, A., Hébert, C., Clark, T., Beaumier, M., & Perreault, S. (2002). *Géologie de la région du lac De La Blache (22K/03 et 22K/04)* (RG 2002-01).

Gobeil, A., Simard, M., Clark, T., Hébert, C., & Leclair, A. (2006). *Géologie de la région du lac Varin (22F/10)* (RP 2006-01). M. d. R. n. Gouvernement du Québec.

Goldstein, S. L., O'Nions, R. K., & Hamilton, P. J. (1984). A Sm-Nd isotopic study of atmospheric dusts and particulates from major river systems. *Earth and Planetary Science Letters*, *70*(2), 221-236. https://doi.org/10.1016/0012-821x(84)90007-4

Gower, C. F., Heaman, L. M., Loveridge, W. D., Schärer, U., & Tucker, R. D. (1991). Grenvillian magmatism in the eastern Grenville Province, Canada. *Precambrian Research*, *51*(1-4), 315-336. https://doi.org/10.1016/0301-9268(91)90106-k

Gower, C. F., & Krogh, T. E. (2002). A U–Pb geochronological review of the Proterozoic history of the eastern Grenville Province. *Canadian Journal of Earth Sciences*, *39*(5), 795-829. https://doi.org/10.1139/e01-090

Griffin, W. L., Wang, X., Jackson, S. E., Pearson, N. J., O'Reilly, S. Y., Xu, X., & Zhou, X. (2002). Zircon chemistry and magma mixing, SE China: In-situ analysis of Hf isotopes, Tonglu and Pingtan igneous complexes. *Lithos*, *61*(3-4), 237-269. https://doi.org/10.1016/s0024-4937(02)00082-8

Grimes, C. B., Wooden, J. L., Cheadle, M. J., & John, B. E. (2015). "Fingerprinting" tectono-magmatic provenance using trace elements in igneous zircon. *Contributions to Mineralogy and Petrology*, *170*(5-6). https://doi.org/10.1007/s00410-015-1199-3

Groulier, P.-A., Indares, A., Dunning, G., & Moukhsil, A. (2016). *Géologie de la ceinture volcano-sédimentaire des Escoumins, Côte-Nord (MB 2016-07)* (MB 2016-07).

Groulier, P.-A., Indares, A., Dunning, G., Moukhsil, A., & Jenner, G. (2018a). Syn-orogenic magmatism over 100 m.y. in high crustal levels of the central Grenville Province: Characteristics, age and tectonic significance. *Lithos*, *312*, 128-152. https://doi.org/10.1016/j.lithos.2018.04.025

Groulier, P.-A., Indares, A., Dunning, G., Moukhsil, A., & Wälle, M. (2018b). Peri-Laurentian, Pinwarian-age oceanic arc crust preserved in the Grenville Province: Insights from the Escoumins supracrustal belt. *Precambrian Research*, *311*, 37-64. https://doi.org/10.1016/j.precamres.2018.04.001

Hanchar, J. M., Finch, R. J., Hoskin, P. W. O., Watson, E. B., Cherniak, D. J., & Mariano, A. N. (2001). Rare earth elements in synthetic zircon: Part 1. Synthesis, and rare earth element and phosphorus doping. *American Mineralogist*, *86*(5-6), 667-680. https://doi.org/10.2138/am-2001-5-607

Hanchar, J. M., & Watson, E. B. (2003). Zircon Saturation Thermometry. *Reviews in Mineralogy and Geochemistry*, *53*(1), 89-112. https://doi.org/10.2113/0530089
Hawthorne, F. C., Oberti, R., Harlow, G. E., Maresch, W. V., Martin, R. F., Schumacher, J. C., & Welch, M. D. (2012). Nomenclature of the amphibole supergroup. *American Mineralogist*, *97*(11-12), 2031-2048. https://doi.org/10.2138/am.2012.4276
Hayden, L. A., & Watson, E. B. (2007). Rutile saturation in hydrous siliceous melts and its bearing on Ti-thermometry of quartz and zircon. *Earth and Planetary Science Letters*, *258*(3-4), 561-568. https://doi.org/10.1016/j.epsl.2007.04.020
Hébert, C., Cadieux, A.-M., & van Breemen, O. (2005). Temporal evolution and nature of Ti–Fe–P mineralization in the anorthosite–mangerite–charnockite–granite (AMCG) suites of the south-central Grenville Province, Saguenay – Lac St. Jean area, Quebec, Canada. *Canadian Journal of Earth Sciences*, *42*(10), 1865-1880. https://doi.org/10.1139/e05-050
Hébert, C., & Lacoste, P. (1998a). *Géologie de la Région de Bagotville (SNRC22D/07)* (RG 97-06).
Hébert, C., & Lacoste, P. (1998b). *Géologie de la région de Jonquière - Chicoutimi (SNRC22D/06)* (RG 96-08).
Hébert, C., van Breemen, O., & Cadieux, A.-M. (2009). *Région du réservoir Pipmuacan, (SNRC 22E) : SYNTHÈSE GÉOLOGIQUE* (978-2-550-56556-7).
Hébert, C., van Breemen, O., & Lacoste, P. (1998). Tectonic setting and U-Pb zircon age of the Poulin-de-Courval Mangerite, Saguenay-Lac Saint-Jean area, Grenville Province, Quebec. In G. S. o. Canada (Ed.), *Radiogenic age and isotopic studies: Report 11* (pp. 69-76). Geological Survey of Canada. https://doi.org/10.4095/210057
Hervet, M., van Breemen, O., & Higgins, M. D. (1994). *U-Pb igneous crystallization ages of intrusive rocks near the southeastern margin of the Lac-St-Jean Anorthosite Complex, Grenville Province, Quebec* (Current Research no. 1994-F). (Radiogenic age and isotopic studies: report 8;, Issue. N. R. Canada.
Higgins, M. D., Ider, M., & van Breemen, O. (2002). U-Pb ages of plutonism, wollastonite formation, and deformation in the central part of the Lac-Saint-Jean anorthosite suite. *Canadian Journal of Earth Sciences*, *39*(7), 1093-1105. https://doi.org/10.1139/e02-033
Higgins, M. D., & van Breemen, O. (1992). The age of the Lac-Saint-Jean Anorthosite Complex and associated mafic rocks, Grenville Province, Canada. *Canadian Journal of Earth Sciences*, *29*(7), 1412-1423. https://doi.org/10.1139/e92-113
Higgins, M. D., & van Breemen, O. (1996). Three generations of anorthosite-mangerite-charnockite-granite (AMCG) magmatism, contact metamorphism and tectonism in the Saguenay-Lac-Saint-Jean region of the Grenville Province, Canada. *Precambrian Research*, *79*(3-4), 327-346. https://doi.org/10.1016/0301-9268(95)00102-6
Hildreth, W., & Moorbath, S. (1988). Crustal contributions to arc magmatism in the Andes of Central Chile. *Contributions to Mineralogy and Petrology*, *98*(4), 455-489. https://doi.org/10.1007/bf00372365
Hokada, T. (2001). Feldspar thermometry in ultrahigh-temperature metamorphic rocks: Evidence of crustal metamorphism attaining ~1100 °C in the Archean Napier Complex, East Antarctica. *American Mineralogist*, *86*(7-8), 932-938. https://doi.org/10.2138/am-2001-0718

Holland, T., & Blundy, J. (1994). Non-ideal interactions in calcic amphiboles and their bearing on amphibole-plagioclase thermometry. *Contributions to Mineralogy and Petrology*, *116*(4), 433-447. https://doi.org/10.1007/bf00310910

Hopkinson, T. N., Harris, N. B. W., Warren, C. J., Spencer, C. J., Roberts, N. M. W., Horstwood, M. S. A., Parrish, R. R., & Vance, D. (2017). The identification and significance of pure sediment-derived granites. *Earth and Planetary Science Letters*, *467*, 57-63. https://doi.org/10.1016/j.epsl.2017.03.018

Hoskin, P. W. O. (2003). The Composition of Zircon and Igneous and Metamorphic Petrogenesis. *Reviews in Mineralogy and Geochemistry*, *53*(1), 27-62. https://doi.org/10.2113/0530027

Hynes, A., & Rivers, T. (2010). Protracted continental collision — evidence from the Grenville Orogen. *Canadian Journal of Earth Sciences*, *47*(5), 591-620. https://doi.org/10.1139/e10-003

Ider, M. (1997). *Géochronologie, géochimie et pétrographie des roches métamorphiques et ignées autour du gisement de wollastonite du Canton Saint-Onge, Québec, Canada* [MSc Thesis, Université du Québec à Chicoutimi].

Indares, A. (2020). Deciphering the metamorphic architecture and magmatic patterns of large hot orogens: Insights from the central Grenville Province. *Gondwana Research*, *80*, 385-409. https://doi.org/10.1016/j.gr.2019.10.013

Indares, A. (2024). The Grenville Province: revisiting the orogenic framework and integrating recent findings. *Canadian Journal of Earth Sciences*. https://doi.org/10.1139/cjes-2023-0143

Indares, A., & Dunning, G. (2018). Metamorphic evolution of the central Grenville Province (Manicouagan area): a review. In A. Moukhsil (Ed.), *Géologie, potentiel minéral et cadre géodynamique des roches de la région du réservoir Daniel-Johnson (Manicouagan), partie centrale de la Province de Grenville* (pp. 171-190).

Indares, A., Moukhsil, A., & Groulier, P.-A. (2023). Geon 14 to early Geon 13 granitoid magmatism in the Grenville Province of Canada, northeastern Laurentia: Distribution, geochemical patterns, and links with an active-margin setting. In *Laurentia: Turning Points in the Evolution of a Continent* (pp. 291-305). https://doi.org/10.1130/2022.1220(17)

Irvine, T. N., & Baragar, W. R. A. (1971). A Guide to the Chemical Classification of the Common Volcanic Rocks.

Ishihara, S. (1977). The Magnetite-series and Ilmenite-series Granitic Rocks. *Mining Geology*, *27*, 293-305. https://doi.org/https://doi.org/10.11456/shigenchishitsu1951.27.293

Jacob, J.-B., Moyen, J.-F., Fiannacca, P., Laurent, O., Bachmann, O., Janoušek, V., Farina, F., & Villaros, A. (2021). Crustal melting vs. fractionation of basaltic magmas: Part 2, Attempting to quantify mantle and crustal contributions in granitoids. *Lithos*, *402-403*. https://doi.org/10.1016/j.lithos.2021.106292

Jacobsen, S. B., & Wasserburg, G. J. (1980). Sm-Nd isotopic evolution of chondrites. *Earth and Planetary Science Letters*, *50*(1), 139-155. https://doi.org/10.1016/0012-821x(80)90125-9

Jamieson, R. A., & Beaumont, C. (2011). Coeval thrusting and extension during lower crustal ductile flow - implications for exhumation of high-grade metamorphic rocks. *Journal of Metamorphic Geology*, *29*(1), 33-51. https://doi.org/10.1111/j.1525-1314.2010.00908.x

Jochum, K. P., Willbold, M., Raczek, I., Stoll, B., & Herwig, K. (2005). Chemical Characterisation of the USGS Reference Glasses GSA-1G, GSC-1G, GSD-1G, GSE-1G,

BCR-2G, BHVO-2G and BIR-1G Using EPMA, ID-TIMS, ID-ICP-MS and LA-ICP-MS. *Geostandards and Geoanalytical Research*, *29*(3), 285-302. https://doi.org/10.1111/j.1751-908X.2005.tb00901.x

Kemp, A. I. S., & Hawkesworth, C. J. (2003). Granitic Perspectives on the Generation and Secular Evolution of the Continental Crust. In *Treatise on Geochemistry* (pp. 349-410). https://doi.org/10.1016/b0-08-043751-6/03027-9

Keppler, H. (2017). Fluids and trace element transport in subduction zones. *American Mineralogist*, *102*(1), 5-20. https://doi.org/10.2138/am-2017-5716

Ketchum, J. W. F., Jackson, S. E., Culshaw, N. G., & Barr, S. M. (2001). Depositional and tectonic setting of the Paleoproterozoic Lower Aillik Group, Makkovik Province, Canada: evolution of a passive margin-foredeep sequence based on petrochemistry and U–Pb (TIMS and LAM-ICP-MS) geochronology. *Precambrian Research*, *105*(2-4), 331-356. https://doi.org/10.1016/s0301-9268(00)00118-2

King, P. L., Chappell, B. W., Allen, C. M., & White, A. J. R. (2001). Are A-type granites the high-temperature felsic granites? Evidence from fractionated granites of the Wangrah Suite. *Australian Journal of Earth Sciences*, *48*(4), 501-514. https://doi.org/10.1046/j.1440-0952.2001.00881.x

Kinny, P. D., & Maas, R. (2003). Lu-Hf and Sm-Nd isotope systems in zircon. In *Zircon* (pp. 327-342). https://doi.org/10.1515/9781501509322-015

Li, Z. X., Bogdanova, S. V., Collins, A. S., Davidson, A., De Waele, B., Ernst, R. E., Fitzsimons, I. C. W., Fuck, R. A., Gladkochub, D. P., Jacobs, J., Karlstrom, K. E., Lu, S., Natapov, L. M., Pease, V., Pisarevsky, S. A., Thrane, K., & Vernikovsky, V. (2008). Assembly, configuration, and break-up history of Rodinia: A synthesis. *Precambrian Research*, *160*(1-2), 179-210. https://doi.org/10.1016/j.precamres.2007.04.021

Lindsley, D. H., & Frost, B. R. (1992). Equilibria among Fe-Ti oxides, pyroxenes, olivine, and quartz: Part I. Theory. *American Mineralogist*, *77*(9-10), 987-1003. https://pubs.geoscienceworld.org/msa/ammin/article/77/9-10/987/42712/Equilibria-among-Fe-Ti-oxides-pyroxenes-olivine

Loiselle, M. C., & Wones, D. R. (1979). Characteristics and origin of anorogenic granites. *Geological Society of America, Abstracts with Programs*, *11*, 468.

Lotout, C., Indares, A., Vervoort, J., & Deloule, E. (2023). High-P metamorphism in the Mesoproterozoic: Petrochronological insights from the Grenville Province. *Precambrian Research*, *399*. https://doi.org/10.1016/j.precamres.2023.107208

Loucks, R. R., Fiorentini, M. L., & Henríquez, G. J. (2020). New Magmatic Oxybarometer Using Trace Elements in Zircon. *Journal of Petrology*, *61*(3). https://doi.org/10.1093/petrology/egaa034

Ludwig, K. R. (1998). On the Treatment of Concordant Uranium-Lead Ages. *Geochimica et Cosmochimica Acta*, *62*(4), 665-676. https://doi.org/10.1016/s0016-7037(98)00059-3

Mattinson, J. M. (2005). Zircon U–Pb chemical abrasion ("CA-TIMS") method: Combined annealing and multi-step partial dissolution analysis for improved precision and accuracy of zircon ages. *Chemical Geology*, *220*(1-2), 47-66. https://doi.org/10.1016/j.chemgeo.2005.03.011

McDonough, W. F., & Sun, S. s. (1995). The composition of the Earth. *Chemical Geology*, *120*(3-4), 223-253. https://doi.org/10.1016/0009-2541(94)00140-4

McLelland, J. M., Selleck, B. W., & Bickford, M. E. (2010a). Review of the Proterozoic evolution of the Grenville Province, its Adirondack outlier, and the Mesoproterozoic inliers of the Appalachians. In *From Rodinia to Pangea: The Lithotectonic Record of the Appalachian Region*. https://doi.org/10.1130/2010.1206(02)

McLelland, J. M., Selleck, B. W., Hamilton, M. A., & Bickford, M. E. (2010b). Late- to Post-Tectonic Setting of Some Major Proterozoic Anorthosite – Mangerite – Charnockite – Granite (AMCG) Suites. *Canadian Mineralogist*, *48*(4), 729-750. https://doi.org/10.3749/canmin.48.4.729

Middlemost, E. A. K. (1994). Naming materials in the magma/igneous rock system. *Earth-Science Reviews*, *37*(3-4), 215-224. https://doi.org/10.1016/0012-8252(94)90029-9

Miller, C. F., McDowell, S. M., & Mapes, R. W. (2003). Hot and cold granites? Implications of zircon saturation temperatures and preservation of inheritance. *Geology*, *31*(6). https://doi.org/10.1130/0091-7613(2003)031<0529:Hacgio>2.0.Co;2

Miller, J. S., Matzel, J. E. P., Miller, C. F., Burgess, S. D., & Miller, R. B. (2007). Zircon growth and recycling during the assembly of large, composite arc plutons. *Journal of Volcanology and Geothermal Research*, *167*(1-4), 282-299. https://doi.org/10.1016/j.jvolgeores.2007.04.019

Morisset, C.-E., Scoates, J. S., Weis, D., & Friedman, R. M. (2009). U–Pb and 40Ar/39Ar geochronology of the Saint-Urbain and Lac Allard (Havre-Saint-Pierre) anorthosites and their associated Fe–Ti oxide ores, Québec: Evidence for emplacement and slow cooling during the collisional Ottawan orogeny in the Grenville Province. *Precambrian Research*, *174*(1-2), 95-116. https://doi.org/10.1016/j.precamres.2009.06.009

Moukhsil, A., & Côté, G. (2018). *Géologie de la région du lac Borgia, Province de Grenville, nord de La Tuque, régions de la Mauricie et du Saguenay-Lac-St-Jean, Québec, Canada* (BG 2018-01). G. d. Québec. http://gq.mines.gouv.qc.ca/bulletinsgeologiques/lac-borgia/

Moukhsil, A., Lacoste, P., Gobeil, A., & David, J. (2009). *Synthèse géologique de la région de Baie-Comeau (SNRC 22F)* (RG 2009-03). G. d. Québec.

Moukhsil, A., Lacoste, P., Solgadi, F., & David, J. (2011). *Géologie de la partie orientale de la région de Baie-Comeau (partie ouest de 22G)* (RG 2011-02).

Moukhsil, A., Solgadi, F., Belkacim, S. d., Elbasbas, A., & Augland, L. E. (2014). *Géologie de la région du lac Okaopéo, Côte-Nord* (RG 2014-03). G. d. Québec.

Moukhsil, A., Solgadi, F., Clarke, T., Blouin, S., Indares, A., & Davis, D. W. (2013a). *Géologie du nord-ouest de la région du barrage Daniel-Johnson (Manic 5), Côte-Nord* (RG 2013-01). G. d. Québec.

Moukhsil, A., Solgadi, F., Indares, A., & Belkacim, S. d. (2013b). *Géologie de la région septentrionale du réservoir aux Outardes 4, Côte-Nord* (RG 2013-03).

Moyen, J.-F., Janoušek, V., Laurent, O., Bachmann, O., Jacob, J.-B., Farina, F., Fiannacca, P., & Villaros, A. (2021). Crustal melting vs. fractionation of basaltic magmas: Part 1, granites and paradigms. *Lithos*, *402-403*. https://doi.org/10.1016/j.lithos.2021.106291

MRNF. (2021). *Système d'information géominière (SIGÉOM)*. Gouvernement du Québec. Retrieved 11 May 2023 from https://sigeom.mines.gouv.qc.ca/

Nekvasil, H. (1992). Ternary feldspar crystallization in high-temperature felsic magmas. *American Mineralogist*, *77*(5-6), 592-604.

Nekvasil, H. (2011). Feldspar crystallisation in felsic magmas: a review. *Earth and Environmental Science Transactions of the Royal Society of Edinburgh*, *83*(1-2), 399-407. https://doi.org/10.1017/s0263593300008063

Nesbitt, H. W., & Young, G. M. (1982). Early Proterozoic Climates and Plate Motions Inferred from Major Element Chemistry of Lutites. *Nature*, *299*(5885), 715-717. https://doi.org/DOI 10.1038/299715a0

O'Nions, R. K., Hamilton, P. J., & Evensen, N. M. (1977). Variations in143Nd/144Nd and87Sr/86Sr ratios in oceanic basalts. *Earth and Planetary Science Letters*, *34*(1), 13-22. https://doi.org/10.1016/0012-821x(77)90100-5

Owens, B. E., Dymek, R. F., Tucker, R. D., Brannon, J. C., & Podosek, F. A. (1994). Age and radiogenic isotopic composition of a late- to post-tectonic anorthosite in the Grenville Province: the Labrieville massif, Quebec. *Lithos*, *31*(3-4), 189-206. https://doi.org/10.1016/0024-4937(94)90009-4

Patchett, P. J., & Tatsumoto, M. (1981). A routine high-precision method for Lu-Hf isotope geochemistry and chronology. *Contributions to Mineralogy and Petrology*, *75*(3), 263-267. https://doi.org/10.1007/bf01166766

Patiño Douce, A. E., & McCarthy, T. C. (1998). Melting of Crustal Rocks During Continental Collision and Subduction. In *When Continents Collide: Geodynamics and Geochemistry of Ultrahigh-Pressure Rocks* (pp. 27-55). https://doi.org/10.1007/978-94-015-9050-1_2

Paton, C., Woodhead, J. D., Hellstrom, J. C., Hergt, J. M., Greig, A., & Maas, R. (2010). Improved laser ablation U-Pb zircon geochronology through robust downhole fractionation correction. *Geochemistry, Geophysics, Geosystems*, *11*(3). https://doi.org/10.1029/2009gc002618

Pearce, J. A., Harris, N. B. W., & Tindle, A. G. (1984). Trace Element Discrimination Diagrams for the Tectonic Interpretation of Granitic Rocks. *Journal of Petrology*, *25*(4), 956-983. https://doi.org/10.1093/petrology/25.4.956

Pearce, N. J. G., Perkins, W. T., Westgate, J. A., Gorton, M. P., Jackson, S. E., Neal, C. R., & Chenery, S. P. (2007). A Compilation of New and Published Major and Trace Element Data for NIST SRM 610 and NIST SRM 612 Glass Reference Materials. *Geostandards Newsletter*, *21*(1), 115-144. https://doi.org/10.1111/j.1751-908X.1997.tb00538.x

Peccerillo, A., & Taylor, S. R. (1976). Geochemistry of eocene calc-alkaline volcanic rocks from the Kastamonu area, Northern Turkey. *Contributions to Mineralogy and Petrology*, *58*(1), 63-81. https://doi.org/10.1007/bf00384745

Pitcher, W. S. (1997). *The nature and origin of granite*. Springer Science & Business Media.

Ridolfi, F. (2021). Amp-TB2: An Updated Model for Calcic Amphibole Thermobarometry. *Minerals*, *11*(3). https://doi.org/10.3390/min11030324

Ridolfi, F., & Renzulli, A. (2012). Calcic amphiboles in calc-alkaline and alkaline magmas: thermobarometric and chemometric empirical equations valid up to 1,130°C and 2.2 GPa. *Contributions to Mineralogy and Petrology*, *163*(5), 877-895. https://doi.org/10.1007/s00410-011-0704-6

Rieder, M., Cavazzini, G., D'yakonov, Y. S., Frank-Kamenetskii, V. A., Gottardi, G., Guggenheim, S., Pavel W. Koval, G. M., Neiva, A. M. R., Radoslovich, E. W., Robert, J.-L., Sassi, F. P., Takeda, H., Weiss, Z., & Wones, D. R. (1998). Nomenclature of the Micas. *Clays and Clay Minerals*, *46*(5), 586-595. https://doi.org/10.1346/ccmn.1998.0460513

Rivers, T. (1997). Lithotectonic elements of the Grenville Province: review and tectonic implications. *Precambrian Research*, *86*(3-4), 117-154. https://doi.org/Doi 10.1016/S0301-9268(97)00038-7

Rivers, T. (2008). Assembly and preservation of lower, mid, and upper orogenic crust in the Grenville Province-Implications for the evolution of large hot long-duration orogens. *Precambrian Research*, *167*(3-4), 237-259. https://doi.org/10.1016/j.precamres.2008.08.005

Rivers, T. (2012). Upper-crustal orogenic lid and mid-crustal core complexes: signature of a collapsed orogenic plateau in the hinterland of the Grenville Province. *Canadian Journal of Earth Sciences*, *49*(1), 1-42. https://doi.org/10.1139/e11-014

Rivers, T., Culshaw, N., Hynes, A., Indares, A., Jamieson, R., & Martignole, J. (2012). The Grenville Orogen — A Post-LITHOPROBE Perspective. In J. A. Percival, F. A. Cook, & R. M. Clowes (Eds.), *Tectonic Styles in Canada: The LITHOPROBE Perspective* (pp. 97-238). Geological Association of Canada.

Roberts, N. M. W., & Spencer, C. J. (2014). The zircon archive of continent formation through time. *Geological Society, London, Special Publications*, *389*(1), 197-225. https://doi.org/10.1144/sp389.14

Roberts, N. M. W., Yakymchuk, C., Spencer, C. J., Keller, C. B., & Tapster, S. R. (2024). Revisiting the discrimination and distribution of S-type granites from zircon trace element composition. *Earth and Planetary Science Letters*, *633*. https://doi.org/10.1016/j.epsl.2024.118638

Rondot, J. (1986). *Géologie de la région de Forestville-Les Escoumins* (ET 85-05).

Sláma, J., Košler, J., Condon, D. J., Crowley, J. L., Gerdes, A., Hanchar, J. M., Horstwood, M. S. A., Morris, G. A., Nasdala, L., Norberg, N., Schaltegger, U., Schoene, B., Tubrett, M. N., & Whitehouse, M. J. (2008). Plešovice zircon — A new natural reference material for U–Pb and Hf isotopic microanalysis. *Chemical Geology*, *249*(1-2), 1-35. https://doi.org/10.1016/j.chemgeo.2007.11.005

Spencer, C. J., Kirkland, C. L., Roberts, N. M. W., Evans, N. J., & Liebmann, J. (2020). Strategies towards robust interpretations of in situ zircon Lu–Hf isotope analyses. *Geoscience Frontiers*, *11*(3), 843-853. https://doi.org/10.1016/j.gsf.2019.09.004

Spencer, C. J., Mitchell, R. N., & Brown, M. (2021). Enigmatic Mid-Proterozoic Orogens: Hot, Thin, and Low. *Geophysical Research Letters*, *48*(16). https://doi.org/10.1029/2021gl093312

Spencer, C. J., Roberts, N. M. W., & Santosh, M. (2017). Growth, destruction, and preservation of Earth's continental crust. https://doi.org/10.1016/j.earscirev.2017.07.013

Streckeisen, A. (1976). To each plutonic rock its proper name. *Earth-Science Reviews*, *12*(1), 1-33. https://doi.org/10.1016/0012-8252(76)90052-0

Sun, S. s., & McDonough, W. F. (1989). Chemical and isotopic systematics of oceanic basalts: implications for mantle composition and processes. *Geological Society, London, Special Publications*, *42*(1), 313-345. https://doi.org/10.1144/gsl.Sp.1989.042.01.19

Szymanowski, D., Fehr, M. A., Guillong, M., Coble, M. A., Wotzlaw, J.-F., Nasdala, L., Ellis, B. S., Bachmann, O., & Schönbächler, M. (2018). Isotope-dilution anchoring of zircon reference materials for accurate Ti-in-zircon thermometry. *Chemical Geology*, *481*, 146-154. https://doi.org/10.1016/j.chemgeo.2018.02.001

Tanaka, T., Togashi, S., Kamioka, H., Amakawa, H., Kagami, H., Hamamoto, T., Yuhara, M., Orihashi, Y., Yoneda, S., Shimizu, H., Kunimaru, T., Takahashi, K., Yanagi, T., Nakano, T., Fujimaki, H., Shinjo, R., Asahara, Y., Tanimizu, M., & Dragusanu, C. (2000). JNdi-1: a neodymium isotopic reference in consistency with LaJolla neodymium. *Chemical Geology*, *168*(3-4), 279-281. https://doi.org/10.1016/s0009-2541(00)00198-4

Thirlwall, M. F., & Anczkiewicz, R. (2004). Multidynamic isotope ratio analysis using MC–ICP–MS and the causes of secular drift in Hf, Nd and Pb isotope ratios. *International Journal of Mass Spectrometry*, *235*(1), 59-81. https://doi.org/10.1016/j.ijms.2004.04.002

Touret, J. L. R., & Huizenga, J. M. (2012). Charnockite microstructures: From magmatic to metamorphic. *Geoscience Frontiers*, *3*(6), 745-753. https://doi.org/10.1016/j.gsf.2012.05.004

Turcotte, S. (2001). *Mise en place de la portion nord-est de la suite anorthositique du Lac-Saint-Jean durant un chevauchement Grenvillien* [Mémoire de maîtrise, Université du Québec à Chicoutimi]. Chicoutimi. https://constellation.uqac.ca/id/eprint/906/

van Breemen, O. (2009). *Report on U-Pb geochronology for the Pipmuacan Reservoir region* (MB2009-04). M. d. R. n. Gouvernement du Québec.

Vautour, S., & Dickin, A. (2019). Nd isotope mapping of a Pinwarian-age composite arc belt in the Quebecia terrane of the central Grenville Province, Canada. *Precambrian Research*, *332*. https://doi.org/10.1016/j.precamres.2019.105409

Vavra, G. (1990). On the kinematics of zircon growth and its petrogenetic significance: a cathodoluminescence study. *Contributions to Mineralogy and Petrology*, *106*(1), 90-99. https://doi.org/10.1007/bf00306410

Vavra, G. (1994). Systematics of internal zircon morphology in major Variscan granitoid types. *Contributions to Mineralogy and Petrology*, *117*(4), 331-344. https://doi.org/10.1007/bf00307269

Vavra, G., Schmid, R., & Gebauer, D. (1999). Internal morphology, habit and U-Th-Pb microanalysis of amphibolite-to-granulite facies zircons: geochronology of the Ivrea Zone (Southern Alps). *Contributions to Mineralogy and Petrology*, *134*(4), 380-404. https://doi.org/10.1007/s004100050492

Vermeesch, P. (2018). IsoplotR: A free and open toolbox for geochronology. *Geoscience Frontiers*, *9*(5), 1479-1493. https://doi.org/10.1016/j.gsf.2018.04.001

Vernon, R. H. (2016). Rapakivi granite problems: plagioclase mantles and ovoid megacrysts. *Australian Journal of Earth Sciences*, *63*(6), 675-700. https://doi.org/10.1080/08120099.2016.1241953

Vervoort, J. D., Kemp, A. I., & Fisher, C. M. (2018, December 01, 2018). *Hf isotope constraints on evolution of the depleted mantle and growth of continental crust* AGU Fall Meeting Abstracts, https://ui.adsabs.harvard.edu/abs/2018AGUFM.V23A..07V

Watson, E. B., & Harrison, T. M. (1983). Zircon saturation revisited: temperature and composition effects in a variety of crustal magma types. *Earth and Planetary Science Letters*, *64*(2), 295-304. https://doi.org/10.1016/0012-821x(83)90211-x

Whalen, J. B., Currie, K. L., & Chappell, B. W. (1987). A-type granites: geochemical characteristics, discrimination and petrogenesis. *Contributions to Mineralogy and Petrology*, *95*(4), 407-419. https://doi.org/10.1007/bf00402202

Whalen, J. B., & Hildebrand, R. S. (2019). Trace element discrimination of arc, slab failure, and A-type granitic rocks. *Lithos*, *348-349*. https://doi.org/10.1016/j.lithos.2019.105179

Whitmeyer, S. J., & Karlstrom, K. E. (2007). Tectonic model for the Proterozoic growth of North America *Geosphere*, *3*(4). https://doi.org/10.1130/ges00055.1

Wiedenbeck, M., Allé, P., Corfu, F., Griffin, W. L., Meier, M., Oberli, F., Quadt, A. V., Roddick, J. C., & Spiegel, W. (1995). Three Natural Zircon Standards for U-Th-Pb, Lu-Hf, Trace Element and Ree Analyses. *Geostandards Newsletter*, *19*(1), 1-23. https://doi.org/10.1111/j.1751-908X.1995.tb00147.x

Wiedenbeck, M., Hanchar, J. M., Peck, W. H., Sylvester, P., Valley, J., Whitehouse, M., Kronz, A., Morishita, Y., Nasdala, L., Fiebig, J., Franchi, I., Girard, J. P., Greenwood, R. C., Hinton, R., Kita, N., Mason, P. R. D., Norman, M., Ogasawara, M., Piccoli, P. M., . . . Zheng, Y. F. (2007). Further Characterisation of the 91500 Zircon Crystal. *Geostandards and Geoanalytical Research*, *28*(1), 9-39. https://doi.org/10.1111/j.1751-908X.2004.tb01041.x

Williams, M., Schoneveld, L., Mao, Y., Klump, J., Gosses, J., Dalton, H., Bath, A., & Barnes, S. (2020). pyrolite: Python for geochemistry. *Journal of Open Source Software*, *5*(50). https://doi.org/10.21105/joss.02314

Wilson, R. W., Houseman, G. A., Buiter, S. J. H., McCaffrey, K. J. W., & Doré, A. G. (2019). Fifty years of the Wilson Cycle concept in plate tectonics: an overview. *Geological Society, London, Special Publications*, *470*(1), 1-17. https://doi.org/10.1144/sp470-2019-58

Woodhead, J., Hergt, J., Shelley, M., Eggins, S., & Kemp, R. (2004). Zircon Hf-isotope analysis with an excimer laser, depth profiling, ablation of complex geometries, and concomitant age estimation. *Chemical Geology*, *209*(1-2), 121-135. https://doi.org/10.1016/j.chemgeo.2004.04.026